APPLICATIONS OF ADAPTIVE INTEGRAL METHOD IN ELECTROMAGNETIC SCATTERING BY LARGE-SCALE COMPOSITE MEDIA AND FINITE ARRAYS

HU LI
(B.ENG.(HONS.), ZHEJIANG UNIVERSITY, CHINA)

A THESIS SUBMITTED
FOR THE DEGREE OF DOCTOR OF PHILOSOPHY
DEPARTMENT OF ELECTRICAL AND COMPUTER ENGINEERING
NATIONAL UNIVERSITY OF SINGAPORE
2010

Acknowledgement

First of all, I express my gratitude towards my supervisors, Professor Li Le-Wei and Professor Yeo Tat Soon, for their guidance in my research topics. Without their kind supervision and warm support, this thesis would not have been realized.

Second, I am grateful to Mr. Ng Chin Hock of the Radar & Signal Processing Laboratory for his technical support during my research period.

Third, I greatly appreciated the help from Dr. Ewe Wei-Bin, Dr. Qiu Cheng-Wei, Miss Li Ya-Nan and other friends.

Last but not the least, I cannot come out the words to express the greatness of my parents. Without them, I cannot come to the lovely world, not to mention pursuing my PhD study here. I owe a lot to them!

This thesis is devoted to my beloved girlfriend, Yu Dan. Without her companion and encouragement, I cannot bear the bitterness and misfortune along the way to finish the thesis!

Contents

Summary

The aim of the thesis is two-fold: the first part is to discuss the development of Adaptive Integral Method (AIM) solvers for the analysis of the electromagnetic scattering by large objects with composite media; the second part is to discuss the acceleration of conventional AIM in the solution of large finite periodic array scattering problems. These two parts are closely-related since many interesting and important problems considered now are finite periodic structures and the unit cell in an array may be made of composite materials, be it anisotropic or chiral.

The development of AIM for electromagnetic scattering by large objects with composite media was considered and discussed. It is noted that we can use Surface Integral Equation (SIE) method to solve the scattering problem by homogeneous chiral objects which can greatly reduce the unknowns compared to Volume Integral Equation (VIE). Therefore, we developed AIM solver based on SIE to solve electromagnetic scattering by large chiral and conducting objects. Numerical results demonstrate the accuracy of our code as well as the efficiency in solving scattering by large chiral and conducting objects.

The development of the AIM solver for solving the scattering problem by large objects with the most general composite media, bi-anisotropic media, was also explored. Due to the lack of closed form Green's function for the bi-anisotropic media, we developed our solver based on VIE through

which free space Green's function is utilized. Numerical results demonstrate the accuracy of our code as well as the efficiency in solving scattering by large bi-anisotropic and conducting objects.

Conventional AIM solvers has been known to be inadequate when applied to solve large periodic array problems. It is due to the ignorance of the structure's periodicity and hence the problem can become intractable. However, recently developed macro basis functions can greatly reduce the unknowns for a unit cell thus relief the burden of conventional AIM in solving these problems. Therefore, the development of new AIM solvers called accurate-sub-entire-domain AIM (ASED-AIM) are developed based on the incorporation of the macro basis functions into conventional AIM. Complexity analysis demonstrates that it is much more efficient than the conventional AIM. Numerical results show its accuracy in calculating the far field RCS through comparison with the conventional AIM.

Although ASED-AIM is accurate enough to calculate the far field RCS, it is not accurate in calculating the near fields. However, characteristic basis function method (CBFM) is a good candidate in calculating the near fields. Therefore, we developed the CBFM/AIM algorithm. Numerical results compared with AIM demonstrate that it is both accurate in calculating the far fields and near fields.

List of Tables

List of Figures

Chapter 1

Introduction

1.1 Electromagnetic Scattering and Adaptive Integral Method

Electromagnetic (EM) scattering is the disturbance of EM fields by the obstacles or scatterers. It has wide applications in many areas. Many methods have been developed for EM scattering problems. The first one is the analytical method, which is accurate but can only be applied for the solution of canonical structures such as spheres. The second one is the asymptotic method which only gives approximate solutions under certain situations. The most popular method is the numerical method. It is rigorous and has no limitations on the shapes of objects involved. Many categories of numerical methods have been developed so far. One is the differential equation solver such as Finite-Difference Time-Domain (FDTD) method [1] and Finite Element Method (FEM) [2], and another is the integral equation solver such as Method of Moments (MoM).

The MoM has been popular since the publication of Harrington's book [3]. It has several advantages over the differential solvers. The first advan-

tage is that it only needs to discretize the surface for problems with homogeneous media, while the differential solver has to discretize the whole body. The second advantage is that it builds on the Green's function, thus the radiation boundary condition is automatically satisfied, while the differential solver has to impose an artificially set boundary condition.

However, there are also some disadvantages of the MoM. The most severe disadvantage is that when using the MoM to solve problems, it will convert the integral equations into a dense matrix. The memory requirement of storing the dense matrix is $O(N^2)$ while the computational time for solving the dense matrix is $O(N^3)$, if a direct solver such as the Gaussian elimination method is used, or $O(N_{iter}N^2)$, if an iterative solver such as the Generalized Minimal Residual Method (GMRES) is used. Here N denotes the number of unknowns and N_{iter} denotes the number of iterations. Therefore, the memory requirement and computational time will be very demanding if the number of unknowns becomes large which prohibits the direct use of the MoM to solve the large-scale problems prevailing today.

In order to alleviate the difficulties met in the solution of using the MoM, and reduce the memory requirement and accelerate the solution process, many fast solvers have been developed recently. There are many kinds of fast solvers in literature now. One is Fast Multiple Method (FMM) [4,5] and its extension Multilevel Fast Multipole Algorithm (MLFMA) [6–9]. They are developed on the addition theorem of the Green's function, which can express the interaction in one coordinate using another. The basic idea is to divide the basis functions into groups similar to the telephone network. The interaction of basis functions at a far distance is realized through the hub of the group while the interaction of basis functions within the same group are calculated directly. Hub A of one group aggregates the radiation pattern of all the basis functions, translated to another hub B via the ad-

dition theorem and then the hub B disaggregate the radiation pattern to respective basis functions under its control. The computational complexity for MLFMA is $O(N \log N)$ and the memory requirement is $O(N)$.

Another fast solver is based on the translation invariance of the Green's functions, so that the matrix vector multiplication can be written as the convolution in which the Fast Fourier Transform (FFT) can be used. The pioneer one is the Conjugate Gradient FFT (CG-FFT) [10–15]. Its computational complexity is $O(N \log N)$ and memory requirement is $O(N)$. However, it uses the rectangular grids to approximate the arbitrarily shaped objects, which results in the staircase error. To overcome the drawback of the CG-FFT, the Adaptive Integral Method (AIM) [16–20, 19, 21–26] and the precorrect-FFT (p-FFT) methods [27–31] have been proposed. The AIM and the p-FFT methods are similar in that they all have the same solution process. That is, to project the basis functions onto grids, then to calculate the far-zone interaction using FFT, interpolate the potential to individual basis functions, and directly calculate the near zone interaction. They only differ in the projection operators. The AIM is based on the multiple moment expansion while the p-FFT employs the far field matching technique. The AIM has been successfully utilized in solving large scale electromagnetic scattering problems of conducting objects [32], dielectric objects [18], dielectric and conducting objects [17] and magnetodielectric objects [22].

Until now, no one has applied the AIM to the bi-anisotropic media. In the first part of the thesis, the author developed the AIM solvers for the electromagnetic scattering by large-scale chiral and conducting objects based on surface integral equations (SIE), and for EM scattering by bi-anisotropic and conducting objects based on volume surface integral equations (VSIE). Recently, there is an increased research interest in the peri-

odic structure problems. However, direct application of the conventional AIM solver in these periodic structures is inadequate as no consideration has been given to the periodicity of the structure. Macro basis functions can greatly reduce the number of unknowns for a unit cell, thus greatly relieve the computational burden. In the second part of the thesis, the author developed the new AIM solvers based on the macro basis functions to efficiently solve the scattering by large-scale finite array problems.

1.2 Literature Review

In this section, literature review will be given in the area of the MoM solution of electromagnetic scattering by composite media and the development of macro basis functions.

1.2.1 Electromagnetic Scattering by composite media

In recent years, extensive research has been conducted on the interaction between electromagnetic waves and composite media. The most general form of the composite media is bi-anisotropic media, which is characterized by four constitutive tensor parameters. The dielectric, magnetodielectric, chiral, anisotropic, gyroelectric, gyromagnetic and Faraday chiral materials are its subclasses. The composite media have been widely used in the electromagnetic applications. Dielectric materials have been used in optical circuits [33]. The magnetodielectric materials have been used as metamaterials [34]. The chiral materials have been widely used as polarization transformer [35] and antenna radome [36]. Gyromagnetic materials

have been used in ferromagnetic film devices [37]. Other anisotropic and bi-anisotropic materials have been widely used [38–41].

Because of wide applications, numerous methods have been applied to solve the electromagnetic problems involving composite media. Analytical methods such as Mie series have been used to solve electromagnetic scattering by canonical structures such as spheres and spherical shells with chiral materials [42,43]. Spherical vector wave function method is applied to solve scattering by spheres, spherical shells and conducting spheres coated with uniaxial anisotropic [44], gyroelectric [45–47], gyromagnetic [48] materials. Numerical methods are also applied to solve composite media scattering problems. FDTD has been widely applied in solving electromagnetic problem with chiral materials [49–52]. FEM is also utilized for the solution of chiral and bi-anisotropic media problem [53–55].

MoM is also widely used to solve the electromagnetic scattering problems with composite media. There are two ways in using the MoM, one is based on the SIE and the other is based on the VIE. SIE can be applied for piecewise homogeneous objects where the closed form of Green's function can be found while VIE is based on free space Green's function thus it can be applied for inhomogenous media where the closed form of Green's function for the media is very difficult to obtain. Chiral media, since it has four scalar constitutive parameters, thus, denotes the most general bi-isotropic media. Moreover, for chiral objects, because of the field decomposition method [56], the SIE can be formulated for the scattering by homogeneous chiral objects. Kluskens et al. have solved two dimensional chiral scattering problems [57, 58] and Worasawate et al. have used the method to three dimensional case where scattering by a homogeneous body is considered [59]. So far, to the author's knowledge, no one has considered the general situation based on MoM where the scatterers can be of arbitrarily

number, the scatterers can be homogeneous chiral or conducting ones, they can be separate or coated by others. Therefore, in this thesis, the author will develop the AIM solver for the fast and efficient solution of electromagnetic scattering by large-scale chiral and conducting objects based on SIE. For the most general media, bi-anisotropic media, which is characterized by four tensor constitutive parameters, since no closed form Green's function exists, only VIE can be applied to solve the scattering problems. Actually, many authors have developed formulations for solving various kinds of scattering problems. Schaubert et. al. developed Schaubert-Wilton-Glisson (SWG) basis function [60] for the inhomogenous dielectric objects which is widely used today. Lu et. al. developed the VSIE [61] for the solution of dielectric and conducting objects. Su solved problems with gyroelectric objects [62]. Shanker et al. obtained solutions for anisotropic objects with both permittivity and permeability as tensors [63]. Hasanovic et al. solved inhomogeneous chiral objects problems [64]. So far, to the best of author's knowledge, no one has applied the VSIE for the solution of the general bi-anisotropic and conducting objects. In this thesis, the author will develop AIM for the fast and efficient solution of the scattering by large-scale bi-anisotropic and conducting objects based on VSIE.

1.2.2 Macro Basis Functions

Research into the characteristics of periodic array of scatterers, e.g. photonic crystals [33] and meta-materials [34], has been actively pursued in recent years. Due to their important applications, fast and accurate algorithms for solving these problems are urgently needed. It is noted that in the solution of these problems, truncated periodic structures are essential for their accurate characterization. There are many methods in solving these problems such as the array decomposition method based on

FE-BI [65, 66], non-overlapping domain decomposition with non-matching grids [67–71] and FETI-DPEM [72–76] based on FEM. The idea of array decomposition method is based on the repetition of the array elements, thus the Toeplitz matrix property is used to reduce the storage requirement and the FFT is employed to accelerate the matrix vector multiplication. The non-overlapping domain decomposition with non-matching grids is based on cement technique, therefore nonconformal meshes for neighboring subdomain can be used. The FETI-DPEM, which is based on Lagrange multipliers, extends the idea of FETI-DP for the solution of scalar Helmholtz equations.

The MoM can be also used to solve finite array problems. However, the direct use of the MoM results in a dense matrix; thus, the MoM becomes numerically inefficient when solving large array problems, and this has led to development of fast solvers, which aim to alleviate the computational burden. It should be realized, however, that the fast solvers such as FMM and AIM are general-purpose in nature and, hence, are not set up to take advantage of the quasi-periodic nature of the large array problems with a view to reducing the computational burden. Recently, a number of numerical techniques have been proposed for addressing the problems of large-scale finite arrays using the MoM. One is based on the use of an infinite array approach as a starter, followed by corrections that account for the edge effects introduced by the truncation of the infinite array [77–82]. The other type of algorithm for efficient analysis of scattering problems is based on the use of macro-basis functions that are constructed by combining low-level basis functions, which can conform to arbitrarily shaped objects. Employing macro-basis functions greatly reduces the number of unknowns without compromising the solution accuracy, enabling us to solve large problems that are often beyond the scope of conventional methods. Techniques that fall within this class are the characteristic basis function

method (CBFM) [83–88], the synthetic-function approach [89–91], the accurate sub-entire-domain (ASED) basis function method [92–94], the eigencurrent approach [95–97] and the subdomain multilevel approach [98–100]. A common attribute of all of these approaches is that their applications leads to reduce the size of the matrix that is needed to solve to construct the solution; however, they do differ, often considerably, in the way they construct the macro-basis functions. It is worthy to note that ASED basis functions, which were proposed by Cui et al. [92], is specifically designed for treating finite periodic structure problems. The ASED basis functions are obtained by the solution of a nine cell problem which considers the most important coupling from near neighbors. The ASED method was accelerated using CG-FFT [93] and later combined with the FMM to significantly reduce memory requirement and computational complexity of FMM in solving periodic array problems [94]. Although the ASED basis function method is accurate enough to calculate far-field RCS, it seems to be less accurate to calculate the near field. The CBFM, which is proposed by Mittra et al. [83], can be used to treat the near field problems very well. The CBFM obtains its macro basis functions through exciting the unit cell with plane waves of arbitrarily incidence angles and polarizations and get rid of the redundant information through SVD process. It has been extensively used to solve a wide class of scattering and radiation problems. In this thesis, the author first combine the conventional AIM with ASED basis functions to calculate far field RCS of large scale finite array comprising of conducting and dielectric objects. Then, the author proposes a new AIM based on the CBFM to calculate both near-field and far-field parameters of large-scale arrays.

1.3 Outline of Thesis

There are seven chapters for the thesis. The first chapter is this chapter, which serves as an introduction to the thesis. The second chapter introduces the basic idea of AIM.

Chapter 3 discusses the development of the AIM solver for the scattering by large-scale chiral and conducting objects. Chapter 4 discusses the development of the AIM solver for the scattering by large-scale bi-anisotropic and conducting objects. Chapter 5 discusses the development of the ASED-AIM solver for the scattering by large-scale finite periodic arrays. Chapter 6 discusses the development of the CBFM/AIM solver for the scattering by large-scale finite periodic arrays.

Chapter 7 provides the conclusion of the thesis.

1.4 Some Original Contributions

The author has made some original contributions to the society when doing his PhD research as listed below:

1. The author developed the the AIM solver based on SIE for the general case of electromagnetic scattering by chiral and conducting objects. The formulations incorporate situations whether the objects are pure chiral objects or hybrid chiral and conducting objects, whether the objects are separated or they are coated.

2. The author developed the AIM solver based on VSIE for the scattering by the large-scale bi-anisotropic and conducting objects.

3. The author developed the ASED-AIM solver for the solution of electromagnetic scattering by the large-scale finite periodic array problems.

4. The author developed the CBFM/AIM solver for obtaining the far-field and near-field information from finite periodic array problems.

The author also made some publications based on the contributions:

1.4.1 Book Chapters

Le-Wei Li, Ya-Nan Li and Li Hu, "Wideband and Low Loss Metamaterials for Microwave and RF Applications: Fast Algorithm and Antenna Design", in Metamaterials - Theory, Design, and Applications, Edited by Tie Jun Cui, Springer, May 2009.

1.4.2 Journal Articles

1. Li Hu, Le-Wei Li, and Raj Mittra, "Electromagnetic Scattering by Finite Periodic Arrays Using CBFM/AIM", IEEE Transactions on Antennas & Propagations, vol. 58, no. 9, pp. 3086-3090, September, 2010.

2. C.-W. Qiu, L. Hu, and S. Zouhdi, "Isotropic non-ideal cloaks providing improved invisibility by adaptive segmentation and optimal refractive index profile from ordering isotropic materials", Opt.Express, Vol. 18, Issue 14, pp. 14950-14959, 2010.

3. Li Hu, Le-Wei Li, and Tat-Soon Yeo, "Fast Solution to Electromagnetic Scattering by Large-scaled Inhomogeneous Bi-anisotropic Materials Using AIM Method", Progress In Electromagnetics Research, vol. 99, pp. 21-36, 2009

4. C.-W. Qiu, L. Hu, B. Zhang, B. Wu, S. Johnson and J. Joannopoulos, "Spherical Cloaking Using Nonlinear Transformations for Improved Segmentation into Concentric Isotropic Coatings", Opt. Express, vol. 17, pp. 13467-13478, 2009

5. Li Hu, Le-Wei Li, and Tat-Soon Yeo, "ASED-AIM Analysis of Scattering by Large-scale Finite Periodic Arrays", Progress In Electromagnetics Research B, vol. 18, pp. 381-399, 2009

6. C.-W. Qiu, L. Hu, X. Xu, and Y. Feng, "Spherical Cloaking with Homogeneous Isotropic Multilayered Structures", Phys. Rev. E, 79, 047602, 2009

1.4.3 Conference Papers

1. Li Hu and Le-Wei Li, "CBFM-Based p-FFT Method: A New Algorithm for Solving Large-Scale Finite Periodic Arrays Scattering Problems", December 7-10, 2009 Asia-Pacific Microwave Conference (APMC 2009)

2. Li Hu and Le-Wei Li, "ASED-AIM Analysis of EM Scattering by 3D Huge-Scale Finite Periodic Arrays", the 2009 International Symposium on Antennas and Propagation (ISAP 2009), October 20-23, 2009

3. Li Hu, Le-Wei Li, Wei-Bin Ewe, and Tat-Soon Yeo, "AIM Analysis of Large-scale Inhomogeneous Bi-anisotropic Scattering Problems", IEEE Antennas and Propagation Society International Symposium 2009 (APS 2009), Charleston, US, June 1-5, 2009

4. Li Hu, Le-Wei Li, Wei-Bin Ewe, and Tat-Soon Yeo, "Solving Large Scale Homogeneous Ciral Objects Scattering Problem Using AIM",

IEEE Antennas and Propagation Society International Symposium 2009 (APS 2009), Charleston, US, June 1-5, 2009

5. Li Hu, Le-Wei Li, Tat-Soon Yeo, and Ruediger Vahldieck, "An Accurate and Robust Approach for Evaluating VIE Impedance Matrix Elements Using SWG Basis Functions", (Invited Paper), Proc of 2008 Asia-Pacific Microwave Conference (APMC'08), Hong Kong/Macau, China SAR on December 16-19/19-20, 2008.

Chapter 2

Basic Idea of Adaptive Integral Method

In this chapter, we discuss in detail about the basic idea and realization of AIM. It forms the basis for later chapters since the implementation of the specific AIM solvers is modified on the basic AIM implementation.

2.1 Basic Idea of AIM

The basic idea of AIM is to approximate the far zone interaction using uniform grid points. Since the Green's function is translational invariant, the interaction between any two points is the same provided that their relative distance is the same. Therefore, the resulting impedance matrix of grid points is Toeplitz matrix and we can use FFT to accelerate the matrix vector multiplication as well as reduce the memory requirement. The algorithm of AIM can be summarized as the following four steps:

1. approximate the basis function by the associated uniform grid points, which is called the projection process;

2. calculate the grids interaction using FFT;

3. interpolate the potential calculated at grids to integration points of associated testing functions;

4. correct the near zone interaction by removing the incorrect interaction approximated by grids.

These four steps can be illustrated by Fig. 2.1. In the following sections, we detailed the realization of each of the four steps.

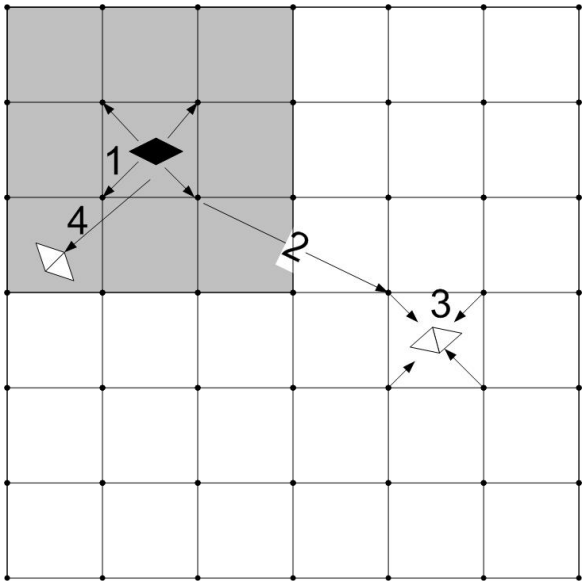

Figure 2.1: The pictorial representation of the AIM.

2.2 Detailed Implementation of AIM

2.2.1 Projection

If the source and field point are far apart, the Green's function is very smooth which can be approximated by polynomials. In this way, the basis

function can be approximated by grid points associated with it as illustrated in Fig. 2.2.

$$\gamma_n \approx \tilde{\gamma}_n = \sum_{u=1}^{(M+1)^3} \Lambda_{nu} \delta(\boldsymbol{r} - \boldsymbol{r}') \tag{2.1}$$

Where γ_n is the basis function and $\tilde{\gamma}_n$ is the approximated grid basis

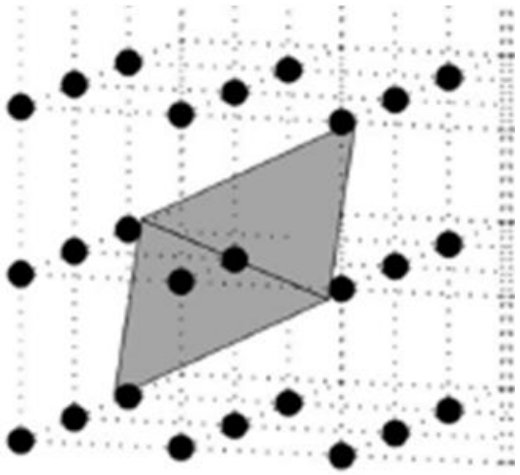

Figure 2.2: The representation of the basis function by associated grid points.

function, M is the expansion order, Λ_{nu} is the projection coefficient and $\boldsymbol{r}'$ denotes the position of the grid point. In order to calculate Λ_{nu}, we use multiple moment method. Here, Green's function is approximated by polynomials and we let the potential produced by two sets of basis functions be equal, namely,

$$\begin{aligned} &\int_{\alpha_n} \gamma_n (x - x_0)^{m1} (y - y_0)^{m2} (z - z_0)^{m3} dr \\ &= \sum_{u=1}^{(M+1)^3} (x_{nu} - x_0)^{m1} (y_{nu} - y_0)^{m2} (z_{nu} - z_0)^{m3} \Lambda_{nu} \end{aligned} \tag{2.2}$$

where $\boldsymbol{r}_0 = (x_0, y_0, z_0)$ can be chosen arbitrarily, normally, it is chosen as the center of the basis function. From this, we can obtain the projection matrix $\overline{\boldsymbol{\Lambda}}$ which is a very sparse matrix, each row has at most $(M+1)^3$ non-zero elements.

2.2.2 Grid Interaction

After we project current on basis functions to the associated grid points, we have current distribution on the grid points and we want to calculate the grid potential resulted from current on these grid points. First we consider 1D problem in which only three grid points x_1, x_2, x_3 exist along x-axis and $2x_2 = x_1 + x_3$. Then, the grid potential vector can be obtained from

$$\begin{pmatrix} g_{11} & g_{12} & g_{13} \\ g_{21} & g_{22} & g_{23} \\ g_{31} & g_{32} & g_{33} \end{pmatrix} \begin{pmatrix} I_1 \\ I_2 \\ I_3 \end{pmatrix} = \begin{pmatrix} \phi_1 \\ \phi_2 \\ \phi_3 \end{pmatrix} \tag{2.3}$$

where g_{mn} is the Green's function with m-th point as field point and n-th point as source point. I_n is the current at n-th point. ϕ_m is the potential at m-th point. since

$$g_{mn} = \frac{e^{-ik|\boldsymbol{r}_m - \boldsymbol{r}_n|}}{4\pi|\boldsymbol{r}_m - \boldsymbol{r}_n|} = g_{m-n} \tag{2.4}$$

we have

$$g_{11} = g_{22} = g_{33} = g_0 \tag{2.5}$$

$$g_{12} = g_{23} = g_{-1} \tag{2.6}$$

$$g_{21} = g_{32} = g_1 \tag{2.7}$$

we have Level 1 Toeplitz matrix

$$\begin{pmatrix} g_0 & g_{-1} & g_{-2} \\ g_1 & g_0 & g_{-1} \\ g_2 & g_1 & g_0 \end{pmatrix} \tag{2.8}$$

thus, the Toeplitz matrix vector multiplication can be done via FFT. We can introduce two vectors

$$\boldsymbol{g} = \begin{pmatrix} g_0 & g_1 & g_2 & 0 & g_{-2} & g_{-1} \end{pmatrix} \tag{2.9}$$

and

$$\boldsymbol{I} = \begin{pmatrix} I_1 & I_2 & I_3 & 0 & 0 & 0 \end{pmatrix} \tag{2.10}$$

and obtain grid potential via

$$\begin{pmatrix} \phi_1 & \phi_2 & \phi_3 & * & * & * \end{pmatrix} = \mathcal{F}^{-1}\left(\mathcal{F}(\boldsymbol{g}) \cdot \mathcal{F}(\boldsymbol{I})\right) \tag{2.11}$$

where $*$ denotes don't care term. Here, $\mathcal{F}$ and $\mathcal{F}^{-1}$ denote 1D FFT and inverse FFT respectively, $\cdot$ denotes the element-wise multiplication. Generally, we can construct $\boldsymbol{g}$ and $\boldsymbol{I}$ via

$$\boldsymbol{g}_k = \begin{cases} g_{k-1} & k \leq N_x \\ g_{k-2N_x-1} & k \geq N_x + 2 \\ 0 & \text{otherwise} \end{cases} \tag{2.12}$$

and

$$\boldsymbol{I}_k = \begin{cases} I_k & k \leq N_x \\ 0 & \text{otherwise} \end{cases} \tag{2.13}$$

where N_x denotes Number of grid points in x-direction. In order to obtain

$$\begin{pmatrix} \phi_1 \\ \phi_2 \\ \vdots \\ \phi_{N_x} \end{pmatrix} = \begin{pmatrix} g_{11} & g_{12} & \cdots & g_{1N_x} \\ g_{21} & g_{22} & \cdots & g_{2N_x} \\ \vdots & \vdots & \ddots & \vdots \\ g_{N_x} & g_{N_x} & \cdots & g_{N_xN_x} \end{pmatrix} \begin{pmatrix} I_1 \\ I_2 \\ \vdots \\ I_{N_x} \end{pmatrix} \tag{2.14}$$

we construct

$$\begin{pmatrix} \phi_1 & \phi_2 & \dots & \phi_{N_x} & * \end{pmatrix} = \mathcal{F}^{-1}\left(\mathcal{F}(\boldsymbol{g}) \cdot \mathcal{F}(\boldsymbol{I})\right) \tag{2.15}$$

For 3D problem, we have 3D Topelitz matrix-vector multiplication:

$$\begin{pmatrix} \phi_{1,1,1} \\ \vdots \\ \phi_{N_x,1,1} \\ \vdots \\ \phi_{N_x,N_y,1} \\ \vdots \\ \phi_{N_x,N_y,N_z} \end{pmatrix} = \begin{pmatrix} \overline{\boldsymbol{G}}^{(2)}_{11} & \overline{\boldsymbol{G}}^{(2)}_{12} & \dots & \overline{\boldsymbol{G}}^{(2)}_{1N_z} \\ \overline{\boldsymbol{G}}^{(2)}_{21} & \overline{\boldsymbol{G}}^{(2)}_{22} & \dots & \overline{\boldsymbol{G}}^{(2)}_{2N_z} \\ \vdots & \vdots & \ddots & \vdots \\ \overline{\boldsymbol{G}}^{(2)}_{N_z} & \overline{\boldsymbol{G}}^{(2)}_{N_z} & \dots & \overline{\boldsymbol{G}}^{(2)}_{N_zN_z} \end{pmatrix} \begin{pmatrix} I_{1,1,1} \\ \vdots \\ I_{N_x,1,1} \\ \vdots \\ I_{N_x,N_y,1} \\ \vdots \\ I_{N_x,N_y,N_z} \end{pmatrix} \tag{2.16}$$

where N_y,N_z denote Number of grid points in y-direction and z-direction respectively. $\overline{\boldsymbol{G}}^{(2)}_{mm'}$ is a Level-2 Topelitz matrix and can be written as

$$\overline{\boldsymbol{G}}^{(2)}_{mm'} = \begin{pmatrix} \overline{\boldsymbol{G}}^{(1)}_{11} & \overline{\boldsymbol{G}}^{(1)}_{12} & \dots & \overline{\boldsymbol{G}}^{(1)}_{1N_y} \\ \overline{\boldsymbol{G}}^{(1)}_{21} & \overline{\boldsymbol{G}}^{(1)}_{22} & \dots & \overline{\boldsymbol{G}}^{(1)}_{2N_y} \\ \vdots & \vdots & \ddots & \vdots \\ \overline{\boldsymbol{G}}^{(1)}_{N_y1} & \overline{\boldsymbol{G}}^{(1)}_{N_y2} & \dots & \overline{\boldsymbol{G}}^{(1)}_{N_yN_y} \end{pmatrix} \tag{2.17}$$

$\overline{\boldsymbol{G}}^{(1)}_{ll'}$ is a Level-1 Topelitz matrix and can be written as

$$\overline{\boldsymbol{G}}^{(1)}_{ll'} = \begin{pmatrix} g_{0,l-l',m-m'} & g_{-1,l-l',m-m'} & \dots & g_{1-N_x,l-l',m-m'} \\ g_{1,l-l',m-m'} & g_{0,l-l',m-m'} & \dots & g_{2-N_x,l-l',m-m'} \\ \vdots & \vdots & \ddots & \vdots \\ g_{N_x-1,l-l',m-m'} & g_{N_x-2,l-l',m-m'} & \dots & g_{0,l-l',m-m'} \end{pmatrix} \tag{2.18}$$

and we can introduce two 3D arrays

$$\boldsymbol{g}_{k,l,m} = \begin{cases} g_{k-1,l-1,m-1}, & k \le N_x, l \le N_y, m \le N_z \\ g_{k-2N_x-1,l-1,m-1} & k \ge N_x+2, l \le N_y, m \le N_z \\ g_{k-1,l-2N_y-1,m-1}, & k \le N_x, l \ge N_y+2, m \le N_z \\ g_{k-2N_x-1,l-2N_y-1,m-1} & k \ge N_x+2, l \ge N_y+2, m \le N_z \\ g_{k-1,l-1,m-2N_z-1}, & k \le N_x, l \le N_y, m \ge N_z+2 \\ g_{k-2N_x-1,l-1,m-2N_z-1} & k \ge N_x+2, l \le N_y, m \ge N_z+2 \\ g_{k-1,l-2N_y-1,m-2N_z-1}, & k \le N_x, l \ge N_y+2, m \ge N_z+2 \\ g_{k-2N_x-1,l-2N_y-1,m-2N_z-1} & k \ge N_x+2, l \ge N_y+2, m \ge N_z+2 \\ 0 & \text{otherwise} \end{cases} \tag{2.19}$$

and

$$\boldsymbol{I}_{k,l,m} = \begin{cases} I_{k,l,m} & k \le N_x, l \le N_y, m \le N_z \\ 0 & \text{otherwise} \end{cases} \tag{2.20}$$

and obtain grid potential via

$$\mathcal{F}^{-1}\left(\mathcal{F}(\boldsymbol{g}) \cdot \mathcal{F}(\boldsymbol{I})\right) \tag{2.21}$$

here, $\mathcal{F}$ denotes 3D-FFT.

2.2.3 Interpolation

After we calculate the grid potential via FFT, we can interpolate the potential to any point we want. Here, we use Lagrange polynomials as interpolation polynomials. For 1D problem, suppose we have two grid points x_1, x_2 with potential ϕ_1, ϕ_2, we would like the potential ϕ at x, we can construct

$$\phi = \phi_1 L_1(x) + \phi_2 L_2(x) \tag{2.22}$$

where $L_1(x), L_2(x)$ are Lagrange polynomials defined as

$$L_1(x) = \frac{x - x_2}{x_1 - x_2} \tag{2.23}$$

$$L_2(x) = \frac{x - x_1}{x_2 - x_1} \tag{2.24}$$

Generally, for N_x grid points, we have

$$\phi = \sum_{i=1}^{N_x} \phi_i L_i(x) \tag{2.25}$$

where

$$L_i(x) = \prod_{j=1, j\neq i}^{N_x} \frac{x - x_j}{x_i - x_j} \tag{2.26}$$

for 3D problems, we have

$$\phi = \sum_{i,j,k} \phi_{i,j,k} L_i(x) M_j(y) N_k(z) \tag{2.27}$$

where

$$L_i(x) = \prod_{j=1, j\neq i}^{N_x} \frac{x - x_j}{x_i - x_j} \tag{2.28}$$

$$M_j(y) = \prod_{k=1, k\neq j}^{N_y} \frac{y - y_k}{y_j - y_k} \tag{2.29}$$

$$N_k(z) = \prod_{l=1, l\neq k}^{N_z} \frac{z - z_l}{z_k - z_l} \tag{2.30}$$

Suppose we use central point integration for the testing functions, in this way, for each testing function, we have to interpolate the potentials at the associate grid points to the center of the testing function. Hence, we have the interpolation matrix $\overline{\mathbf{\Gamma}}$ where each row has only at most $(M+1)^3$ non-zero elements and the element can be written as

$$\Gamma_{m,i,j,k} = L_i(x) M_j(y) N_k(z) \tag{2.31}$$

2.2.4 Near Zone Correction

Although grid interaction can approximate the original basis function interaction pretty well in the far zone distance, it works badly at the near zone because the Green's function is singular when source and field points are near. Therefore, we have to directly calculate the interaction and remove the incorrect ones contributed by the grid approximation, therefore, we can define the near zone impedance matrix as

$$Z_{mn}^{\text{near}} = \begin{cases} Z_{mn} - \hat{Z}_{mn}, & \text{if } d_{mn} \leq d_{\text{near}} \\ 0, & \text{otherwise} \end{cases} \tag{2.32}$$

where Z_{mn} is directly calculated through MoM and $\hat{Z}_{mn}$ is grid approximation, d_{mn} is the distance between basis function m and n, d_{near} is the near zone threshold. As a rule of thumb, $d_{\text{near}} \approx 0.4\lambda_0$ where λ_0 is the free space wavelength.

2.2.5 Add All Together

As mentioned above, the basic idea of AIM is to split the impedance matrix vector multiplication into two parts:

$$\overline{\boldsymbol{Z}}\boldsymbol{I} = \overline{\boldsymbol{Z}}^{\text{near}}\boldsymbol{I} + \overline{\boldsymbol{Z}}^{\text{far}}\boldsymbol{I}. \tag{2.33}$$

For the near zone interaction, since $\overline{\boldsymbol{Z}}^{\text{near}}$ is a sparse matrix, we can directly calculated the matrix vector multiplication and store the sparse matrix where the memory requirement is $O(N)$ and computational time is $O(N)$ where N is the number of unknowns. For the far zone interaction, we can approximate the interaction via uniform grids. First, we project the current

on the basis functions to the associate grids by

$$\hat{\boldsymbol{I}} = \overline{\boldsymbol{\Lambda}}\boldsymbol{I}. \tag{2.34}$$

where $\hat{\boldsymbol{I}}$ is the current on the uniform grids, $\overline{\boldsymbol{\Lambda}}$ is the projection matrix obtained above. Then, we calculate the grid potential produced by grid current via FFT transform as follows

$$\hat{\boldsymbol{\phi}} = \mathcal{F}^{-1}\left\{\mathcal{F}\{\boldsymbol{g}\} \cdot \mathcal{F}\{\hat{\boldsymbol{I}}\}\right\}. \tag{2.35}$$

where $\hat{\boldsymbol{\phi}}$ is the grid potential, $\boldsymbol{g}$ is the 3D array defined above. After that, we interpolate the grid potential to the center of the testing function via

$$\boldsymbol{\phi} = \overline{\boldsymbol{\Gamma}}\hat{\boldsymbol{\phi}} \tag{2.36}$$

where $\overline{\boldsymbol{\Gamma}}$ is the interpolation matrix defined above. Finally, we correct the near zone interaction by adding $\overline{\boldsymbol{Z}}^{\text{near}}\boldsymbol{I}$. Since the projection and interpolation matrix are sparse, thus, the computer resource will be mainly consumed by FFT process, the memory requirement for the far zone interaction is $O(N)$ and computational time is $O(N \log N)$. Therefore, based on the above discussions, we finally have the implementation of AIM:

$$\overline{\boldsymbol{Z}}\boldsymbol{I} = \overline{\boldsymbol{Z}}^{\text{near}}\boldsymbol{I} + \overline{\boldsymbol{\Gamma}}\mathcal{F}^{-1}\left\{\mathcal{F}\{\boldsymbol{g}\} \cdot \mathcal{F}\{\overline{\boldsymbol{\Lambda}}\boldsymbol{I}\}\right\}. \tag{2.37}$$

Chapter 3

Scattering by Large Chiral and Conducting Objects

In this chapter, we will derive the integral equations for scattering by chiral and conducting objects and then use AIM to speed up the solution process as well as reduce the memory requirement. It is noted that we can use surface integral equations for piecewise homogeneous chiral objects due to the wave split method. It is also noted that the integral equations derived here is very general in that it can be used to deal with piecewise homogeneous media with bi-iostropic constitutive parameters, be it simple dielectric or magneto-dielectric media. Moreover, the integral equations with the presence of conducting objects are also derived so the mixed conducting and homogeneous media problems can be solved. The advantage of using surface integral equations over volume integral equations is that the number of unknowns are greatly reduced thus the electrical size of the problem in consideration is much larger than that using volume integral equations.

3.1 Surface Integral Equations

In this section, we first derive the surface integral equations for piecewise homogeneous chiral media problems. Then, we take perfect conducting object into consideration.

3.1.1 Integral equations for Chiral Objects

According to [59], the electric and magnetic fields radiated by $\boldsymbol{J}$ and $\boldsymbol{K}$ in an unbounded chiral medium characterized by ϵ, μ, ξ are given below:

$$\boldsymbol{E} = -\eta \mathcal{L}\boldsymbol{J} - \mathcal{M}\boldsymbol{K} \tag{3.1}$$

$$\boldsymbol{H} = \mathcal{M}\boldsymbol{J} - \frac{1}{\eta}\mathcal{L}\boldsymbol{K} \tag{3.2}$$

where $\eta = \sqrt{\frac{\mu}{\epsilon}}$. The operators $\mathcal{L}$ and $\mathcal{M}$ are defined as:

$$\begin{aligned}\mathcal{L}\boldsymbol{X} = \frac{j}{2}\Bigg\{&(k_+ \int_S \boldsymbol{X} G_+ dS + k_- \int_S \boldsymbol{X} G_- dS) + \nabla[\frac{1}{k_+}\int_S (\nabla' \cdot \boldsymbol{X}) G_+ dS \\ &+ \frac{1}{k_-}\int_S (\nabla' \cdot \boldsymbol{X}) G_- dS] + \nabla \times (\int_S \boldsymbol{X} G_+ dS - \int_S \boldsymbol{X} G_- dS)\Bigg\} \end{aligned} \tag{3.3}$$

$$\begin{aligned}\mathcal{M}\boldsymbol{X} = \frac{1}{2}\Bigg\{&(k_+ \int_S \boldsymbol{X} G_+ dS - k_- \int_S \boldsymbol{X} G_- dS) + \nabla[\frac{1}{k_+}\int_S (\nabla' \cdot \boldsymbol{X}) G_+ dS \\ &- \frac{1}{k_-}\int_S (\nabla' \cdot \boldsymbol{X}) G_- dS] + \nabla \times (\int_S \boldsymbol{X} G_+ dS + \int_S \boldsymbol{X} G_- dS)\Bigg\}. \end{aligned} \tag{3.4}$$

where The right-handed (+) and left-handed (-) circularly polarized wave parameters are defined as

$$k_\pm = \omega(\sqrt{\mu\epsilon} \pm \xi) \tag{3.5}$$

$$G_\pm = \frac{e^{-jk_\pm |\boldsymbol{r} - \boldsymbol{r'}|}}{4\pi |\boldsymbol{r} - \boldsymbol{r'}|} \tag{3.6}$$

When it comes to nonchiral medium, the operators will degenerate to

$$\mathcal{L}\boldsymbol{X} = jk\int_S \boldsymbol{X}GdS + \frac{j}{k}\nabla\int_S(\nabla'\cdot\boldsymbol{X})GdS \tag{3.7}$$

$$\mathcal{M}\boldsymbol{X} = \nabla\times\int_S \boldsymbol{X}GdS \tag{3.8}$$

where $k_+ = k_- = k$, and $G_+ = G_- = G$.

There are two situations for chiral objects as shown in Fig. 3.1. In

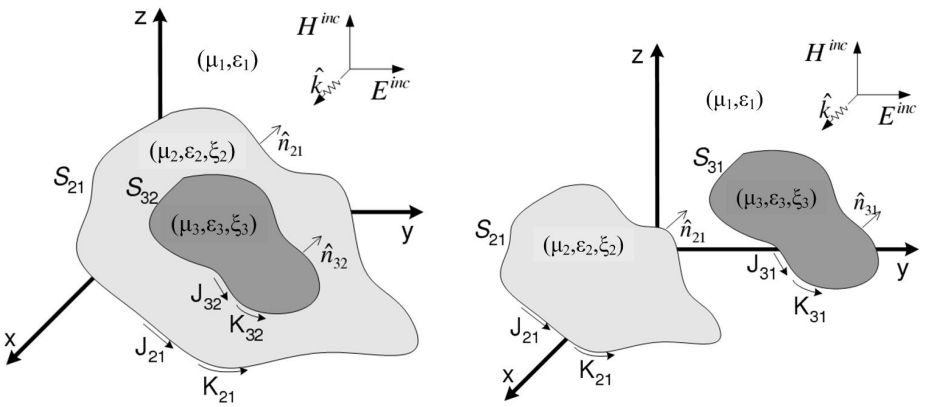

(a) coated chiral objects (b) Discrete chiral objects.

Figure 3.1: Configuration of chiral objects.

Fig. 3.1(a), one chiral object with constitutive parameters $(\mu_3, \epsilon_3, \xi_3)$ is coated by another chiral material with constitutive parameters $(\mu_2, \epsilon_2, \xi_2)$, they are embedded in a nonchiral medium with constitutive parameters (μ_1, ϵ_1). Surface electric and magnetic currents $\boldsymbol{J}_{ji}, \boldsymbol{K}_{ji}$ flow along Surface S_{ji}. Unit vectors $\widehat{\boldsymbol{n}}_{ji}$ point outward into background medium. On the outer surface S_{21}, only $\boldsymbol{J}_{21}, \boldsymbol{K}_{21}$ produce scattered fields in background medium (μ_1, ϵ_1), thus

$$\boldsymbol{J}_{21} = \widehat{\boldsymbol{n}}_{21}\times\boldsymbol{H}_1 = \widehat{\boldsymbol{n}}_{21}\times\Big\{\boldsymbol{H}^{\text{inc}} + (\mathcal{M}_1\boldsymbol{J}_{21} - \frac{1}{\eta_1}\mathcal{L}_1\boldsymbol{K}_{21})\Big\} \tag{3.9}$$

$$\boldsymbol{K}_{21} = -\widehat{\boldsymbol{n}}_{21}\times\boldsymbol{E}_1 = -\widehat{\boldsymbol{n}}_{21}\times\Big\{\boldsymbol{E}^{\text{inc}} + (-\eta_1\mathcal{L}_1\boldsymbol{J}_{21} - \mathcal{M}_1\boldsymbol{K}_{21})\Big\} \tag{3.10}$$

and on the inner surface S_{21}, $\boldsymbol{J}_{32}, \boldsymbol{K}_{32}$ and $\boldsymbol{J}_{21}, \boldsymbol{K}_{21}$ produce scattered

fields in medium $(\mu_2, \epsilon_2, \xi_2)$, thus

$$-\boldsymbol{J}_{21} = -\widehat{\boldsymbol{n}}_{21} \times \Big\{(-\mathcal{M}_2\boldsymbol{J}_{21} + \frac{1}{\eta_2}\mathcal{L}_2\boldsymbol{K}_{21}) + (\mathcal{M}_2\boldsymbol{J}_{32} - \frac{1}{\eta_2}\mathcal{L}_2\boldsymbol{K}_{32})\Big\} \quad (3.11)$$

$$-\boldsymbol{K}_{21} = \widehat{\boldsymbol{n}}_{21} \times \Big\{(\eta_2\mathcal{L}_2\boldsymbol{J}_{21} + \mathcal{M}_2\boldsymbol{K}_{21}) + (-\eta_2\mathcal{L}_2\boldsymbol{J}_{32} - \mathcal{M}_2\boldsymbol{K}_{32})\Big\} \quad (3.12)$$

Combining these two equations, we can obtain MFIE on S_{21}

$$\begin{aligned}\widehat{\boldsymbol{n}}_{21} \times \boldsymbol{H}^{\text{inc}} &= -\widehat{\boldsymbol{n}}_{21} \times (\mathcal{M}_1 + \mathcal{M}_2)\boldsymbol{J}_{21} + \widehat{\boldsymbol{n}}_{21} \times (\frac{1}{\eta_1}\mathcal{L}_1 + \frac{1}{\eta_2}\mathcal{L}_2)\boldsymbol{K}_{21} \\ &\quad + \widehat{\boldsymbol{n}}_{21} \times \mathcal{M}_2\boldsymbol{J}_{32} - \widehat{\boldsymbol{n}}_{21} \times \frac{1}{\eta_2}\mathcal{L}_2\boldsymbol{K}_{32}. \end{aligned} \quad (3.13)$$

and EFIE

$$\begin{aligned}\widehat{\boldsymbol{n}}_{21} \times \boldsymbol{E}^{\text{inc}} &= \widehat{\boldsymbol{n}}_{21} \times (\eta_1\mathcal{L}_1 + \eta_2\mathcal{L}_2)\boldsymbol{J}_{21} + \widehat{\boldsymbol{n}}_{21} \times (\mathcal{M}_1 + \mathcal{M}_2)\boldsymbol{K}_{21} \\ &\quad - \widehat{\boldsymbol{n}}_{21} \times \eta_2\mathcal{L}_2\boldsymbol{J}_{32} - \widehat{\boldsymbol{n}}_{21} \times \mathcal{M}_2\boldsymbol{K}_{32}. \end{aligned} \quad (3.14)$$

Similarly, the coupled EFIE and MFIE on the surface S_{32} can be written as

$$\begin{aligned} 0 &= \widehat{\boldsymbol{n}}_{32} \times (\eta_2\mathcal{L}_2 + \eta_3\mathcal{L}_3)\boldsymbol{J}_{32} + \widehat{\boldsymbol{n}}_{32} \times (\mathcal{M}_2 + \mathcal{M}_3)\boldsymbol{K}_{32} \\ &\quad - \widehat{\boldsymbol{n}}_{32} \times \eta_2\mathcal{L}_2\boldsymbol{J}_{21} - \widehat{\boldsymbol{n}}_{32} \times \mathcal{M}_2\boldsymbol{K}_{21} \quad (3.15) \\ 0 &= -\widehat{\boldsymbol{n}}_{32} \times (\mathcal{M}_2 + \mathcal{M}_3)\boldsymbol{J}_{32} + \widehat{\boldsymbol{n}}_{32} \times (\frac{1}{\eta_2}\mathcal{L}_2 + \frac{1}{\eta_3}\mathcal{L}_3)\boldsymbol{K}_{32} \\ &\quad + \widehat{\boldsymbol{n}}_{32} \times \mathcal{M}_2\boldsymbol{J}_{21} - \widehat{\boldsymbol{n}}_{32} \times \frac{1}{\eta_2}\mathcal{L}_2\boldsymbol{K}_{21}. \quad (3.16) \end{aligned}$$

If we repeat the same procedure for the discrete scatterers as shown in Fig. 3.1(b), we can obtain

$$\begin{aligned}\widehat{\boldsymbol{n}}_{21} \times \boldsymbol{E}^{\text{inc}} &= \widehat{\boldsymbol{n}}_{21} \times (\eta_1\mathcal{L}_1 + \eta_2\mathcal{L}_2)\boldsymbol{J}_{21} + \widehat{\boldsymbol{n}}_{21} \times (\mathcal{M}_1 + \mathcal{M}_2)\boldsymbol{K}_{21} \\ &\quad + \widehat{\boldsymbol{n}}_{21} \times \eta_1\mathcal{L}_1\boldsymbol{J}_{31} + \widehat{\boldsymbol{n}}_{21} \times \mathcal{M}_1\boldsymbol{K}_{31} \quad (3.17) \\ \widehat{\boldsymbol{n}}_{21} \times \boldsymbol{H}^{\text{inc}} &= -\widehat{\boldsymbol{n}}_{21} \times (\mathcal{M}_1 + \mathcal{M}_2)\boldsymbol{J}_{21} + \widehat{\boldsymbol{n}}_{21} \times (\frac{1}{\eta_1}\mathcal{L}_1 + \frac{1}{\eta_2}\mathcal{L}_2)\boldsymbol{K}_{21} \end{aligned}$$

$$-\hat{\boldsymbol{n}}_{21} \times \mathcal{M}_1 \boldsymbol{J}_{31} + \hat{\boldsymbol{n}}_{21} \times \frac{1}{\eta_1} \mathcal{L}_1 \boldsymbol{K}_{31} \tag{3.18}$$

$$\begin{aligned} \hat{\boldsymbol{n}}_{31} \times \boldsymbol{E}^{\text{inc}} &= \hat{\boldsymbol{n}}_{31} \times (\eta_1 \mathcal{L}_1 + \eta_3 \mathcal{L}_3) \boldsymbol{J}_{31} + \hat{\boldsymbol{n}}_{31} \times (\mathcal{M}_1 + \mathcal{M}_3) \boldsymbol{K}_{31} \\ &\quad + \hat{\boldsymbol{n}}_{31} \times \eta_1 \mathcal{L}_1 \boldsymbol{J}_{21} + \hat{\boldsymbol{n}}_{31} \times \mathcal{M}_1 \boldsymbol{K}_{21} \end{aligned} \tag{3.19}$$

$$\begin{aligned} \hat{\boldsymbol{n}}_{31} \times \boldsymbol{H}^{\text{inc}} &= -\hat{\boldsymbol{n}}_{31} \times (\mathcal{M}_1 + \mathcal{M}_3) \boldsymbol{J}_{31} + \hat{\boldsymbol{n}}_{31} \times (\frac{1}{\eta_1} \mathcal{L}_1 + \frac{1}{\eta_3} \mathcal{L}_3) \boldsymbol{K}_{31} \\ &\quad - \hat{\boldsymbol{n}}_{31} \times \mathcal{M}_1 \boldsymbol{J}_{21} + \hat{\boldsymbol{n}}_{31} \times \frac{1}{\eta_1} \mathcal{L}_1 \boldsymbol{K}_{21}. \end{aligned} \tag{3.20}$$

3.1.2 Integral Equations for Conducting and Chiral Objects

If conducting objects are present, we have to consider their contribution. There are two situations as shown in Fig. 3.2. In Fig. 3.2(a), one con-

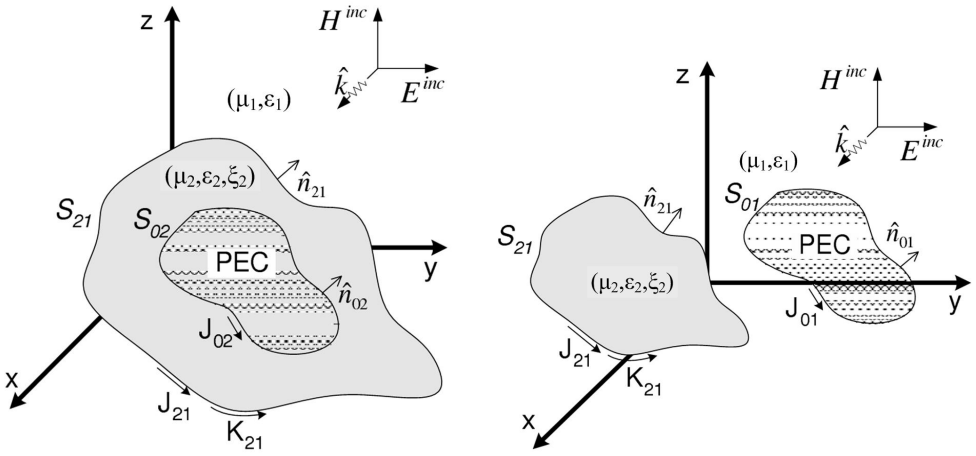

(a) conducting object coated with chiral material (b) Discrete chiral and conducting objects.

Figure 3.2: Configuration of chiral and perfectly conducting scatterers.

ducting object is coated by a chiral material with constitutive parameters $(\mu_2, \epsilon_2, \xi_2)$, they are embedded in a nonchiral medium with constitutive parameters (μ_1, ϵ_1). Surface electric and magnetic currents $\boldsymbol{J}_{ji}, \boldsymbol{K}_{ji}$ flow along Surface S_{ji}. Unit vectors $\hat{\boldsymbol{n}}_{ji}$ point outward into background medium. On the outer surface S_{21}, only $\boldsymbol{J}_{21}, \boldsymbol{K}_{21}$ produce scattered fields in background

medium (μ_1, ϵ_1), thus

$$\boldsymbol{J}_{21} = \hat{\boldsymbol{n}}_{21} \times \boldsymbol{H}_1 = \hat{\boldsymbol{n}}_{21} \times \Big\{ \boldsymbol{H}^{\text{inc}} + (\mathcal{M}_1 \boldsymbol{J}_{21} - \frac{1}{\eta_1} \mathcal{L}_1 \boldsymbol{K}_{21}) \Big\} \quad (3.21)$$

$$\boldsymbol{K}_{21} = -\hat{\boldsymbol{n}}_{21} \times \boldsymbol{E}_1 = -\hat{\boldsymbol{n}}_{21} \times \Big\{ \boldsymbol{E}^{\text{inc}} + (-\eta_1 \mathcal{L}_1 \boldsymbol{J}_{21} - \mathcal{M}_1 \boldsymbol{K}_{21}) \Big\} \quad (3.22)$$

and on the inner surface S_{21}, $\boldsymbol{J}_{02}$ and $\boldsymbol{J}_{21}, \boldsymbol{K}_{21}$ produce scattered fields in medium $(\mu_2, \epsilon_2, \xi_2)$, thus

$$-\boldsymbol{J}_{21} = -\hat{\boldsymbol{n}}_{21} \times \Big\{ (-\mathcal{M}_2 \boldsymbol{J}_{21} + \frac{1}{\eta_2} \mathcal{L}_2 \boldsymbol{K}_{21}) + (\mathcal{M}_2 \boldsymbol{J}_{02}) \Big\} \quad (3.23)$$

$$-\boldsymbol{K}_{21} = \hat{\boldsymbol{n}}_{21} \times \Big\{ (\eta_2 \mathcal{L}_2 \boldsymbol{J}_{21} + \mathcal{M}_2 \boldsymbol{K}_{21}) + (-\eta_2 \mathcal{L}_2 \boldsymbol{J}_{02}) \Big\} \quad (3.24)$$

Therefore, we have EFIE and MFIE on S_{21}

$$\begin{aligned} \hat{\boldsymbol{n}}_{21} \times \boldsymbol{E}^{\text{inc}} &= \hat{\boldsymbol{n}}_{21} \times (\eta_1 \mathcal{L}_1 + \eta_2 \mathcal{L}_2) \boldsymbol{J}_{21} + \hat{\boldsymbol{n}}_{21} \times (\mathcal{M}_1 + \mathcal{M}_2) \boldsymbol{K}_{21} \\ &\quad -\hat{\boldsymbol{n}}_{21} \times \eta_2 \mathcal{L}_2 \boldsymbol{J}_{02} \quad (3.25) \\ \hat{\boldsymbol{n}}_{21} \times \boldsymbol{H}^{\text{inc}} &= -\hat{\boldsymbol{n}}_{21} \times (\mathcal{M}_1 + \mathcal{M}_2) \boldsymbol{J}_{21} + \hat{\boldsymbol{n}}_{21} \times (\frac{1}{\eta_1} \mathcal{L}_1 + \frac{1}{\eta_2} \mathcal{L}_2) \boldsymbol{K}_{21} \\ &\quad +\hat{\boldsymbol{n}}_{21} \times \mathcal{M}_2 \boldsymbol{J}_{02}. \quad (3.26) \end{aligned}$$

On the surface of the S_{02}, we have

$$\begin{aligned} \hat{\boldsymbol{n}}_{02} \times \eta_2 \mathcal{L}_2 \boldsymbol{J}_{02} &= \hat{\boldsymbol{n}}_{02} \times \eta_2 \mathcal{L}_2 \boldsymbol{J}_{21} + \hat{\boldsymbol{n}}_{02} \times \mathcal{M}_2 \boldsymbol{K}_{21} \quad (3.27) \\ \boldsymbol{J}_{02} - \hat{\boldsymbol{n}}_{02} \times \mathcal{M}_2 \boldsymbol{J}_{02} &= -\hat{\boldsymbol{n}}_{02} \times \mathcal{M}_2 \boldsymbol{J}_{21} + \hat{\boldsymbol{n}}_{02} \times \frac{1}{\eta_2} \mathcal{L}_2 \boldsymbol{K}_{21}. \quad (3.28) \end{aligned}$$

In order to avoid internal resonance and make the impedance matrix well conditioned, we should combine the two equations above and arrive at the combined field integral equation as follows, where $0 \leq \alpha \leq 1$:

$$\begin{aligned} 0 &= \hat{\boldsymbol{n}}_{02} \times \Big\{ \alpha(\eta_2 \mathcal{L}_2 \boldsymbol{J}_{21} + \mathcal{M}_2 \boldsymbol{K}_{21} - \eta_2 \mathcal{L}_2 \boldsymbol{J}_{02}) + (1-\alpha)(-\eta_2 \mathcal{M}_2 \boldsymbol{J}_{21} \\ &\quad +\mathcal{L}_2 \boldsymbol{K}_{21} + \eta_2 \mathcal{M}_2 \boldsymbol{J}_{02}) \Big\} - (1-\alpha)\eta_2 \boldsymbol{J}_{02}. \quad (3.29) \end{aligned}$$

Now we consider the conducting scatterer placed beside a discrete chiral scatterer as shown in Fig. 3.2(b). By following the same procedure, the integral equations on the surface of the discrete chiral scatterer become

$$\begin{aligned}\widehat{\boldsymbol{n}}_{21}\times\boldsymbol{E}^{\text{inc}} &= \widehat{\boldsymbol{n}}_{21}\times(\eta_1\mathcal{L}_1+\eta_2\mathcal{L}_2)\boldsymbol{J}_{21}+\widehat{\boldsymbol{n}}_{21}\times(\mathcal{M}_1+\mathcal{M}_2)\boldsymbol{K}_{21}\\ &\quad +\widehat{\boldsymbol{n}}_{21}\times\eta_1\mathcal{L}_1\boldsymbol{J}_{01} \qquad (3.30)\\ \widehat{\boldsymbol{n}}_{21}\times\boldsymbol{H}^{\text{inc}} &= -\widehat{\boldsymbol{n}}_{21}\times(\mathcal{M}_1+\mathcal{M}_2)\boldsymbol{J}_{21}+\widehat{\boldsymbol{n}}_{21}\times(\frac{1}{\eta_1}\mathcal{L}_1+\frac{1}{\eta_2}\mathcal{L}_2)\boldsymbol{K}_{21}\\ &\quad -\widehat{\boldsymbol{n}}_{21}\times\mathcal{M}_1\boldsymbol{J}_{01}. \qquad (3.31)\end{aligned}$$

The integral equations on the surface of the discrete conducting scatterer are

$$\boldsymbol{E}^{\text{inc}}=\widehat{\boldsymbol{n}}_{01}\times\{\eta_1\mathcal{L}_1\boldsymbol{J}_{01}+\eta_1\mathcal{L}_1\boldsymbol{J}_{21}+\mathcal{M}_1\boldsymbol{K}_{21}\} \qquad (3.32)$$

$$\widehat{\boldsymbol{n}}_{01}\times\boldsymbol{H}^{\text{inc}}=\boldsymbol{J}_{01}-\widehat{\boldsymbol{n}}_{01}\times\left\{\mathcal{M}_1\boldsymbol{J}_{01}-\mathcal{M}_1\boldsymbol{J}_{21}+\frac{1}{\eta_1}\mathcal{L}_1\boldsymbol{K}_{21}\right\}. \qquad (3.33)$$

In order to avoid internal resonance and make the impedance matrix well conditioned, we should combine the two equations above and arrive at the combined field integral equation as follows, where $0\le\alpha\le1$:

$$\begin{aligned}&\widehat{\boldsymbol{n}}_{01}\times\left\{\alpha\boldsymbol{E}^{\text{inc}}+(1-\alpha)\eta_1\boldsymbol{H}^{\text{inc}}\right\}\\ =\;&(1-\alpha)\eta_1\boldsymbol{J}_{01}+\widehat{\boldsymbol{n}}_{01}\times\left\{\alpha(\eta_1\mathcal{L}_1\boldsymbol{J}_{21}+\mathcal{M}_1\boldsymbol{K}_{21}+\eta_1\mathcal{L}_1\boldsymbol{J}_{01})\right.\\ +\;&\left.(1-\alpha)(-\eta_1\mathcal{M}_1\boldsymbol{J}_{21}+\mathcal{L}_1\boldsymbol{K}_{21}-\eta_1\mathcal{M}_1\boldsymbol{J}_{01})\right\}. \qquad (3.34)\end{aligned}$$

3.2 Method of Moments for Chiral and Conducting Objects

This section discusses the discretization of the above mentioned integral equations into matrix equations. Using RWG basis functions, we can express the surface equivalent electric and magnetic current $\boldsymbol{J}_{ji}$ and $\boldsymbol{K}_{ji}$ (j = 2 or 3 or 0) as follows:

$$\boldsymbol{J}_{ji} = \sum I_{n_j} \boldsymbol{f}_{n_j} \tag{3.35}$$

$$\boldsymbol{K}_{ji} = \sum M_{n_j} \boldsymbol{f}_{n_j}. \tag{3.36}$$

For mixed chiral objects, substituting Eqns. (3.35)-(3.36) into Eqns. (3.15)-(3.20), and applying the Galerkin's testing procedure, we convert the integral equations to a linear equation system written as

$$\begin{pmatrix} \overline{\boldsymbol{Z}}^{E_2 I_2} & \overline{\boldsymbol{Z}}^{E_2 M_2} & \theta\overline{\boldsymbol{Z}}^{E_2 I_3} & \theta\overline{\boldsymbol{Z}}^{E_2 M_3} \\ \overline{\boldsymbol{Z}}^{H_2 I_2} & \overline{\boldsymbol{Z}}^{H_2 M_2} & \theta\overline{\boldsymbol{Z}}^{H_2 I_3} & \theta\overline{\boldsymbol{Z}}^{H_2 M_3} \\ \theta\overline{\boldsymbol{Z}}^{E_3 I_2} & \theta\overline{\boldsymbol{Z}}^{E_3 M_2} & \overline{\boldsymbol{Z}}^{E_3 I_3} & \overline{\boldsymbol{Z}}^{E_3 M_3} \\ \theta\overline{\boldsymbol{Z}}^{H_3 I_2} & \theta\overline{\boldsymbol{Z}}^{H_3 M_2} & \overline{\boldsymbol{Z}}^{H_3 I_3} & \overline{\boldsymbol{Z}}^{H_3 M_3} \end{pmatrix} \begin{pmatrix} I_2 \\ M_2 \\ I_3 \\ M_3 \end{pmatrix} = \begin{pmatrix} E_2 \\ H_2 \\ \delta E_3 \\ \delta H_3 \end{pmatrix} \tag{3.37}$$

where the (I_2, M_2) and (I_3, M_3) are the coefficients of the equivalent electric and magnetic current densities on S_{2i} and S_{3i}, respectively. The elements of the sub-matrices are defined as

$$Z_{mn}^{E_2 I_2} = \int_{T_{m_2}} \boldsymbol{f}_{m_2} \cdot (\eta_1 \mathcal{L}_1 + \eta_2 \mathcal{L}_2) \boldsymbol{f}_{n_2} dS_{m_2} \tag{3.38}$$

$$Z_{mn}^{E_2 M_2} = \int_{T_{m_2}} \boldsymbol{f}_{m_2} \cdot (\mathcal{M}_1 + \mathcal{M}_2) \boldsymbol{f}_{n_2} dS_{m_2} \tag{3.39}$$

$$Z_{mn}^{E_2 I_3} = -\int_{T_{m_2}} \boldsymbol{f}_{m_2} \cdot (\eta_2 \mathcal{L}_2) \boldsymbol{f}_{n_3} dS_{m_2} \tag{3.40}$$

$$Z_{mn}^{E_2 M_3} = -\int_{T_{m_2}} \boldsymbol{f}_{m_2} \cdot (\mathcal{M}_2) \boldsymbol{f}_{n_3} dS_{m_2} \tag{3.41}$$

$$Z_{mn}^{H_2 I_2} = -\int_{T_{m_2}} \boldsymbol{f}_{m_2} \cdot (\mathcal{M}_1 + \mathcal{M}_2) \boldsymbol{f}_{n_2} dS_{m_2} \tag{3.42}$$

$$Z_{mn}^{H_2M_2} = \int_{T_{m_2}} \boldsymbol{f}_{m_2} \cdot (\frac{1}{\eta_1}\mathcal{L}_1 + \frac{1}{\eta_2}\mathcal{L}_2)\boldsymbol{f}_{n_2} dS_{m_2} \tag{3.43}$$

$$Z_{mn}^{H_2I_3} = \int_{T_{m_2}} \boldsymbol{f}_{m_2} \cdot (\mathcal{M}_2)\boldsymbol{f}_{n_3} dS_{m_2} \tag{3.44}$$

$$Z_{mn}^{H_2M_3} = -\int_{T_{m_2}} \boldsymbol{f}_{m_2} \cdot (\frac{1}{\eta_2}\mathcal{L}_2)\boldsymbol{f}_{n_3} dS_{m_2} \tag{3.45}$$

$$Z_{mn}^{E_3I_2} = -\int_{T_{m_3}} \boldsymbol{f}_{m_3} \cdot (\eta_2\mathcal{L}_2)\boldsymbol{f}_{n_2} dS_{m_3} \tag{3.46}$$

$$Z_{mn}^{E_3M_2} = -\int_{T_{m_3}} \boldsymbol{f}_{m_3} \cdot (\mathcal{M}_2)\boldsymbol{f}_{n_2} dS_{m_3} \tag{3.47}$$

$$Z_{mn}^{E_3I_3} = \int_{T_{m_3}} \boldsymbol{f}_{m_3} \cdot (\eta_2\mathcal{L}_2 + \eta_3\mathcal{L}_3)\boldsymbol{f}_{n_3} dS_{m_3} \tag{3.48}$$

$$Z_{mn}^{E_3M_3} = \int_{T_{m_3}} \boldsymbol{f}_{m_3} \cdot (\mathcal{M}_2 + \mathcal{M}_3)\boldsymbol{f}_{n_3} dS_{m_3} \tag{3.49}$$

$$Z_{mn}^{H_3I_2} = \int_{T_{m_3}} \boldsymbol{f}_{m_3} \cdot (\mathcal{M}_2)\boldsymbol{f}_{n_2} dS_{m_3} \tag{3.50}$$

$$Z_{mn}^{H_3M_2} = -\int_{T_{m_3}} \boldsymbol{f}_{m_3} \cdot (\frac{1}{\eta_2}\mathcal{L}_2)\boldsymbol{f}_{n_2} dS_{m_3} \tag{3.51}$$

$$Z_{mn}^{H_3I_3} = -\int_{T_{m_3}} \boldsymbol{f}_{m_3} \cdot (\mathcal{M}_2 + \mathcal{M}_3)\boldsymbol{f}_{n_3} dS_{m_3} \tag{3.52}$$

$$Z_{mn}^{H_3M_3} = \int_{T_{m_3}} \boldsymbol{f}_{m_3} \cdot (\frac{1}{\eta_2}\mathcal{L}_2 + \frac{1}{\eta_3}\mathcal{L}_3)\boldsymbol{f}_{n_3} dS_{m_3}. \tag{3.53}$$

The elements of the excitation electric and magnetic fields are thus expressed as

$$E_{2,m} = \int_{T_{m_2}} \boldsymbol{f}_{m_2} \cdot \boldsymbol{E}^{\text{inc}} dS_{m_2} \tag{3.54}$$

$$H_{2,m} = \int_{T_{m_2}} \boldsymbol{f}_{m_2} \cdot \boldsymbol{H}^{\text{inc}} dS_{m_2} \tag{3.55}$$

$$E_{3,m} = \int_{T_{m_3}} \boldsymbol{f}_{m_3} \cdot \boldsymbol{E}^{\text{inc}} dS_{m_3} \tag{3.56}$$

$$H_{3,m} = \int_{T_{m_3}} \boldsymbol{f}_{m_3} \cdot \boldsymbol{H}^{\text{inc}} dS_{m_3}. \tag{3.57}$$

For cases shown in Fig. 3.1(a) and Fig. 3.1(b), we let $(\delta = 0, \theta = 1)$ and $(\delta = 1, \theta = -1)$ in Eqn. (3.37) respectively. The scattering by the single chiral scatterer can be considered as the special case of mixed chiral scatterers. The matrix equation can be directly obtained as

$$\begin{pmatrix} \overline{\boldsymbol{Z}}^{E_2I_2} & \overline{\boldsymbol{Z}}^{E_2M_2} \\ \overline{\boldsymbol{Z}}^{H_2I_2} & \overline{\boldsymbol{Z}}^{H_2M_2} \end{pmatrix} \begin{pmatrix} I_2 \\ M_2 \end{pmatrix} = \begin{pmatrix} E_2 \\ H_2 \end{pmatrix}. \tag{3.58}$$

For composite chiral and conducting objects, substituting Eqns. (3.35)-(3.36) into Eqns. (3.25)-(3.34), and applying the Galerkin's testing procedure, we convert the integral equations to a linear equation system written as

$$\begin{pmatrix} \overline{\boldsymbol{Z}}^{E_2 I_2} & \overline{\boldsymbol{Z}}^{E_2 M_2} & \theta\overline{\boldsymbol{Z}}^{E_2 I_0} \\ \overline{\boldsymbol{Z}}^{H_2 I_2} & \overline{\boldsymbol{Z}}^{H_2 M_2} & \theta\overline{\boldsymbol{Z}}^{H_2 I_0} \\ \theta\overline{\boldsymbol{Z}}^{E_0 I_2} & \theta\overline{\boldsymbol{Z}}^{E_0 M_2} & \overline{\boldsymbol{Z}}^{E_0 I_0} \end{pmatrix} \begin{pmatrix} I_2 \\ M_2 \\ I_0 \end{pmatrix} = \begin{pmatrix} E_2 \\ H_2 \\ \delta E_0 \end{pmatrix} \tag{3.59}$$

where I_0 stands for coefficients of the equivalent electric current density on S_{0i} and the (I_2, M_2) are the coefficients of the equivalent electric and magnetic current densities on S_{2i}, respectively. The elements of the submatrices are defined as

$$Z_{mn}^{E_2 I_2} = \int_{T_{m_2}} \boldsymbol{f}_{m_2} \cdot (\eta_1 \mathcal{L}_1 + \eta_2 \mathcal{L}_2) \boldsymbol{f}_{n_2} dS_{m_2} \tag{3.60}$$

$$Z_{mn}^{E_2 M_2} = \int_{T_{m_2}} \boldsymbol{f}_{m_2} \cdot (\mathcal{M}_1 + \mathcal{M}_2) \boldsymbol{f}_{n_2} dS_{m_2} \tag{3.61}$$

$$Z_{mn}^{E_2 I_0} = -\int_{T_{m_2}} \boldsymbol{f}_{m_2} \cdot (\eta_2 \mathcal{L}_2) \boldsymbol{f}_{n_0} dS_{m_2} \tag{3.62}$$

$$Z_{mn}^{H_2 I_2} = -\int_{T_{m_2}} \boldsymbol{f}_{m_2} \cdot (\mathcal{M}_1 + \mathcal{M}_2) \boldsymbol{f}_{n_2} dS_{m_2} \tag{3.63}$$

$$Z_{mn}^{H_2 M_2} = \int_{T_{m_2}} \boldsymbol{f}_{m_2} \cdot (\frac{1}{\eta_1} \mathcal{L}_1 + \frac{1}{\eta_2} \mathcal{L}_2) \boldsymbol{f}_{n_2} dS_{m_2} \tag{3.64}$$

$$Z_{mn}^{H_2 I_0} = \int_{T_{m_2}} \boldsymbol{f}_{m_2} \cdot (\mathcal{M}_2) \boldsymbol{f}_{n_0} dS_{m_2} \tag{3.65}$$

$$Z_{mn}^{E_0 I_2} = \int_{T_{m_0}} \boldsymbol{f}_{m_0} \cdot (\alpha\eta_2 \mathcal{L}_2 - (1-\alpha)\eta_2 \mathcal{M}_2) \boldsymbol{f}_{n_2} dS_{m_0} \tag{3.66}$$

$$Z_{mn}^{E_0 M_2} = \int_{T_{m_0}} \boldsymbol{f}_{m_0} \cdot (\alpha\mathcal{M}_2 + (1-\alpha)\mathcal{L}_2) \boldsymbol{f}_{n_2} dS_{m_0} \tag{3.67}$$

$$Z_{mn}^{E_0 I_0} = \int_{T_{m_0}} \boldsymbol{f}_{m_0} \cdot (-\alpha\eta_2 \mathcal{L}_2 + (1-\alpha)\eta_2 \mathcal{M}_2) \boldsymbol{f}_{n_0} dS_{m_0}. \tag{3.68}$$

The elements of the excitation electric and magnetic fields are expressed as

$$E_{2,m} = \int_{T_{m_2}} \boldsymbol{f}_{m_2} \cdot \boldsymbol{E}^{\text{inc}} dS_{m_2} \tag{3.69}$$

$$H_{2,m} = \int_{T_{m_2}} \boldsymbol{f}_{m_2} \cdot \boldsymbol{H}^{\text{inc}} dS_{m_2} \tag{3.70}$$

$$E_{0,m} = \int_{T_{m_0}} \boldsymbol{f}_{m_0} \cdot (\alpha \boldsymbol{E}^{\text{inc}} + (1-\alpha)\eta_1 \boldsymbol{H}^{\text{inc}}) dS_{m_0}. \tag{3.71}$$

For our problem, we let $(\delta = 0, \theta = 1)$ and $(\delta = 1, \theta = -1)$ in Eqn. (3.59) for cases shown in Fig. 3.2(a) and Fig. 3.2(b), respectively.

3.3 Accuracy and Complexity of the Chiral AIM Solver

This section discusses about the accuracy and complexity of the chiral AIM solver. First, we discuss about the accuracy. We set up a numerical experiment to test how well the approximation of AIM to MoM is in the far zone distance and how far we should choose as the far zone distance. In this experiment, we consider a conducting sphere with radius $1.0\lambda_0$ coated with chiral material with thickness $0.1\lambda_0$, constitutive parameters $\epsilon_r = 2$, $\mu_r = 1$, and $\xi_r = 0.3$. This experiment is general in that it considers both chiral and conducting objects. The objects are discretized into triangle meshes with average side length $0.1\lambda_0$. Then, we define the relative error as

$$\Delta Z_{mn} = \frac{|Z_{mn} - \hat{Z}_{mn}|}{|Z_{mn}|}. \tag{3.72}$$

where Z_{mn} is the impedance matrix element calculated by MoM and $\hat{Z}_{mn}$ is the impedance matrix element calculated by AIM. we take Z_{mn}^{EI} as an example. Similar calculations can be also carried out for other impedance matrix elements. The ΔZ_{mn} is plotted as a function of the distance between elements for different grid sizes, as shown in Fig. 3.3. From Fig. 3.3, it is clear that $\hat{Z}_{mn}$ approximates Z_{mn} very well at far zone distance, e.g., $0.4\lambda_0$. The results also show that the smaller the grid size, the more accurate the approximation is. Since reducing grid size could increase the FFT vector size, we have to choose an appropriate grid size as a compromise to balance the required accuracy and the given computer resources. Throughout this

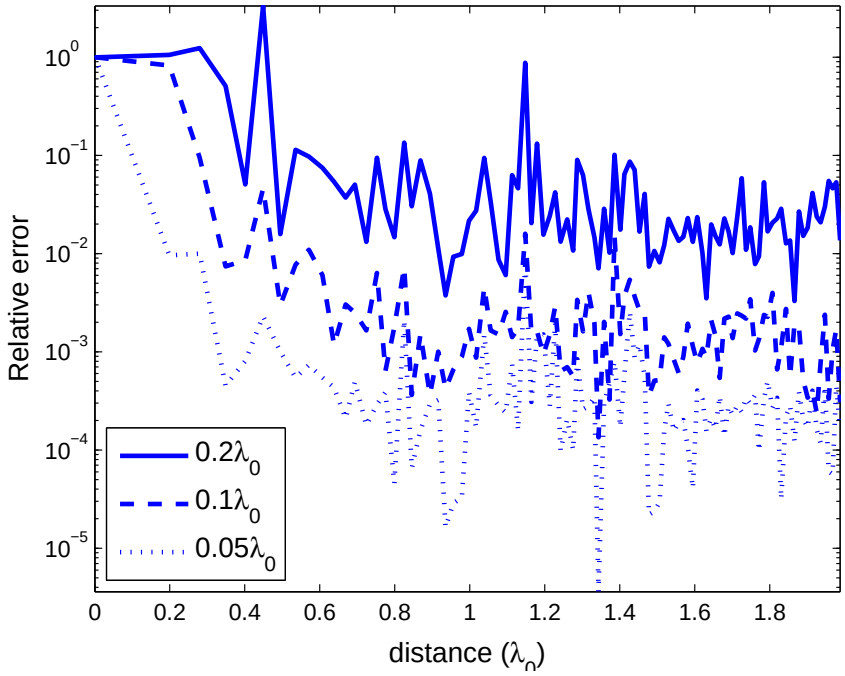

Figure 3.3: The relative error of for matrix elements of Z_{mn}^{EI} using different grid sizes.

paper, we choose a grid size of $0.1\lambda_0$ since the accuracy of 1% relative error is good enough for most engineering applications.

Next, we explore the computational complexity and storage requirement of our AIM implementation. The matrix storage requirement and CPU time per iteration are plotted in Fig. 3.4. From it, it is clear that AIM solver has a very small requirement on memory as well as computational time, since the ordinary MoM solver requires $O(N^2)$ for memory and $O(N^3)$ for computational time.

3.4 Numerical Results

In this section, we will present several examples to demonstrate the accuracy and applicability of our AIM implementation to solve the scattering problems of chiral and conducting objects formulated using the SIE

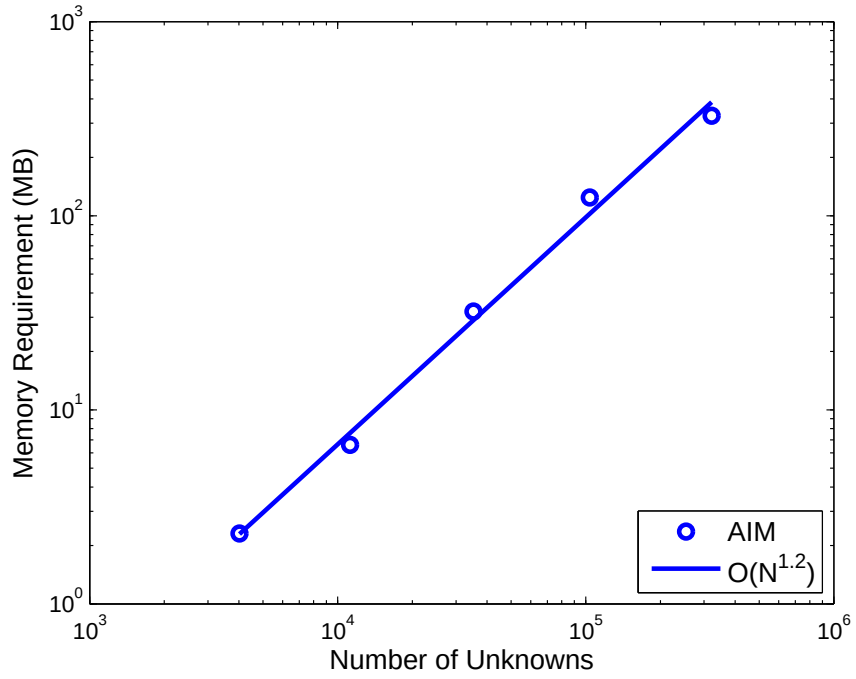

(a)

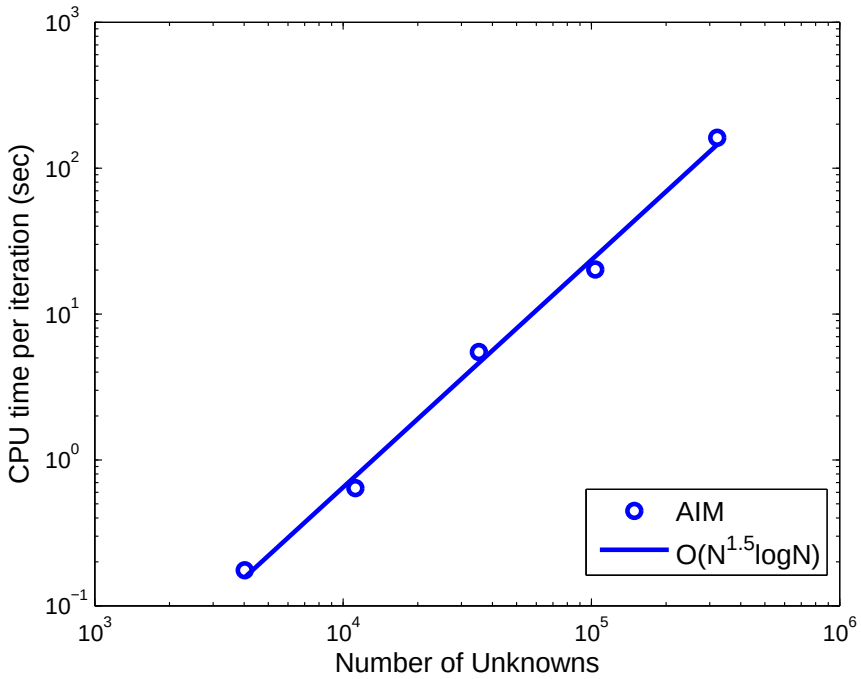

(b)

Figure 3.4: (a) Memory requirement and (b) CPU time for the AIM solver versus the number of unknowns N.

method. If not specified, the objects are illuminated by a θ-polarized plane wave with incident angle of $\theta^{\text{inc}} = 0^o$ and $\phi^{\text{inc}} = 0^o$.

3.4.1 A Multilayered Chiral Sphere

In the first example, in order to test the accuracy of our AIM solver for the coated chiral scatterers, we consider a coated chiral sphere with inner diameter $d_1 = 3.0\lambda_0$ and outer diameter $d_2 = 6.0\lambda_0$, where λ_0 is the free space wavelength. The constitutive parameters for the two layers are the same: $\epsilon_r = 2$, $\mu_r = 1$ and $\xi_r = 0.4$ where $\epsilon = \epsilon_0\epsilon_r$, $\mu = \mu_0\mu_r$, and $\xi = \xi_r\sqrt{\epsilon\mu}$. The total number of unknowns is $N = 228,904$. Fig. 3.5 shows the bistatic RCS of the chiral sphere calculated using our code and also the exact Mie series for comparison. In these figures, the first subscript from the right on σ denotes the transmitter's polarization and the second denotes the receiver's polarization. From Fig. 3.5, we can conclude that the RCS results calculated from our code agree well with those exact solutions in terms of the Mie series.

3.4.2 Nine Chiral Spheres

A nine-sphere scattering problem shown in Fig. 3.6 is studied in this subsection. The diameter of each sphere is $2\lambda_0$, of which five spheres (in yellow) have relative permittivity $\epsilon_{r1} = 1.75 - j0.3$ and four spheres (in green) have relative permittivity $\epsilon_{r2} = 2.25 - j0.5$. The $\xi_r = 0$ for all the spheres. There is no spacing among the adjacent cells. The spheres are illuminated by a θ-polarized plane wave at an incident angle of $\theta^{\text{inc}} = 90^o$ and $\phi^{\text{inc}} = 180^o$. The bistatic RCS result is calculated using 290,063 unknowns and shown in Fig. 3.6(b). Also the result from [18] is shown for comparison and a good agreement has been observed.

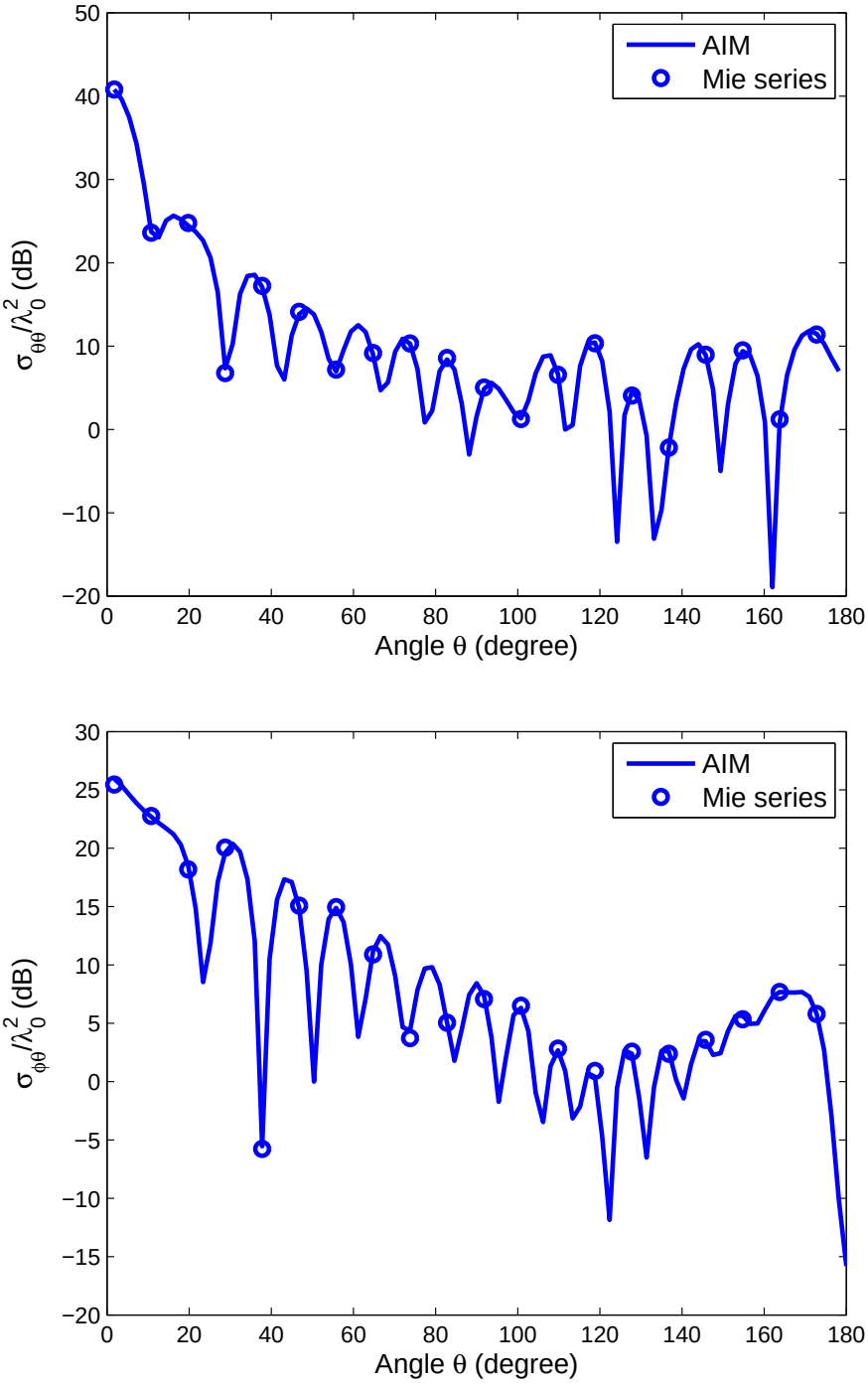

Figure 3.5: Bistatic RCS in x-z plane of a multilayered chiral sphere. (a) Co-polarized bistatic RCS; (b) Cross-polarized bistatic RCS.

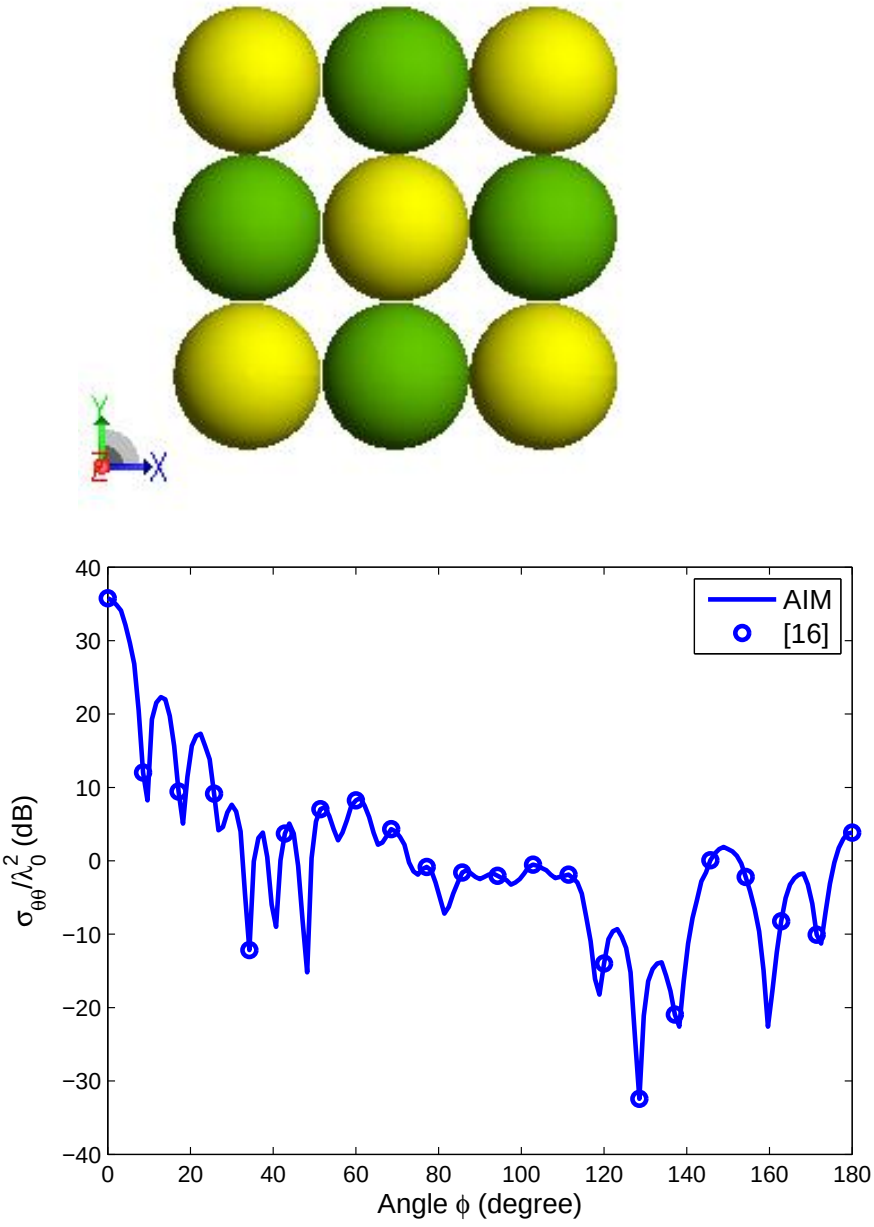

Figure 3.6: (a)Configuration of nine spheres with $\epsilon_{r1} = 1.75 - j0.3$, $\epsilon_{r2} = 2.25 - j0.5$ and $\xi_r = 0$. The diameter of each sphere is $2\lambda_0$. (b) Bistatic RCS of nine spheres in x-y plane.

3.4.3 A PEC Sphere with Chiral Coating

In the third example, we consider a PEC sphere with diameter $d = 1.8\lambda_0$, coated with a chiral material with a thickness of $0.1\lambda_0$. The constitutive parameters for the chiral material are: $\epsilon_r = 2.667$, $\mu_r = 1.333$ and $\xi_r = 0.5$. The total number of unknowns is $N = 203,748$. The chiral sphere is illuminated by a plane wave with $\widehat{\boldsymbol{k}}$ towards the z-direction and $\boldsymbol{E}$ in the x-direction. Fig. 3.7 shows the bistatic RCS of the chiral sphere calculated using our code and also the Mie series for comparison. From Fig. 3.7, we can conclude that the RCS results calculated from our code agree well with those of the Mie series.

3.4.4 Four Chiral Spheres Over a PEC Plane

The last example considered is a system consisting of four spheres on the top of a PEC plate shown in Fig. 3.8(a). There is no spacing among adjacent spheres. The diameter of each sphere is $2\lambda_0$ and the relative permittivity of each of the spheres is $\epsilon_r = 1.6 - 0.4j$ and $\xi_r = 0$. The $8\lambda_0 \times 8\lambda_0$ PEC plate is placed at $z = 0$ and the centers of the spheres are located $1.3\lambda_0$ above the PEC plate. The bistatic RCS is computed using 230,984 unknowns and shown in Fig. 3.8(b). Also shown is the result from [18]. A good agreement has been observed.

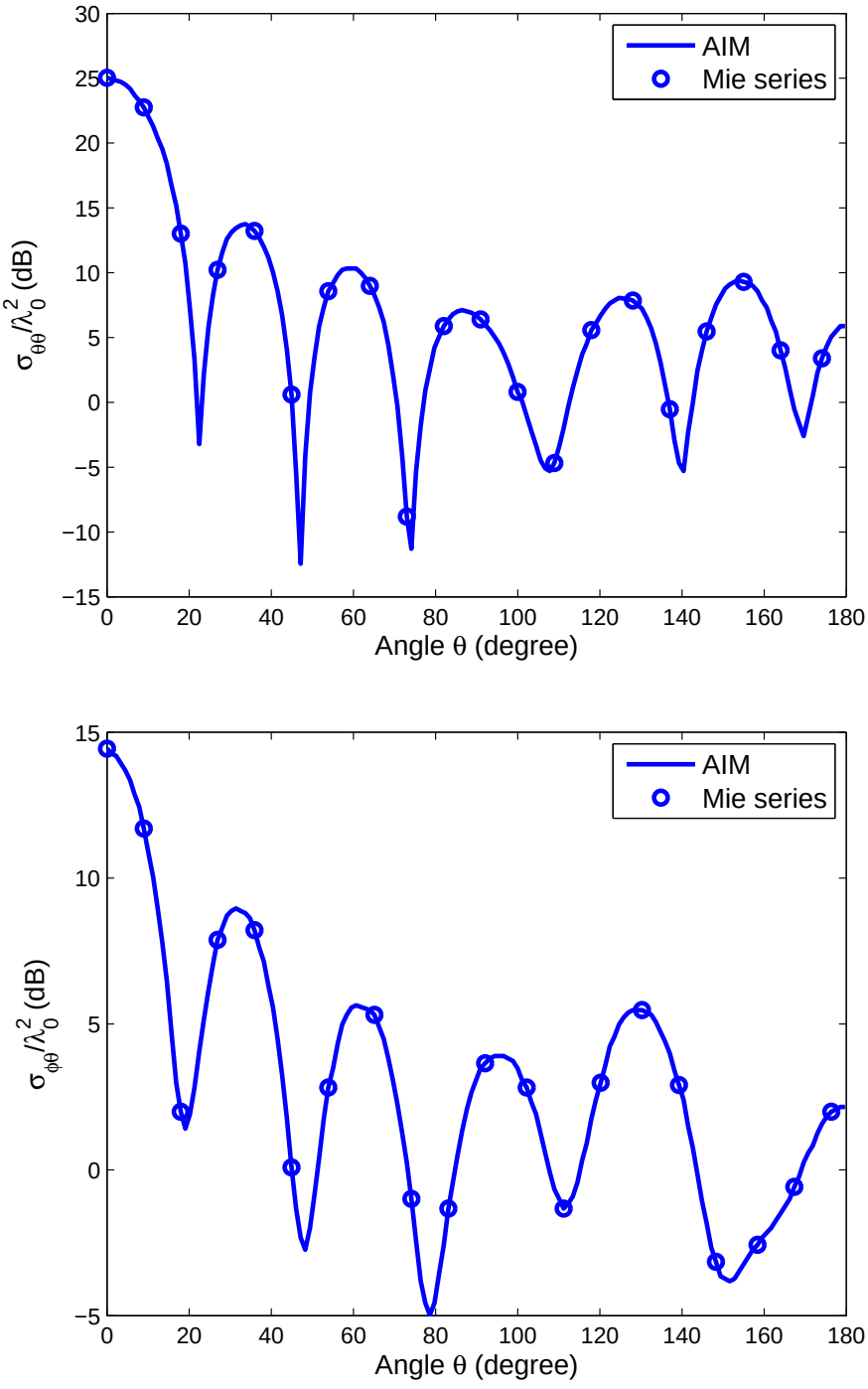

Figure 3.7: Bistatic RCS in x-z plane of a conducting sphere coated with chiral material. (a) Co-polarized bistatic RCS; (b) cross-polarized bistatic RCS.

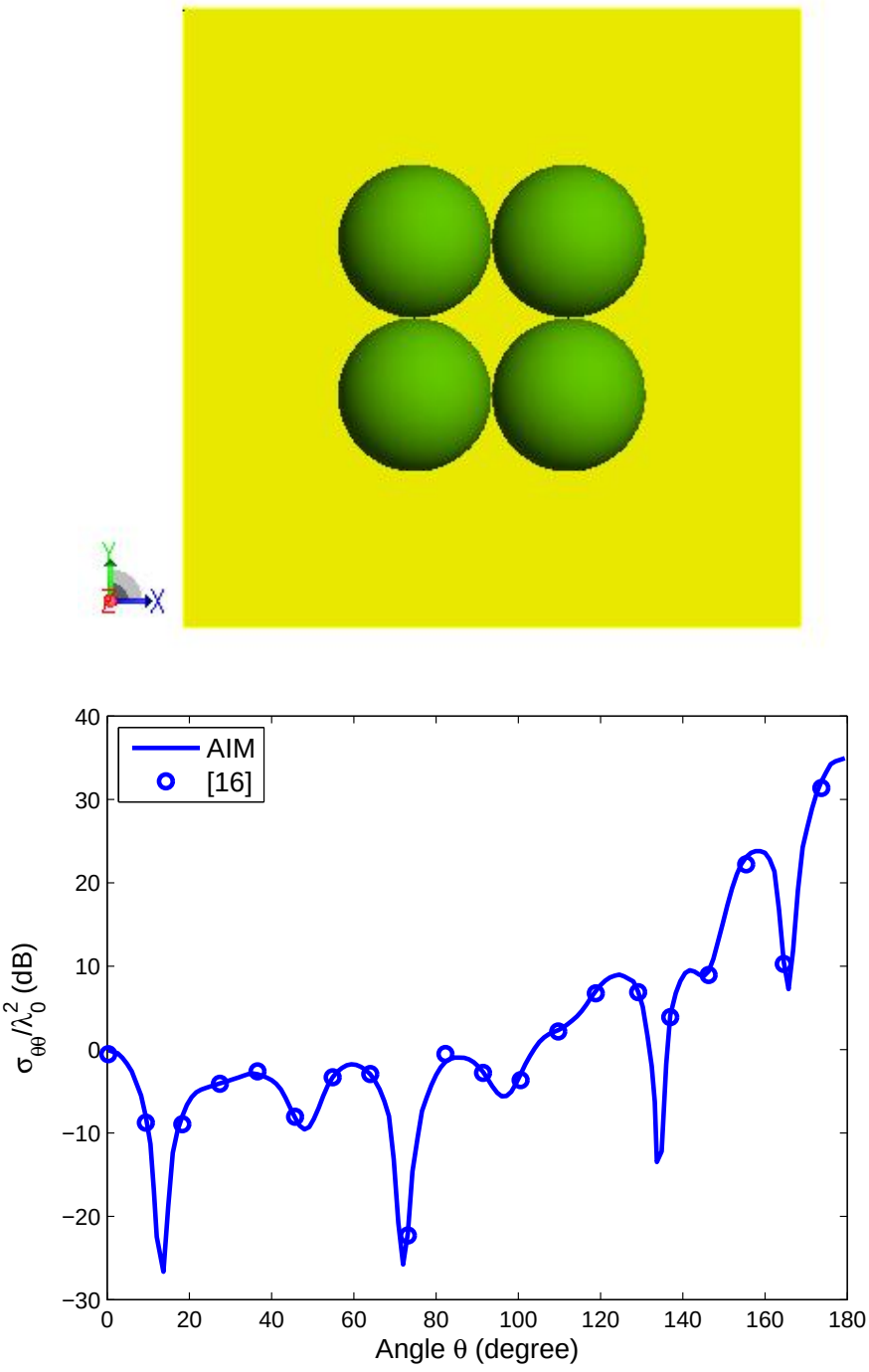

Figure 3.8: (a) Configuration of four spheres with $\epsilon_r = 1.6 - 0.4j$ and $\xi_r = 0$, $1.3\lambda_0$ above a $8\lambda_0 \times 8\lambda_0$ PEC plate. The diameter of each sphere is $2\lambda_0$. (b) Bistatic RCS of the structure in x-z plane.

Chapter 4

Scattering by Large Conducting and Bi-Anisotropic Objects

The most generalized composite media is bi-anisotropic media, which is characterized by four constitutive parameter tensors. We do not have closed form Green's functions yet for it, thus we can only solve the scattering problems involving bi-anisotropic media using VIEs which replace the inhomogeneity using equivalent volume current sources, by which only free space Green's function is needed. In this chapter, the scattering problem of bi-anistoropic and conducting objects will be solved by using the VSIE method. In the first section, constitutive parameters for general bi-anisotropic media are introduced. In the second section, VSIE for scattering by bi-anisotropic and conducting objects will be derived which will be discretized in the following section. In the third section, MoM will be applied to convert the integral equations into matrix forms; and in the fourth section, the AIM algorithm will be modified to accelerate the solution process and reduce memory requirement. In the last section, numerical

examples will be presented to demonstrate the accuracy and capabilities in solving large bi-anisotropic and conducting objects.

4.1 Volume Integral Equations

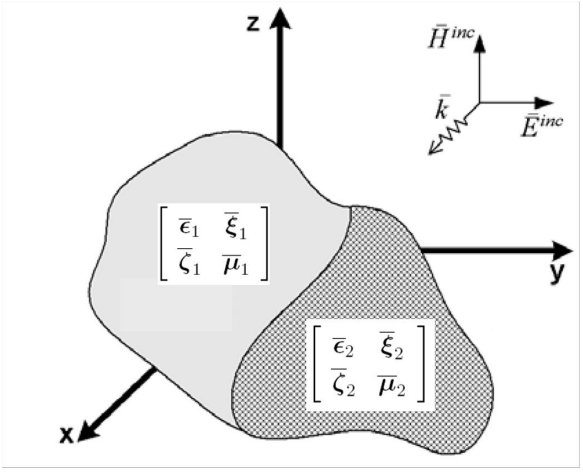

Figure 4.1: Inhomogeneous bi-anisotropic scatterers in free space illuminated by an electromagnetic wave.

Consider a homogeneous background medium with permittivity ϵ_0 and permeability μ_0. If an inhomogeneous bi-anisotropic body is present in the background, the fields in the region of bi-anisotropic body must satisfy Maxwell equation:

$$\nabla \times \boldsymbol{E} = -j\omega \boldsymbol{B} = -j\omega\mu_0 \boldsymbol{H} - \boldsymbol{M}_V \tag{4.1}$$

$$\nabla \times \boldsymbol{H} = j\omega \boldsymbol{D} = j\omega\epsilon_0 \boldsymbol{E} + \boldsymbol{J}_V \tag{4.2}$$

The constitutive relations for bi-anisotropic media are:

$$\boldsymbol{D} = \overline{\boldsymbol{\epsilon}} \cdot \boldsymbol{E} + \overline{\boldsymbol{\xi}} \cdot \boldsymbol{H} \tag{4.3}$$

$$\boldsymbol{B} = \overline{\boldsymbol{\zeta}} \cdot \boldsymbol{E} + \overline{\boldsymbol{\mu}} \cdot \boldsymbol{H} \tag{4.4}$$

which can be written as:

$$\boldsymbol{E} = \overline{\boldsymbol{\alpha}}_1 \cdot \boldsymbol{D} + \overline{\boldsymbol{\alpha}}_2 \cdot \boldsymbol{B} \tag{4.5}$$

$$\boldsymbol{H} = \overline{\boldsymbol{\alpha}}_3 \cdot \boldsymbol{D} + \overline{\boldsymbol{\alpha}}_4 \cdot \boldsymbol{B} \tag{4.6}$$

where the parameters are:

$$\begin{pmatrix} \overline{\boldsymbol{\alpha}}_1 & \overline{\boldsymbol{\alpha}}_2 \\ \overline{\boldsymbol{\alpha}}_3 & \overline{\boldsymbol{\alpha}}_4 \end{pmatrix} = \begin{pmatrix} \overline{\boldsymbol{\epsilon}} & \overline{\boldsymbol{\xi}} \\ \overline{\boldsymbol{\zeta}} & \overline{\boldsymbol{\mu}} \end{pmatrix}^{-1} \tag{4.7}$$

The expression of equivalent volume sources are:

$$\boldsymbol{J}_V = j\omega(\overline{\boldsymbol{\epsilon}} - \epsilon_0 \overline{\boldsymbol{I}}) \cdot \boldsymbol{E} + j\omega \overline{\boldsymbol{\xi}} \cdot \boldsymbol{H} \tag{4.8}$$

$$\boldsymbol{M}_V = j\omega(\overline{\boldsymbol{\mu}} - \mu_0 \overline{\boldsymbol{I}}) \cdot \boldsymbol{H} + j\omega \overline{\boldsymbol{\zeta}} \cdot \boldsymbol{E} \tag{4.9}$$

which can be written as:

$$\boldsymbol{J}_V = j\omega(\overline{\boldsymbol{\beta}}_1 \cdot \boldsymbol{D} + \overline{\boldsymbol{\beta}}_2 \cdot \boldsymbol{B}) \tag{4.10}$$

$$\boldsymbol{M}_V = j\omega(\overline{\boldsymbol{\beta}}_3 \cdot \boldsymbol{D} + \overline{\boldsymbol{\beta}}_4 \cdot \boldsymbol{B}) \tag{4.11}$$

where the parameters are defined as:

$$\begin{pmatrix} \overline{\boldsymbol{\beta}}_1 & \overline{\boldsymbol{\beta}}_2 \\ \overline{\boldsymbol{\beta}}_3 & \overline{\boldsymbol{\beta}}_4 \end{pmatrix} = \begin{pmatrix} \overline{\boldsymbol{I}} - \epsilon_0 \overline{\boldsymbol{\alpha}}_1 & -\epsilon_0 \overline{\boldsymbol{\alpha}}_2 \\ -\mu_0 \overline{\boldsymbol{\alpha}}_3 & \overline{\boldsymbol{I}} - \mu_0 \overline{\boldsymbol{\alpha}}_4 \end{pmatrix} \tag{4.12}$$

Using mixed potential expression for source field relationship, the scattering fields can be expressed by:

$$\boldsymbol{E}^{\text{sca}} = -j\omega \boldsymbol{A} - \nabla \phi_e - \nabla \times \frac{\boldsymbol{F}}{\epsilon_0} \tag{4.13}$$

$$\boldsymbol{H}^{\text{sca}} = -j\omega \boldsymbol{F} - \nabla \phi_m + \nabla \times \frac{\boldsymbol{A}}{\mu_0} \tag{4.14}$$

where $\boldsymbol{A}, \boldsymbol{F}, \phi_e, \phi_m$ are magnetic vector potential, electric vector potential, electric scalar potential, magnetic scalar potential which can be expressed by:

$$\boldsymbol{A} = \mu_0 \int_V \boldsymbol{J}_V G dV' \tag{4.15}$$

$$\boldsymbol{F} = \epsilon_0 \int_V \boldsymbol{M}_V G dV' \tag{4.16}$$

$$\phi_e = \frac{1}{\epsilon_0} \int_V \rho_e G dV' \tag{4.17}$$

$$\phi_m = \frac{1}{\mu_0} \int_V \rho_m G dV' \tag{4.18}$$

where G is the free space Green's function:

$$G(\boldsymbol{r}, \boldsymbol{r}') = \frac{e^{-jk_0|\boldsymbol{r}-\boldsymbol{r}'|}}{4\pi|\boldsymbol{r}-\boldsymbol{r}'|} \tag{4.19}$$

The relations between equivalent volume charge densities and currents are:

$$\rho_e = -\frac{1}{j\omega} \nabla \cdot \boldsymbol{J}_V \tag{4.20}$$

$$\rho_m = -\frac{1}{j\omega} \nabla \cdot \boldsymbol{M}_V \tag{4.21}$$

Since the total fields are the sum of incident fields and scattering fields induced by the bi-anisotropic body:

$$\boldsymbol{E} = \boldsymbol{E}^{\text{inc}} + \boldsymbol{E}^{\text{sca}} \tag{4.22}$$

$$\boldsymbol{H} = \boldsymbol{H}^{\text{inc}} + \boldsymbol{H}^{\text{sca}} \tag{4.23}$$

based on eqns.(4.5)-(4.6) and eqns.(4.13)-(4.14), we obtain volume electric and magnetic integral equations:

$$\boldsymbol{E}^{\text{inc}} = \overline{\boldsymbol{\alpha}}_1 \cdot \boldsymbol{D} + \overline{\boldsymbol{\alpha}}_2 \cdot \boldsymbol{B} + j\omega \boldsymbol{A} + \nabla \phi_e + \nabla \times \frac{\boldsymbol{F}}{\epsilon_0} \tag{4.24}$$

$$\boldsymbol{H}^{\text{inc}} = \overline{\boldsymbol{\alpha}}_3 \cdot \boldsymbol{D} + \overline{\boldsymbol{\alpha}}_4 \cdot \boldsymbol{B} + j\omega \boldsymbol{F} + \nabla \phi_m - \nabla \times \frac{\boldsymbol{A}}{\mu_0} \tag{4.25}$$

When there are conducting objects besides the bi-anisotropic objects, we should also consider the scattered fields by the conducting objects. In this way, we can use VSIE to solve the problem. The scattered electric field $\boldsymbol{E}^{\text{sca}}$ and magnetic field $\boldsymbol{H}^{\text{sca}}$ by the induced surface electric current of the conducting object are given by

$$\boldsymbol{E}_S^{\text{sca}} = -j\omega \boldsymbol{A}_S - \nabla V_S \tag{4.26}$$

$$\boldsymbol{H}_S^{\text{sca}} = \frac{1}{\mu_0} \nabla \times \boldsymbol{A}_S \tag{4.27}$$

where $\boldsymbol{A}_S$ and V_S can be expressed as

$$\boldsymbol{A}_S = \mu_0 \int_S \boldsymbol{J}_S G dS \tag{4.28}$$

$$V_S = \frac{1}{\epsilon_0} \int_S \rho_S G dS \tag{4.29}$$

with

$$\rho_S = -\frac{1}{j\omega} \nabla'_S \cdot \boldsymbol{J}_S. \tag{4.30}$$

In the bi-anisotropic region V, by taking the scattered field from the surface current into consideration, the total electric field becomes

$$\boldsymbol{E} = \boldsymbol{E}^{\text{inc}} + \boldsymbol{E}_V^{\text{sca}} + \boldsymbol{E}_S^{\text{sca}}. \tag{4.31}$$

Similarly, the scattered field by volume current density also contributes to the total field on conducting surface S. Since the tangential components of total electric field vanish on conducting surface, we obtain the EFIE as follows:

$$\widehat{\boldsymbol{n}} \times \boldsymbol{E}^{\text{inc}} = -\widehat{\boldsymbol{n}} \times [\boldsymbol{E}_V^{\text{sca}} + \boldsymbol{E}_S^{\text{sca}}]. \tag{4.32}$$

For a closed conducting surface, the MFIE can be obtained by considering the tangential components of the total magnetic field on the conducting surface, which are equal to the induced surface current components. Thus,

we get

$$\widehat{\boldsymbol{n}} \times \boldsymbol{H}^{\text{inc}} = \boldsymbol{J}_S - \widehat{\boldsymbol{n}} \times [\boldsymbol{H}_V^{\text{sca}} + \boldsymbol{H}_S^{\text{sca}}]. \tag{4.33}$$

In order to avoid internal resonance and make the impedance matrix well conditioned, the CFIE can be formulated for a closed conducting body by linearly combining the EFIE and the MFIE such that

$$\begin{aligned} &\widehat{\boldsymbol{n}} \times (\alpha \boldsymbol{E}^{\text{inc}} + (1-\alpha)\eta_0 \boldsymbol{H}^{\text{inc}}) = (1-\alpha)\eta_0 \boldsymbol{J}_S \\ &-\widehat{\boldsymbol{n}} \times [\alpha(\boldsymbol{E}_V^{\text{sca}} + \boldsymbol{E}_S^{\text{sca}}) + (1-\alpha)\eta_0(\boldsymbol{H}_V^{\text{sca}} + \boldsymbol{H}_S^{\text{sca}})]. \end{aligned} \tag{4.34}$$

where $0 \leq \alpha \leq 1$, and $\eta_0 = \sqrt{\frac{\mu_0}{\epsilon_0}}$ is the free space impedance.

4.2 Method of Moments for Bi-Anisotropic Media

The integral equations characterizing the interaction of electromagnetic waves and composite of bi-anisotropic and PEC objects are summarized as follows:

$$\overline{\boldsymbol{\alpha}}_1 \boldsymbol{D} + \overline{\boldsymbol{\alpha}}_2 \boldsymbol{B} + j\omega \boldsymbol{A} + \nabla V + \frac{1}{\epsilon_0} \nabla \times \boldsymbol{F} = \boldsymbol{E}^{\text{inc}} \tag{4.35}$$

$$\overline{\boldsymbol{\alpha}}_3 \boldsymbol{D} + \overline{\boldsymbol{\alpha}}_4 \boldsymbol{B} + j\omega \boldsymbol{F} + \nabla U - \frac{1}{\mu_0} \nabla \times \boldsymbol{A} = \boldsymbol{H}^{\text{inc}} \tag{4.36}$$

$$\begin{aligned} &\widehat{\boldsymbol{n}} \times (\alpha \boldsymbol{E}^{\text{inc}} + (1-\alpha)\eta_0 \boldsymbol{H}^{\text{inc}}) = (1-\alpha)\eta_0 \boldsymbol{J}_S \\ &-\widehat{\boldsymbol{n}} \times [\alpha(\boldsymbol{E}_V^{\text{sca}} + \boldsymbol{E}_S^{\text{sca}}) + (1-\alpha)\eta_0(\boldsymbol{H}_V^{\text{sca}} + \boldsymbol{H}_S^{\text{sca}})]. \end{aligned} \tag{4.37}$$

The volume of bi-anisotropic material and the surface of conducting body are discretized into tetrahedral elements and triangular patches, respectively. These elements are used because of their flexibility to model arbitrarily shaped 3-D object. The surface current density is expanded using

the RWG basis functions $\boldsymbol{f}_n^S$:

$$\boldsymbol{J}_S = \sum_{n=1}^{N_S} I_n^S \boldsymbol{f}_n^S. \tag{4.38}$$

Within the bi-anisotropic region, to ensure the normal continuity of $\boldsymbol{D}$ and $\boldsymbol{B}$, the electric and magnetic flux density $\boldsymbol{D}$ and $\boldsymbol{B}$ are expanded using the SWG basis functions $\boldsymbol{f}_n^V$ as follows:

$$\boldsymbol{D} = \frac{1}{j\omega} \sum_{n=1}^{N_V} D_n \boldsymbol{f}_n^V \tag{4.39}$$

$$\boldsymbol{B} = \frac{1}{j\omega} \sum_{n=1}^{N_V} B_n \boldsymbol{f}_n^V. \tag{4.40}$$

Using the Galerkin's procedure, testing Eqns. (4.35)-(4.36) with $\boldsymbol{f}_m^V$ and testing Eqn. (4.37) with $\boldsymbol{f}_m^S$, the hybrid integral equations will be converted into a matrix equation system as

$$\begin{pmatrix} Z_{mn}^{ED} & Z_{mn}^{EB} & Z_{mn}^{EI} \\ Z_{mn}^{HD} & Z_{mn}^{HB} & Z_{mn}^{HI} \\ Z_{mn}^{SD} & Z_{mn}^{SB} & Z_{mn}^{SI} \end{pmatrix} \begin{pmatrix} D_n \\ B_n \\ I_n^S \end{pmatrix} = \begin{pmatrix} E_m^V \\ H_m^V \\ E_m^S \end{pmatrix} \tag{4.41}$$

where

$$\begin{aligned} Z_{mn}^{ED} = & \frac{1}{j\omega} \langle \boldsymbol{f}_m^V, \overline{\boldsymbol{\alpha}}_1 \cdot \boldsymbol{f}_n^V \rangle + j\omega\mu_0 \langle \boldsymbol{f}_m^V, \boldsymbol{A}_{1,n} \rangle \\ & - \frac{1}{j\omega\epsilon_0} \langle \boldsymbol{f}_m^V, \nabla\phi_{1,n} \rangle + \langle \boldsymbol{f}_m^V, \nabla \times \boldsymbol{A}_{3,n} \rangle \end{aligned} \tag{4.42}$$

$$\begin{aligned} Z_{mn}^{EB} = & \frac{1}{j\omega} \langle \boldsymbol{f}_m^V, \overline{\boldsymbol{\alpha}}_2 \cdot \boldsymbol{f}_n^V \rangle + j\omega\mu_0 \langle \boldsymbol{f}_m^V, \boldsymbol{A}_{2,n} \rangle \\ & - \frac{1}{j\omega\epsilon_0} \langle \boldsymbol{f}_m^V, \nabla\phi_{2,n} \rangle + \langle \boldsymbol{f}_m^V, \nabla \times \boldsymbol{A}_{4,n} \rangle \end{aligned} \tag{4.43}$$

$$Z_{mn}^{EI} = j\omega\mu_0 \langle \boldsymbol{f}_m^V, \boldsymbol{A}_n^S \rangle - \frac{1}{j\omega\epsilon_0} \langle \boldsymbol{f}_m^V, \nabla\phi_n^S \rangle \tag{4.44}$$

$$\begin{aligned} Z_{mn}^{HD} = & \frac{1}{j\omega} \langle \boldsymbol{f}_m^V, \overline{\boldsymbol{\alpha}}_3 \cdot \boldsymbol{f}_n^V \rangle + j\omega\epsilon_0 \langle \boldsymbol{f}_m^V, \boldsymbol{A}_{3,n} \rangle \\ & - \frac{1}{j\omega\mu_0} \langle \boldsymbol{f}_m^V, \nabla\phi_{3,n} \rangle - \langle \boldsymbol{f}_m^V, \nabla \times \boldsymbol{A}_{1,n} \rangle \end{aligned} \tag{4.45}$$

$$Z_{mn}^{HB} = \frac{1}{j\omega}\langle \boldsymbol{f}_m^V, \overline{\boldsymbol{\alpha}}_4 \cdot \boldsymbol{f}_n^V \rangle + j\omega\epsilon_0 \langle \boldsymbol{f}_m^V, \boldsymbol{A}_{4,n} \rangle$$
$$- \frac{1}{j\omega\mu_0}\langle \boldsymbol{f}_m^V, \nabla\phi_{4,n} \rangle - \langle \boldsymbol{f}_m^V, \nabla \times \boldsymbol{A}_{2,n} \rangle \tag{4.46}$$

$$Z_{mn}^{HI} = -\langle \boldsymbol{f}_m^V, \nabla \times \boldsymbol{A}_n^S \rangle \tag{4.47}$$

$$Z_{mn}^{SD} = (1-\alpha)\eta_0 \widehat{\boldsymbol{n}} \times \left\{ j\omega\epsilon_0 \langle \boldsymbol{f}_m^S, \boldsymbol{A}_{3,n} \rangle - \frac{1}{j\omega\mu_0}\langle \boldsymbol{f}_m^S, \nabla\phi_{3,n} \rangle - \langle \boldsymbol{f}_m^S, \nabla \times \boldsymbol{A}_{1,n} \rangle \right\}$$
$$+ \alpha \left\{ j\omega\mu_0 \langle \boldsymbol{f}_m^S, \boldsymbol{A}_{1,n} \rangle - \frac{1}{j\omega\epsilon_0}\langle \boldsymbol{f}_m^S, \nabla\phi_{1,n} \rangle + \langle \boldsymbol{f}_m^S, \nabla \times \boldsymbol{A}_{3,n} \rangle \right\} \tag{4.48}$$

$$Z_{mn}^{SB} = (1-\alpha)\eta_0 \widehat{\boldsymbol{n}} \times \left\{ j\omega\epsilon_0 \langle \boldsymbol{f}_m^S, \boldsymbol{A}_{4,n} \rangle - \frac{1}{j\omega\mu_0}\langle \boldsymbol{f}_m^S, \nabla\phi_{4,n} \rangle - \langle \boldsymbol{f}_m^S, \nabla \times \boldsymbol{A}_{2,n} \rangle \right\}$$
$$+ \alpha \left\{ j\omega\mu_0 \langle \boldsymbol{f}_m^S, \boldsymbol{A}_{2,n} \rangle - \frac{1}{j\omega\epsilon_0}\langle \boldsymbol{f}_m^S, \nabla\phi_{2,n} \rangle + \langle \boldsymbol{f}_m^S, \nabla \times \boldsymbol{A}_{4,n} \rangle \right\} \tag{4.49}$$

$$Z_{mn}^{SI} = (1-\alpha)\eta_0 \langle \boldsymbol{f}_m^S, \boldsymbol{f}_n^S \rangle + \alpha \left\{ j\omega\mu_0 \langle \boldsymbol{f}_m^S, \boldsymbol{A}_n^S \rangle - \frac{1}{j\omega\epsilon_0}\langle \boldsymbol{f}_m^S, \nabla\phi_n^S \rangle \right\}$$
$$- (1-\alpha)\eta_0 \widehat{\boldsymbol{n}} \times \left\{ \langle \boldsymbol{f}_m^S, \nabla \times \boldsymbol{A}_n^S \rangle \right\} \tag{4.50}$$

and the elements of the right hand side are:

$$E_m^V = \langle \boldsymbol{f}_m^V, \boldsymbol{E}^{\text{inc}} \rangle \tag{4.51}$$

$$H_m^V = \langle \boldsymbol{f}_m^V, \boldsymbol{H}^{\text{inc}} \rangle \tag{4.52}$$

$$E_m^S = \alpha \langle \boldsymbol{f}_m^S, \boldsymbol{E}^{\text{inc}} \rangle + (1-\alpha)\eta_0 \widehat{\boldsymbol{n}} \times \langle \boldsymbol{f}_m^S, \boldsymbol{H}^{\text{inc}} \rangle \tag{4.53}$$

where the symmetric product of two functions $\boldsymbol{f}$ and $\boldsymbol{g}$ is defined as

$$\langle \boldsymbol{f}, \boldsymbol{g} \rangle = \int_\Omega \boldsymbol{f} \cdot \boldsymbol{g} d\Omega \tag{4.54}$$

and

$$\boldsymbol{A}_{i,n} = \int_{V_n} \overline{\boldsymbol{\beta}}_i \cdot \boldsymbol{f}_n^V G dV' \tag{4.55}$$

$$\phi_{i,n} = \int_{V_n} \nabla \cdot (\overline{\boldsymbol{\beta}}_i \cdot \boldsymbol{f}_n^V) G dV' \tag{4.56}$$

$$\boldsymbol{A}_n^S = \int_{S_n} \boldsymbol{f}_n^S G dS' \tag{4.57}$$

$$\phi_n^S = \int_{S_n} \nabla \cdot (\boldsymbol{f}_n^S) G dS'. \tag{4.58}$$

4.3 Accuracy and Complexity of the AIM Bi-Anisotropic Solver

This section discusses about the accuracy and complexity of the chiral AIM solver. First, we discuss about the accuracy. We set up a numerical experiment to test how well the approximation of AIM to MoM is in the far zone distance and how far we should choose as the far zone distance. In this experiment, we consider a conducting sphere with radius $2.0\lambda_0$ coated with bi-anisotropic media, the thickness of the coating is 0.1λ with the constitutive parameters $\epsilon_r = 2$, $\mu_r = 1.5$, and $\xi_r = 0.3$ where $\overline{\boldsymbol{\epsilon}} = \epsilon_r\epsilon_0\overline{\boldsymbol{I}}$, $\overline{\boldsymbol{\mu}} = \mu_r\mu_0\overline{\boldsymbol{I}}$, $\overline{\boldsymbol{\xi}} = -j\xi_r\sqrt{\epsilon_r\epsilon_0\mu_r\mu_0}\overline{\boldsymbol{I}}$ and $\overline{\boldsymbol{\zeta}} = -\overline{\boldsymbol{\xi}}$. The SWG and RWG basis functions are used to expand the volume currents and surface currents to discretize the integral equations. Then, we define the relative error as

$$\Delta Z_{mn} = \frac{|Z_{mn} - \hat{Z}_{mn}|}{|Z_{mn}|}. \tag{4.59}$$

where Z_{mn} is the impedance matrix element calculated by MoM and $\hat{Z}_{mn}$ is the impedance matrix element calculated by AIM. we take Z_{mn}^{ED} as an example. Similar calculations can be also carried out for other impedance matrix elements. The ΔZ_{mn} is plotted as a function of the distance between elements for different grid sizes, as shown in Fig. 4.2. From Fig. 4.2, it is clear that $\hat{Z}_{mn}$ approximates Z_{mn} very well at far zone distance, e.g., $0.4\lambda_0$. The results also show that the smaller the grid size, the more accurate the approximation is. Since reducing grid size could increase the FFT vector size, we have to choose an appropriate grid size as a compromise to balance the required accuracy and the given computer resources. Throughout this paper, we choose a grid size of $0.1\lambda_0$ since the accuracy of 1% relative error is good enough for most engineering applications.

Next, we explore the computational complexity and storage require-

ment of our AIM implementation. The matrix storage requirement and CPU time per iteration are plotted in Fig. 4.3. From it, it is clear that AIM solver has a very small requirement on memory as well as computational time, since the ordinary MoM solver requires $O(N^2)$ for memory and $O(N^3)$ for computational time.

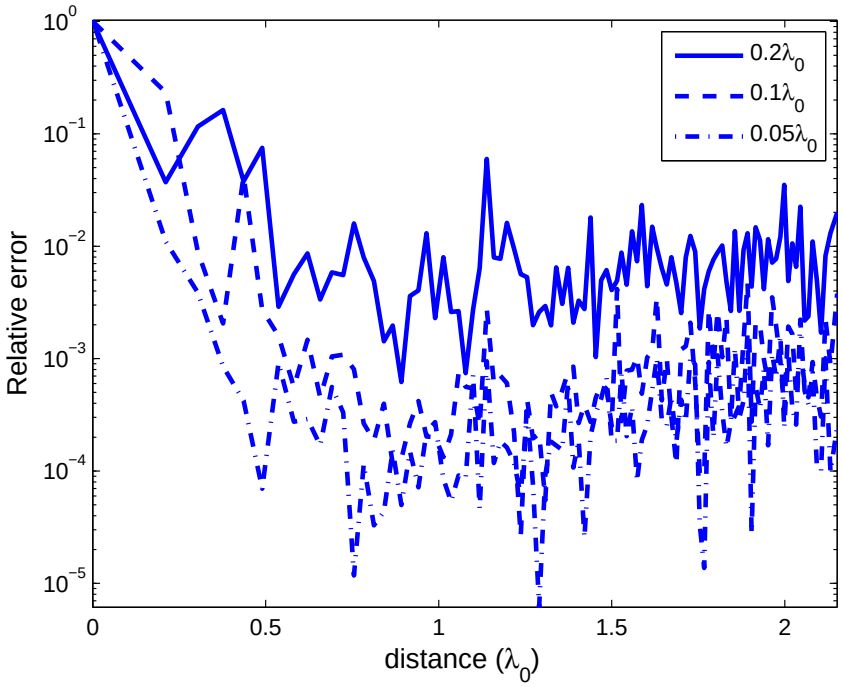

Figure 4.2: The relative error of AIM for matrix elements of Z_{mn}^{ED} using different grid sizes.

4.4 Numerical Results Involving Large Bi-Anisotropic Objects

In this section, several examples will be given to demonstrate the validity and efficiency of our code to solve the electromagnetic scattering by large scale arbitrarily shaped bi-anisotropic objects. The GMRES solver is adopted as the iterative solver and it terminates when the normalized residue falls below 10^{-3}. By default, the objects are illuminated by a plane

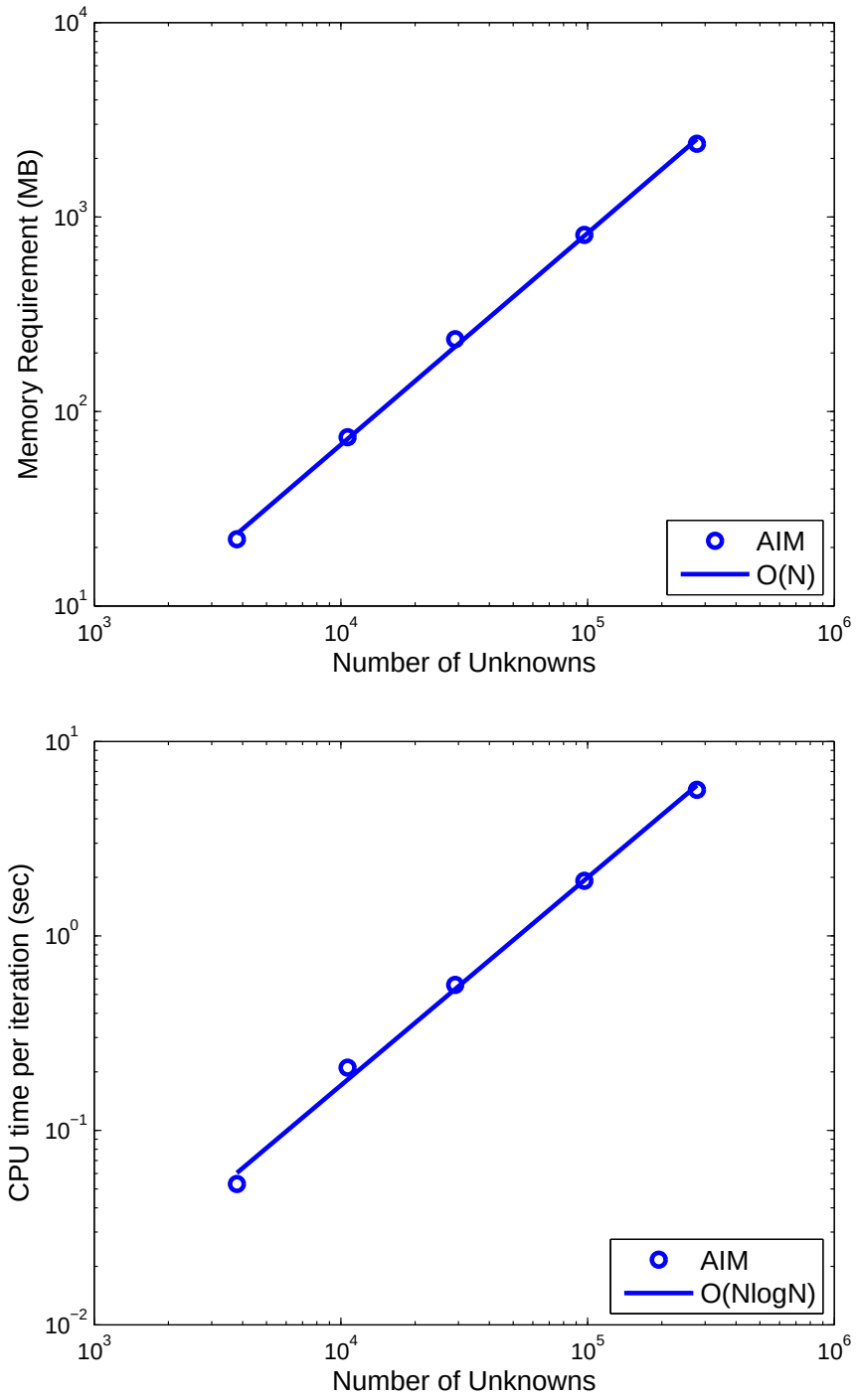

Figure 4.3: The number of unknowns versus (a) memory requirement and CPU time per iteration for the AIM solver.

wave with $\hat{k}$ in +z-direction and $\boldsymbol{E}$ in +x-direction. λ_0 denotes the free space wavelength.

4.4.1 Large Dielectric Objects

In this section, the first example we considered is a conducting sphere coated with dielectric material. The diameter of the spherical core is $4.0\lambda_0$ and the thickness of the coating layer is $0.1\lambda_0$, with a relative permittivity of $\epsilon_r = 2.0 - 1.0j$. The bistatic RCS in x-z plane is computed with 249,093 unknowns and the result is shown in Fig. 4.4. The RCS result is compared with the Mie series solution and a good agreement was observed.

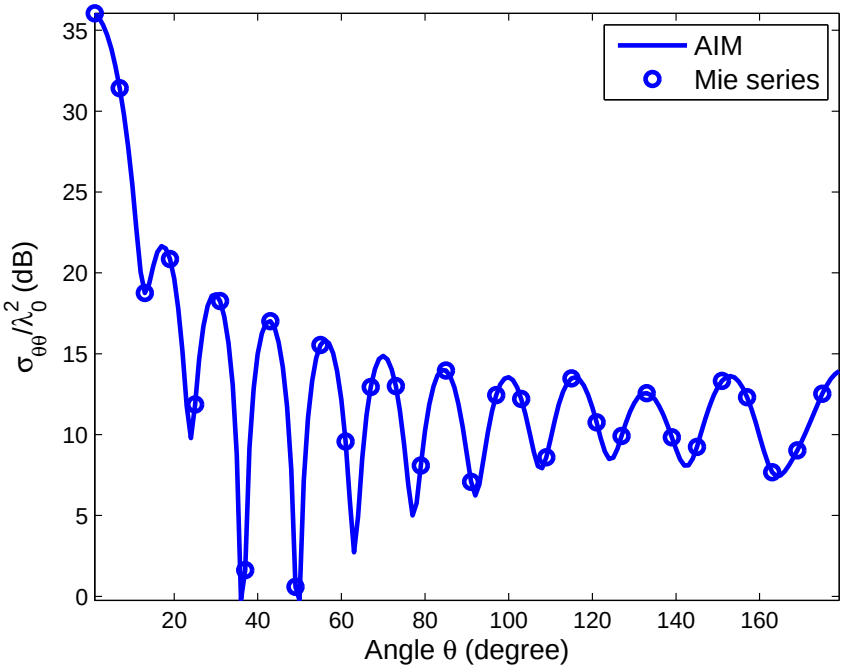

Figure 4.4: Bistatic RCS in x-z plane of a conducting sphere with diameter $4.0\lambda_0$ coated with dielectric material with a thickness of $0.1\lambda_0$, and a relative permittivity $\epsilon_r = 2.0 - 1.0j$.

The second example we considered is a conducting trapezoidal plate with coating on its sides as shown in Fig. 4.5. The length of the upper side is 3 feet and 7 feet for the lower side. The height is 3 feet. The thickness of

the plate is 1 inches. The thickness of the coating is 2 inches. The coating layer has relative permittivity of $\epsilon_r = 4.5 - 9.0j$. The monostatic RCSs for $\theta\theta$- and $\phi\phi$-polarizations in the x-y and x-z planes are computed at 1 GHz with 254,957 unknowns. The corresponding results are shown in Fig. 4.6 and Fig. 4.7. A good agreement with published results [101, 102] is observed.

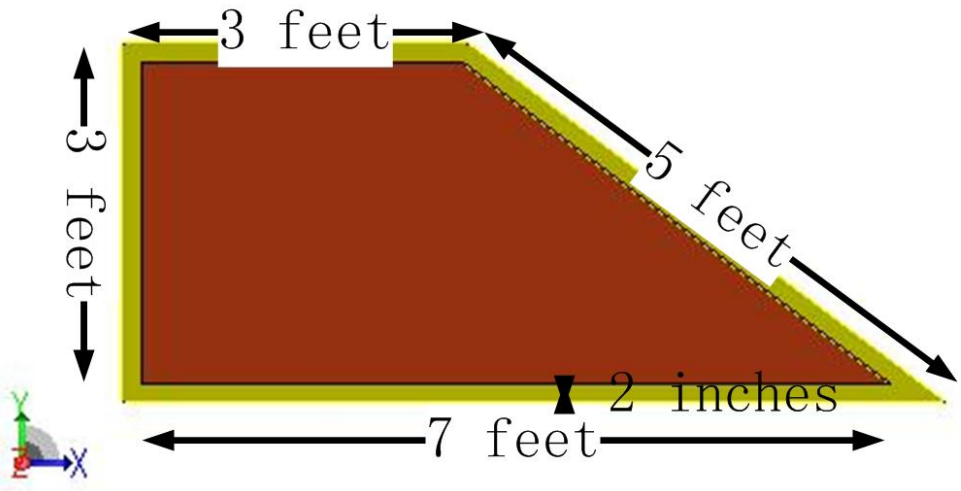

Figure 4.5: The geometry of a trapezoidal plate (in blown) with coating (in yellow) on its sides. The coating material has a relative permittivity, $\epsilon_r = 4.5 - 9.0j$.

4.4.2 Large Magnetodielectric Objects

In this section, the first example we considered is a conducting sphere coated with magnetodielectric material. The diameter of the spherical core is $4.0\lambda_0$ and the thickness of the coating layer is $0.1\lambda_0$, with a relative permittivity of $\epsilon_r = 1.6 - 0.8j$, permeability of $\mu_r = 0.8 - 0.2j$. The bistatic RCS in x-z plane is computed with 225,703 unknowns and the result is shown in Fig. 4.8. The RCS result is compared with the Mie series solution and a good agreement is observed.

The second example is a multilayer cylinder coated with a dielectric

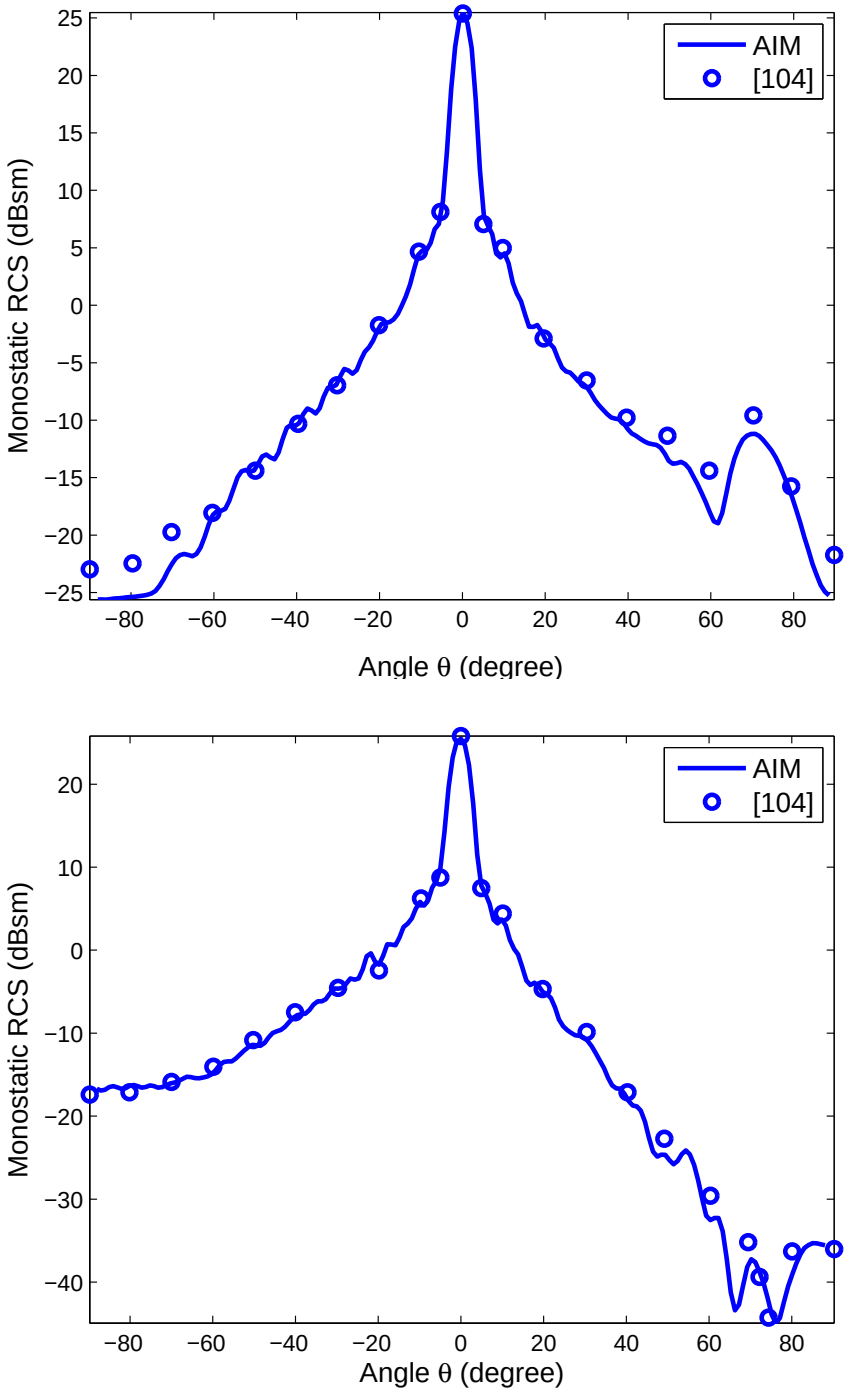

Figure 4.6: Monostatic RCSs of a trapezoidal conducting plate with coated sides shown in Fig. 4.5 at 1 GHz. (a) $\theta\theta$-polarization in x-z plane. (b) $\phi\phi$-polarization in x-z plane.

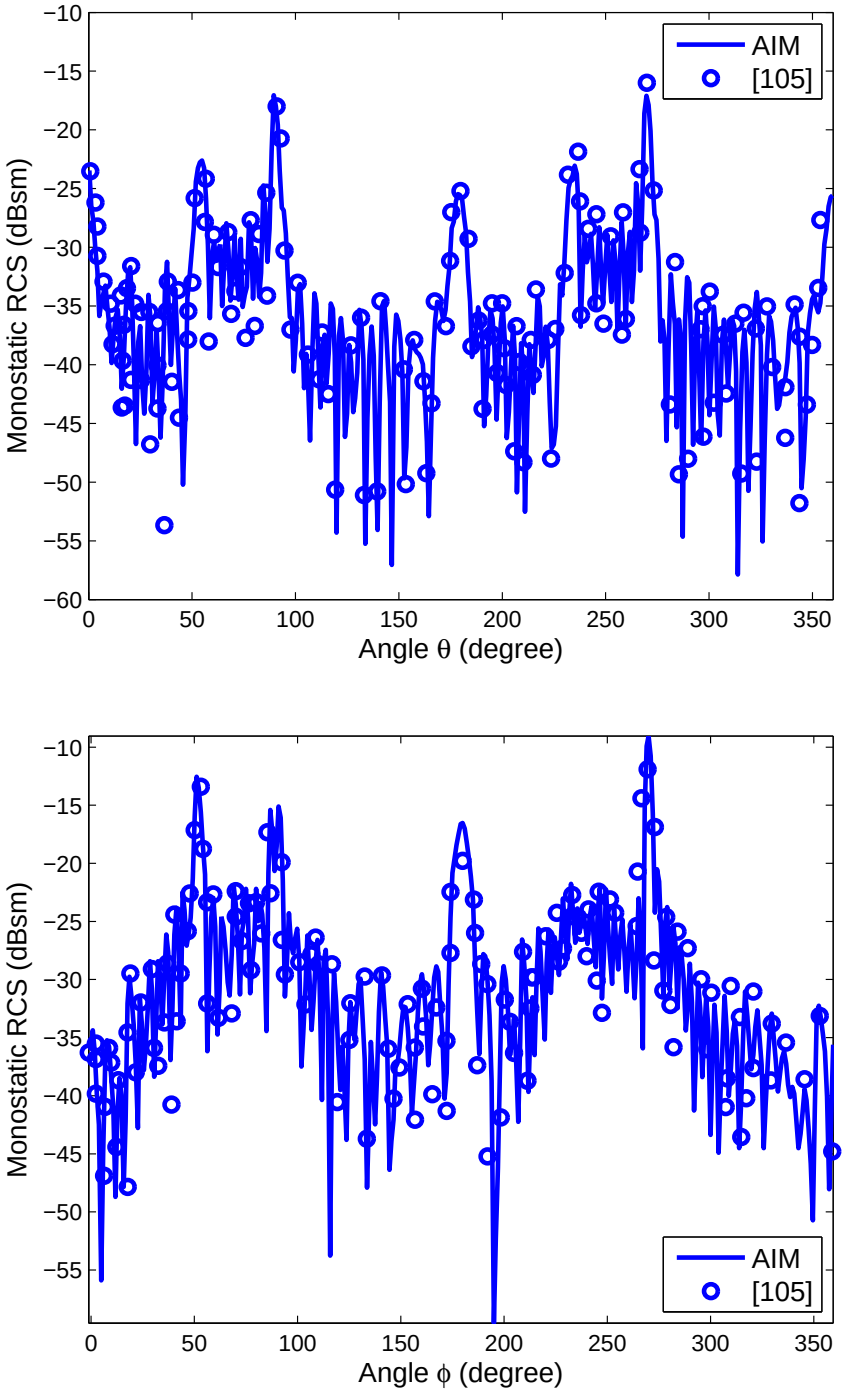

Figure 4.7: Monostatic RCSs of a trapezoidal conducting plate with coated sides shown in Fig. 4.5 at 1 GHz. (a) $\theta\theta$-polarization in x-y plane. (b) $\phi\phi$-polarization in x-y plane.

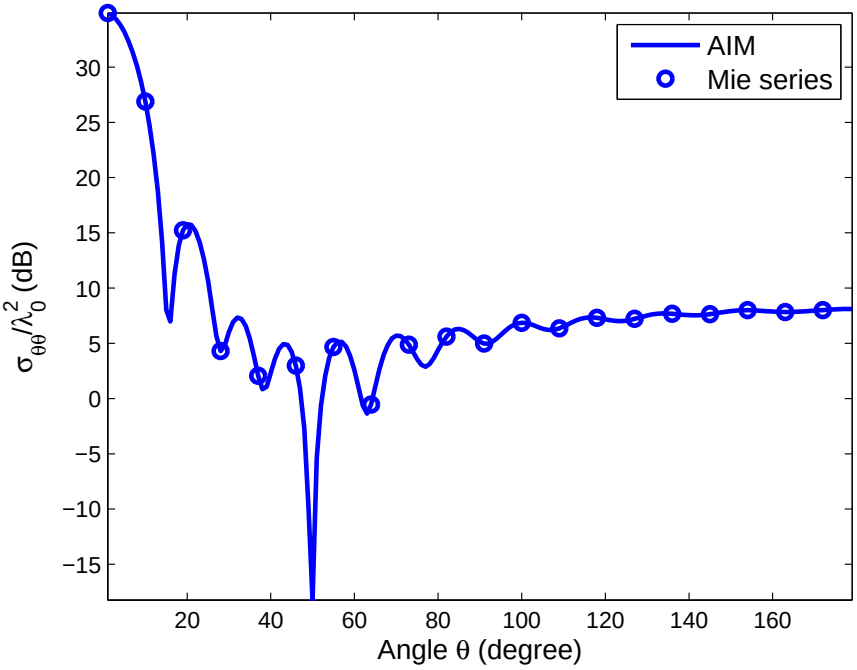

Figure 4.8: Bistatic RCS of a conducting sphere with diameter $4.0\lambda_0$ coated with magnetodielectric material with the thickness of the coating layer $0.1\lambda_0$, $\epsilon_r = 1.6 - 0.8j$, $\mu_r = 0.8 - 0.2j$ in x-z plane.

material and the cross-section of the cylinder is shown in Fig. 4.9(a). The diameter of the inner layer is $0.4\lambda_0$ and thickness of the other three layers is $0.2\lambda_0$ each. The inner layer of the cylinder is made of lossy magnetic material with relative permeability $\mu_{r1} = 1.69 - 0.01j$ and the outer layer is made of lossy dielectric with relative permittivity $\epsilon_{r1} = 1.69 - 0.01j$. The second and third layers of the cylinder are made of magnetodielectric material with material properties $\epsilon_{r2} = 1.21$, $\mu_{r2} = 1.44$ and $\epsilon_{r3} = 1.44$, $\mu_{r3} = 1.21$, respectively. The height of the cylinder is $2.0\lambda_0$. The cylinder is coated with a dielectric layer having a thickness of $0.1\lambda_0$ and a relative permittivity of $\epsilon_{r5} = 1.69$. The bistatic RCS of the cylinder in x-z plane is computed using 295,913 unknowns and shown in Fig. 4.9(b). Also shown is the result from [23]. A good agreement is observed.

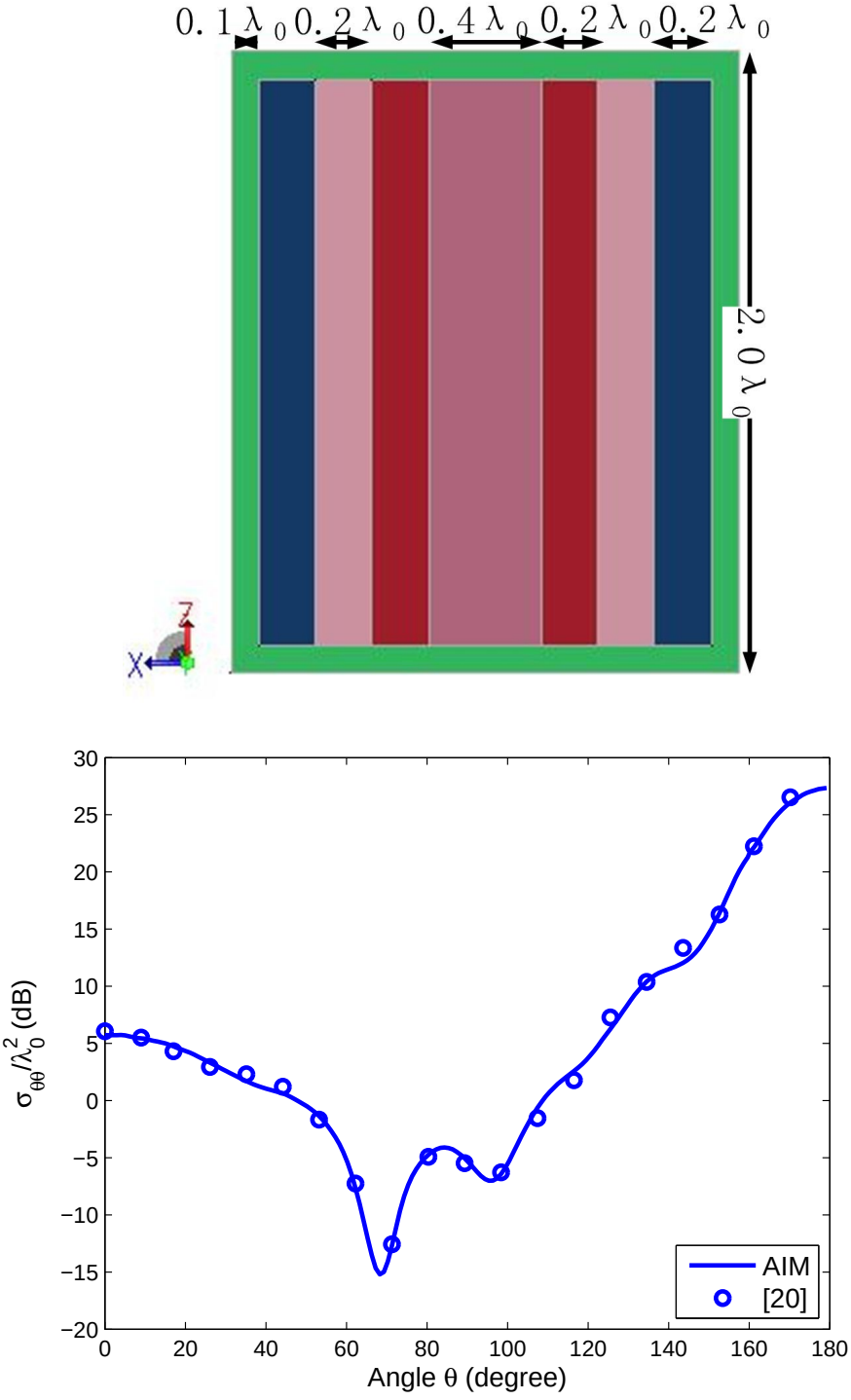

Figure 4.9: (a) The cross section of a multilayered cylinder made of magnetodielectric material with a layer of dielectric coating; (b) Bistatic RCS of the cylinder shown in Fig. 4.9(a) in x-z plane.

4.4.3 Large Objects with Chiral Material

In this section, the first example we consider is a chiral sphere with diameter $d = 2.0\lambda_0$. The constitutive parameters are: $\epsilon_r = 2$, $\mu_r = 1$, $\xi_r = \frac{\xi}{\sqrt{\mu\epsilon}} = 0.3$. The bistatic RCS results are calculated using 218,602 unknowns. Fig. 4.10 shows the bistatic RCS values of the sphere in x-z plane calculated using our code and also the Mie series [42] for comparison. From Fig. 4.10, we can conclude that the RCS results calculated from our code are in a good agreement with Mie series.

In the second example, we consider a conducting cone coated with dispersive chiral material show in Fig. 4.11(a). The base diameter of the cone is 1.2 m and the cross section of the cone is a equilateral triangle. The thickness of the coating is 0.03 m. The constitutive equations for dispersive chiral media can be written as

$$\boldsymbol{D}(\omega) = \epsilon_0\epsilon_r(\omega)\boldsymbol{E}(\omega) - j\kappa(\omega)\sqrt{\epsilon_0\mu_0}\boldsymbol{H}(\omega) \tag{4.60}$$

$$\boldsymbol{B}(\omega) = \mu_0\mu_r(\omega)\boldsymbol{H}(\omega) + j\kappa(\omega)\sqrt{\epsilon_0\mu_0}\boldsymbol{E}(\omega). \tag{4.61}$$

In most of the cases, the Lorentz model is used to characterize the dispersive nature of permittivity and permeability. The Lorentz model is in the form of

$$\epsilon_r(\omega) = \epsilon_{\infty r} + \frac{(\epsilon_{sr} - \epsilon_{\infty r})\omega_\epsilon^2}{\omega_\epsilon^2 - \omega^2 + j2\omega_\epsilon\xi_\epsilon\omega} \tag{4.62}$$

$$\mu_r(\omega) = \mu_{\infty r} + \frac{(\mu_{sr} - \mu_{\infty r})\omega_\mu^2}{\omega_\mu^2 - \omega^2 + j2\omega_\mu\xi_\mu\omega}. \tag{4.63}$$

The Condon model [50] is generally used to describe the dispersive nature of chirality. The Condon model is in the form of

$$\kappa(\omega) = \frac{\tau_\kappa\omega_\kappa^2\omega}{\omega_\kappa^2 - \omega^2 + j2\omega_\kappa\xi_\kappa\omega}. \tag{4.64}$$

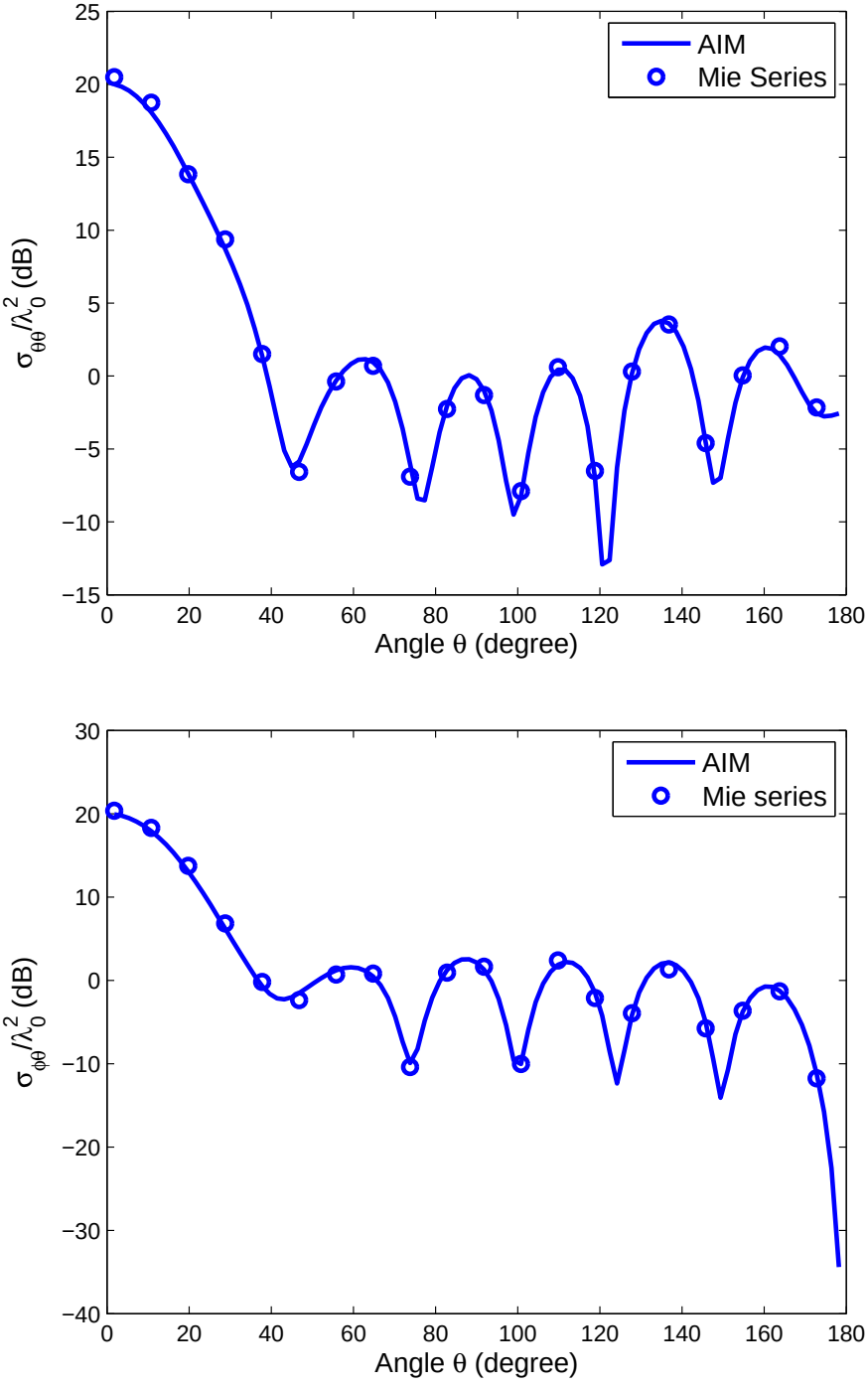

Figure 4.10: Bistatic RCS of a chiral sphere with diameter $d = 2.0\lambda_0$, $\epsilon_r = 2$, $\mu_r = 1$, and $\xi_r = 0.3$ in x-z plane. (a) Co-polarized Bistatic RCS; (b) cross-polarized bistatic RCS.

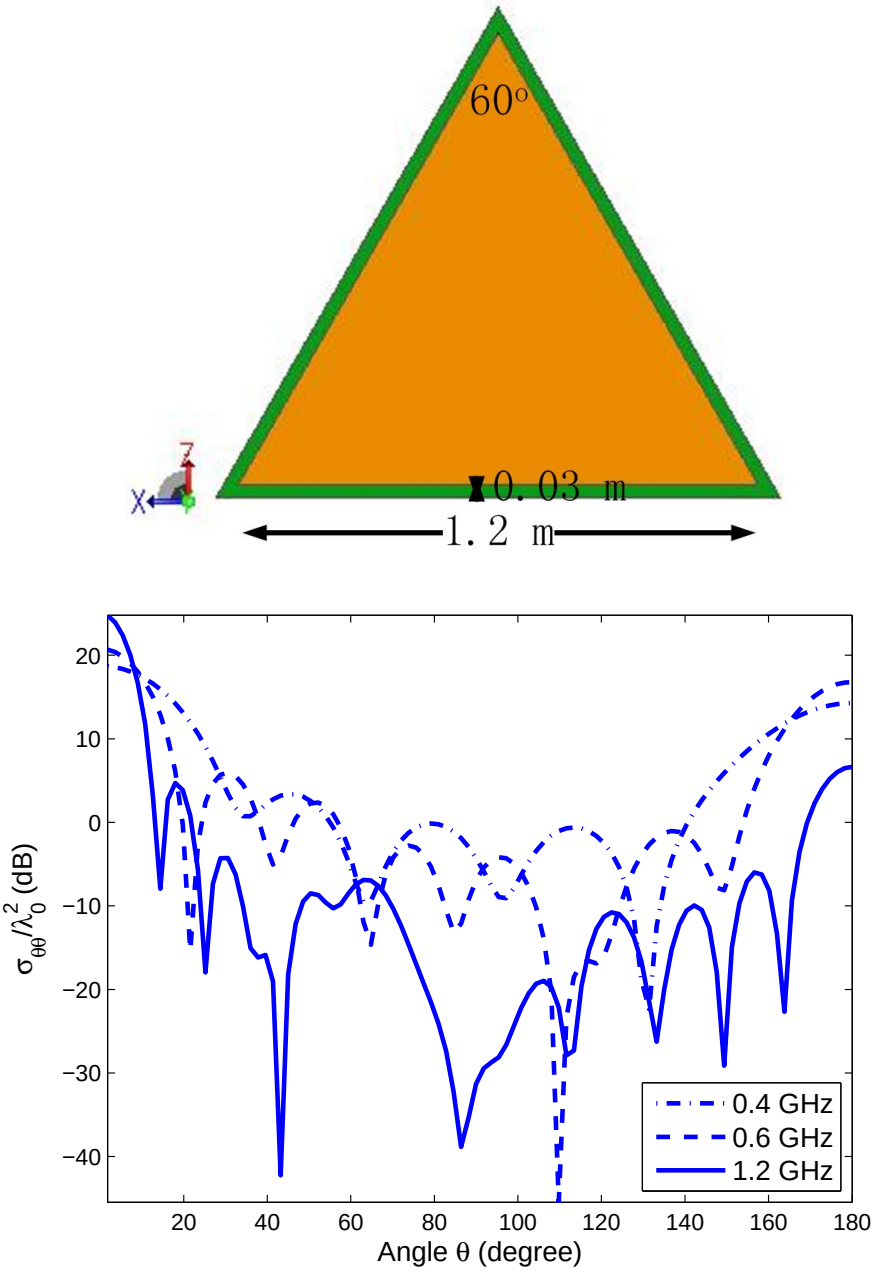

Figure 4.11: (a) The cross section of conducting cone coated with dispersive chiral material; (b) Bistatic RCS of the conducting cone coated with dispersive chiral material shown in Fig. 4.11(a) in x-z plane at different frequencies.

If a chiral material with the following parameters is considered,

$$\begin{aligned} \epsilon_{\infty r} = 2; \quad \epsilon_{sr} = 5; \quad \omega_\epsilon = 2\pi \times 2 \times 10^9; \quad \xi_\epsilon = 0.5 \\ \mu_{\infty r} = 1.1; \quad \mu_{sr} = 1.8; \quad \omega_\mu = 2\pi \times 2 \times 10^9; \quad \xi_\mu = 0.5 \\ \tau_\kappa = \tfrac{0.5}{\omega_\kappa}; \quad \omega_\kappa = 2\pi \times 2 \times 10^9; \quad \xi_\kappa = 0.3, \end{aligned} \tag{4.65}$$

the constitutive parameters can be evaluated at different frequencies. We have, at 0.4 GHz, $\epsilon_r = 4.9950 - 0.6240j, \mu_r = 1.7988 - 0.1456j, \kappa = 0.1026 - 0.0128j$; at 0.6 GHz, $\epsilon_r = 4.9735 - 0.9803j, \mu_r = 1.7938 - 0.2287j, \kappa = 0.1586 - 0.0314j$; at 1.2 GHz, $\epsilon_r = 4.4948 - 2.3389j, \mu_r = 1.6821 - 0.5457j, \kappa = 0.3561 - 0.2003j$. The RCS values are calculated using 261,287 unknowns. The RCS's calculated at different frequencies are shown in Fig. 4.11(b).

4.4.4 Large Objects with Uniaxial Anisotropic Material

In this section, the first example we consider is a conducting sphere with diameter $d = 3.0\lambda_0$ coated with uniaxial anisotropic material of a thickness $0.1\lambda_0$. The constitutive parameters are $\epsilon_t = 2.0 - 0.1j, \epsilon_z = 4.0 - 0.2j$ and $\mu_t = 2.0 - 0.1j, \mu_z = 4.0 - 0.2j$. The bistatic RCS results are calculated using 289,295 unknowns. Fig. 4.12 shows the bistatic RCS of the sphere calculated using our code and also the spherical vector wave functions [44] for comparison. From Fig. 4.12, we can conclude that the RCS results calculated from our code are in a good agreement with that obtained from the spherical vector wave functions method.

The second example is a conducting cube coated with uniaxial anisotropic material and the cross-section of the cube shown in Fig. 4.13(a). The side of the cube is $3\lambda_0$ and thickness of the coating material is $0.1\lambda_0$. The consti-

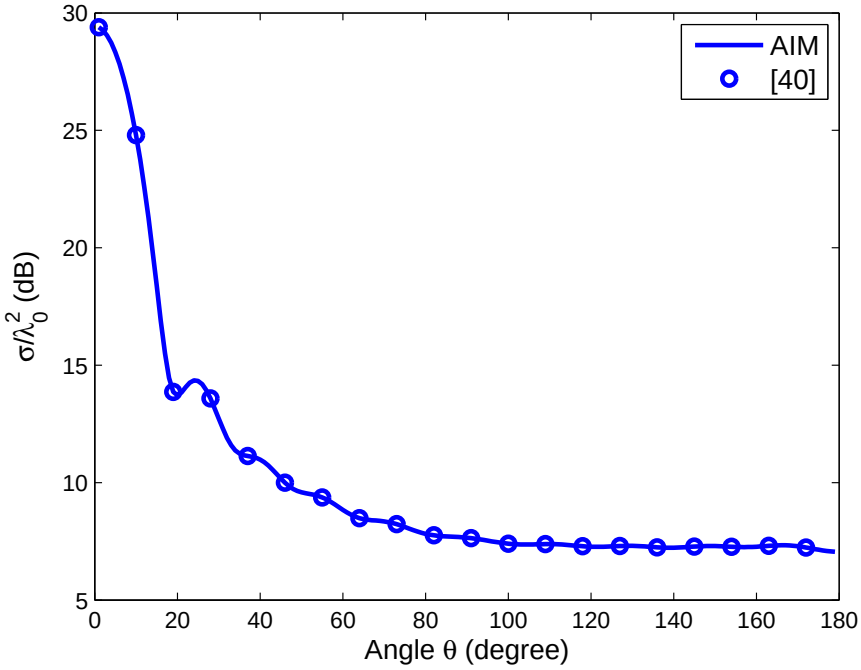

Figure 4.12: Bistatic RCS in x-z plane of a conducting sphere with diameter $d = 3.0\lambda_0$ coated with uniaxial anisotropic material with thickness $0.1\lambda_0$.

tutive parameters are: $\overline{\boldsymbol{\epsilon}} = \epsilon_0 \begin{pmatrix} 2 & 0 & 0 \\ 0 & 2 & 0 \\ 0 & 0 & 5 \end{pmatrix}$ and $\overline{\boldsymbol{\mu}} = \mu_0 \begin{pmatrix} 3 & 0 & 0 \\ 0 & 3 & 0 \\ 0 & 0 & 1 \end{pmatrix}$. The bistatic RCS values of the cube are computed using 133,476 and 264,508 unknowns and shown in Fig. 4.13(b). From Fig. 4.13(b), it is clear that the result has converged.

4.4.5 Large Objects with Gyroelectric Material

In this section, we first consider an example of electromagnetic scattering by a conducting sphere coated with gyroelectric material. The diameter of the sphere is $3.0\lambda_0$ and the thickness of the layer is $0.1\lambda_0$. The permittivity tensor is $\overline{\boldsymbol{\epsilon}} = \epsilon_0 \begin{pmatrix} 2.0 - 0.1j & j & 0 \\ -j & 2.0 - 0.1j & 0 \\ 0 & 0 & 4.0 - 0.2j \end{pmatrix}$. The calculated RCS results are computed with 289,295 unknowns and shown in Fig. 4.14.

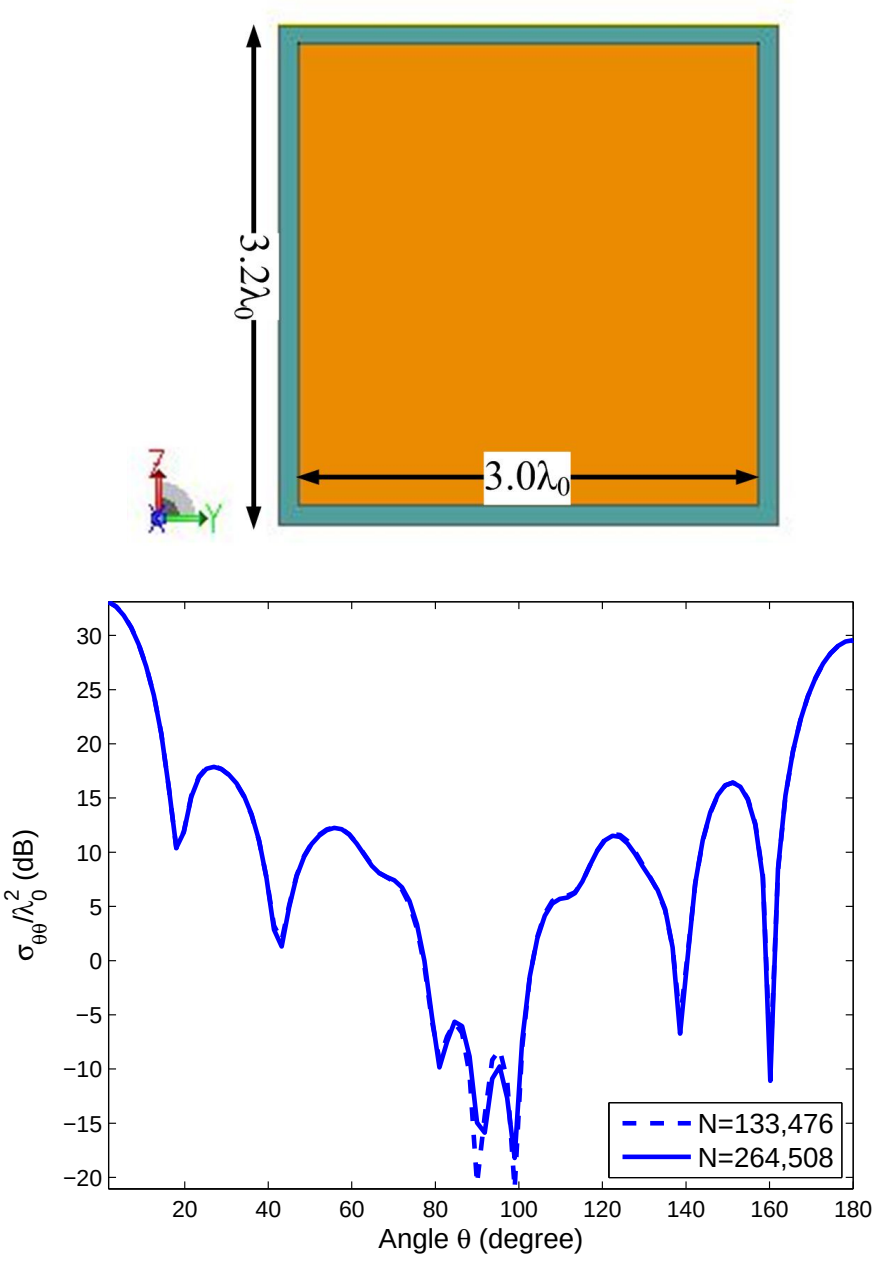

Figure 4.13: (a) The cross section of a conducting cube coated with anisotropic material; (b) Bistatic RCS of the cube shown in Fig. 4.13(a).

Also the result computed using vector wave function expansion method [47] is presented for comparison and a good agreement has been observed.

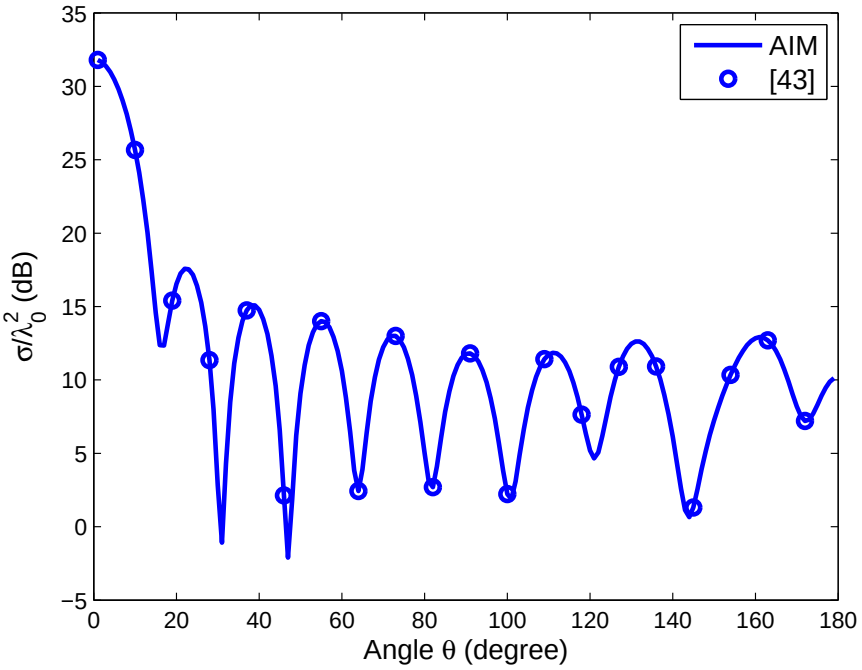

Figure 4.14: Bistatic RCS of a conducting sphere with the diameter $3.0\lambda_0$, coated with gyroelectric material with the thickness of $0.1\lambda_0$.

The second example is a conducting structure coated with gyroelectric material and the cross-section of the structure is shown in Fig. 4.15(a). It is composed of a semi-sphere with diameter $3\lambda_0$ and the height of the cylinder is $3\lambda_0$. The thickness of the coating material is $0.1\lambda_0$. The constitutive parameters are: $\overline{\boldsymbol{\epsilon}} = \epsilon_0 \begin{pmatrix} 2 & j & 0 \\ -j & 2 & 0 \\ 0 & 0 & 5 \end{pmatrix}$. The bistatic RCS of the cube is computed using 130,942 and 271,341 unknowns and shown in Fig. 4.15(b). From Fig. 4.15(b), it is clear that the result has converged.

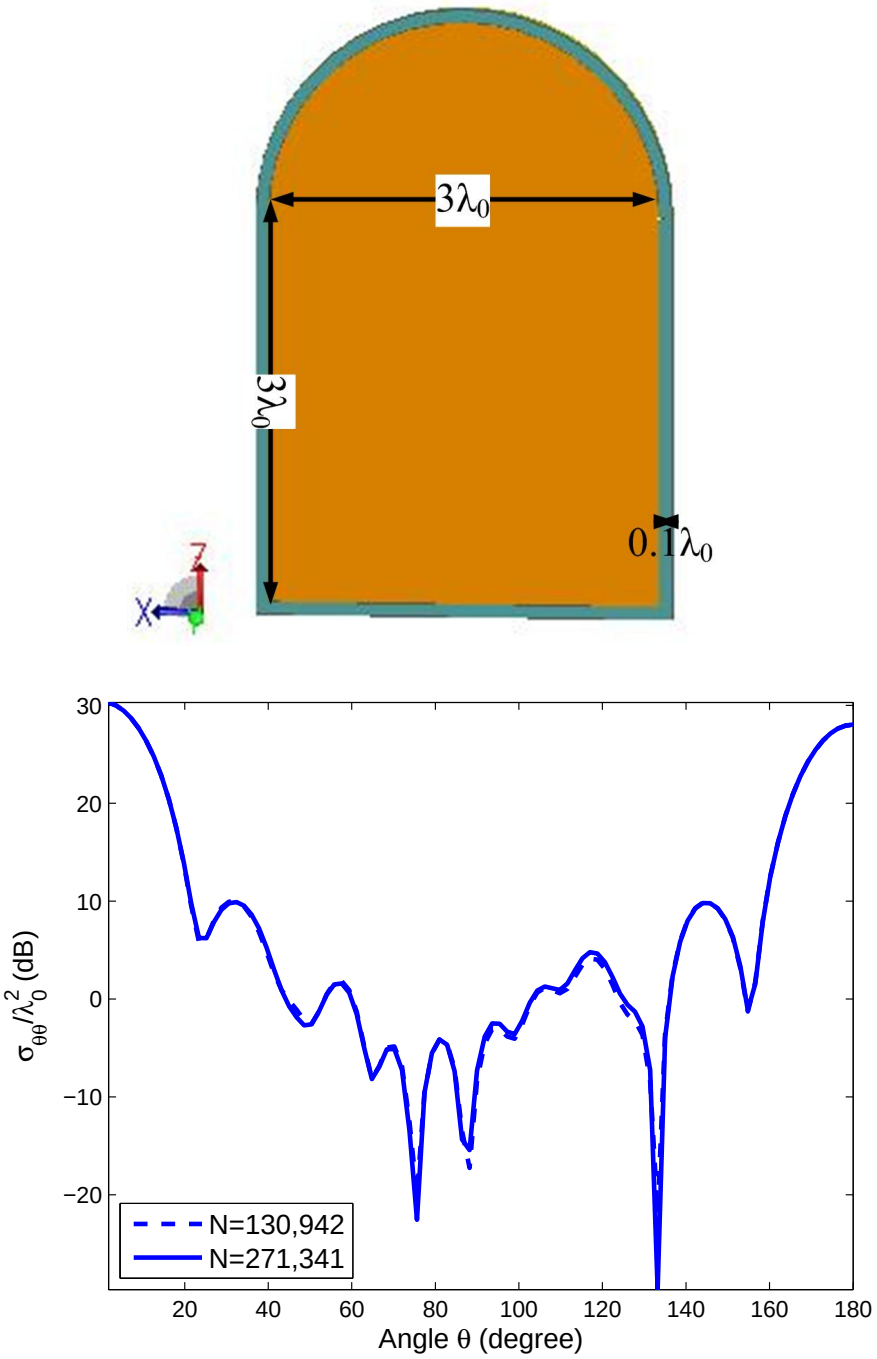

Figure 4.15: (a) The cross section of a conducting structure coated with gyroelectric material; (b) Bistatic RCS of the structure shown in Fig. 4.15(a).

4.4.6 Large Objects with Gyromagnetic Material

In this section, the first example is a conducting sphere coated with gyromagnetic material with permeability tensor:

$$\overline{\boldsymbol{\mu}} = \mu_0 \begin{pmatrix} 2.0 - 0.1j & 1.0j & 0 \\ -1.0j & 2.0 - 0.1j & 0 \\ 0 & 0 & 4.0 - 0.2j \end{pmatrix}.$$ The diameter of the conducting sphere is $3.0\lambda_0$ and the coated thickness is $0.1\lambda_0$, respectively. The calculated RCS results are computed with 295,289 unknowns and shown in Fig. 4.16. Also the result computed using vector wave function expansion method [48] is presented for comparison and a good agreement has been observed.

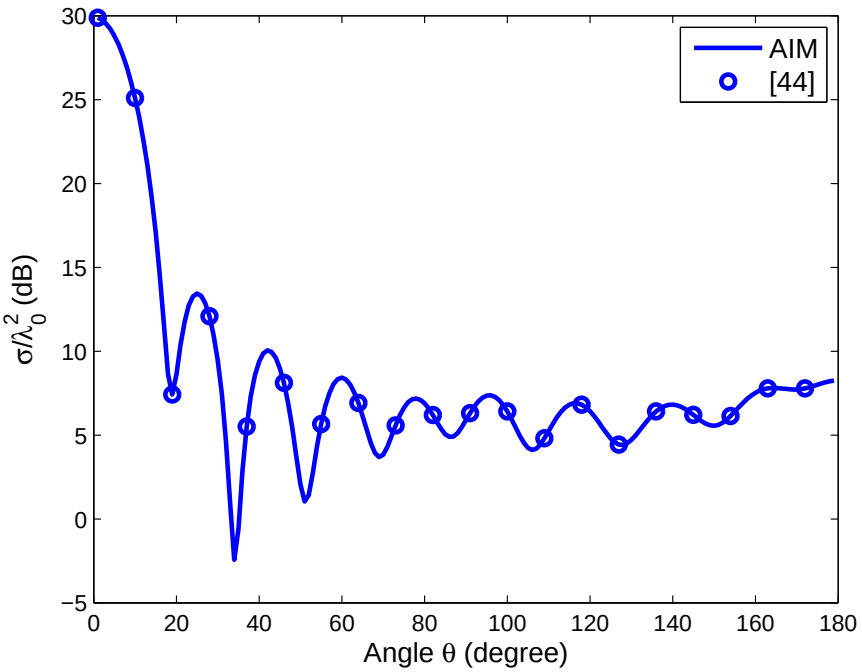

Figure 4.16: Bistatic RCS of a a conducting sphere coated with gyromagnetic material. The diameter of the conducting sphere is $3.0\lambda_0$ and the coated thickness is $0.1\lambda_0$.

The second example is a conducting structure coated with gyromagnetic material shown in Fig. 4.17(a). The structure is the combination of a

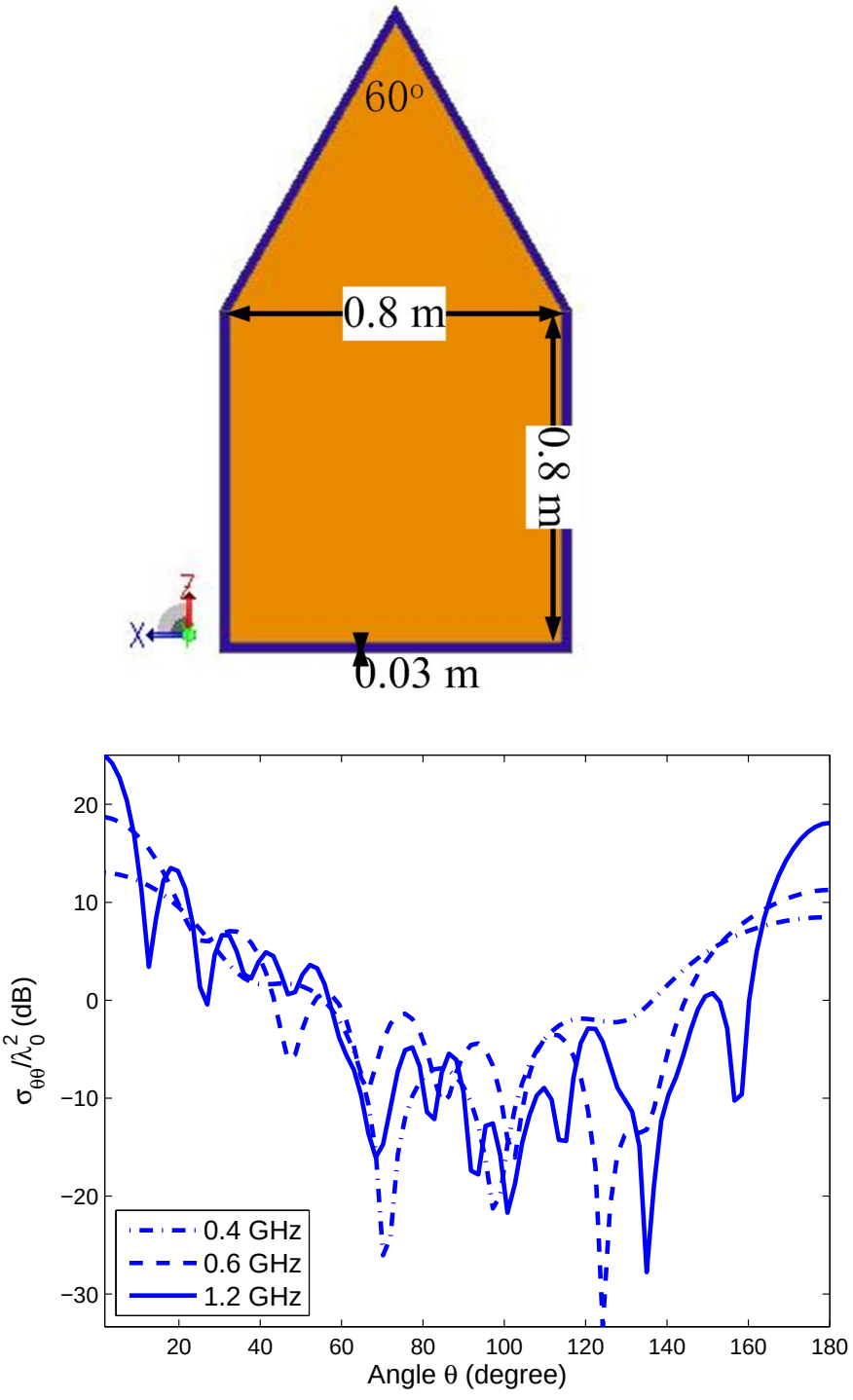

Figure 4.17: (a) A conducting structure coated with gyromagnetic material; (b) Bistatic RCS of the conducting structure shown in Fig. 4.17(a) coated with gyromagnetic material in x-z plane at different frequencies.

cylinder with diameter 0.8 m, height 0.8 m and a cone whose cross section is an equilateral triangle with side length 0.8 m. The coating is 0.03 m thick. When biased by a DC magnetic field $\boldsymbol{B}_0 = \hat{a}_z B_0$, gyromagnetic materials, whose permittivity tensor $\overline{\boldsymbol{\epsilon}} = \epsilon_0 \overline{\boldsymbol{I}}$, are characterized by their permeability tensors $\overline{\boldsymbol{\mu}} = \mu_0 \overline{\boldsymbol{\mu}}_r$ where with constitute parameters with permeability tensor $\overline{\boldsymbol{\mu}}_r = \begin{pmatrix} \mu_1 & j\mu_2 & 0 \\ -j\mu_2 & \mu_1 & 0 \\ 0 & 0 & \mu_3 \end{pmatrix}$ where the elements in the permeability tensor are formulated as [103]:

$$\mu_1 = 1 + \frac{(\omega_0 + j\omega\alpha)\omega_m}{(\omega_0 + j\omega\alpha)^2 - \omega^2} \tag{4.66}$$

$$\mu_1 = \frac{\omega\omega_m}{(\omega_0 + j\omega\alpha)^2 - \omega^2} \tag{4.67}$$

$$\mu_3 = 1 \tag{4.68}$$

where α is the ferrite damping factor, ω_0 is the Larmor precession frequency, and ω_m is the saturation magnetization frequency. The Larmor precession frequency ω_0 and the saturation magnetization frequency ω_m are determined by the DC magnetic field bias by [103]:

$$\omega_0 = \gamma_m H_0 \tag{4.69}$$

$$\omega_m = \gamma_m M_0 \tag{4.70}$$

where γ_m is the gyromagnetic ratio, H_0 is the magnitude of the applied DC magnetic field, and M_0 is the magnitude of saturated magnetization vector. $\boldsymbol{M}_0$ is in the same direction of the applied magnetic field $\boldsymbol{H}_0$.

Once the Larmor precession frequency, saturation magnetization frequency, and ferrite damping factor are given, the permeability tensor $\overline{\boldsymbol{\mu}}$ can be evaluated at any frequency. For example, if we consider a ferrite

material with the parameters of

$$\alpha = 0.1 \tag{4.71}$$

$$\omega_0 = 2\pi \times 2 \times 10^9 \tag{4.72}$$

$$\omega_m = 2\pi \times 2 \times 10^9 \tag{4.73}$$

we have, at 0.4 GHz, $\overline{\boldsymbol{\mu}}_r = \begin{pmatrix} 2.0412 - 0.0226j & 0.0087 + 0.2081j & 0 \\ -0.0087 - 0.2081j & 2.0412 - 0.0226j & 0 \\ 0 & 0 & 1 \end{pmatrix}$

at 0.6 GHz, $\overline{\boldsymbol{\mu}}_r = \begin{pmatrix} 2.0974 - 0.0394j & 0.0217 + 0.3286j & 0 \\ -0.0217 - 0.3286j & 2.0974 - 0.0394j & 0 \\ 0 & 0 & 1 \end{pmatrix}$

at 1.2 GHz, $\overline{\boldsymbol{\mu}}_r = \begin{pmatrix} 2.5346 - 0.1951j & 0.1717 + 0.9104j & 0 \\ -0.1717 - 0.9104j & 2.5346 - 0.1951j & 0 \\ 0 & 0 & 1 \end{pmatrix}$.

The calculated RCS results are computed with 276,875 unknowns and shown in Fig. 4.17(b).

4.4.7 A Large Object coated with Faraday Chiral Material

In this section, we consider an example of electromagnetic scattering by a large conducting object coated with faraday chiral material. The structure considered is shown in Fig. 4.18(a). The structure is the combination of a semi-sphere with diameter $4.0\lambda_0$ and a cone whose cross section is an equilateral triangle with side length $4.0\lambda_0$. The coating is $0.1\lambda_0$

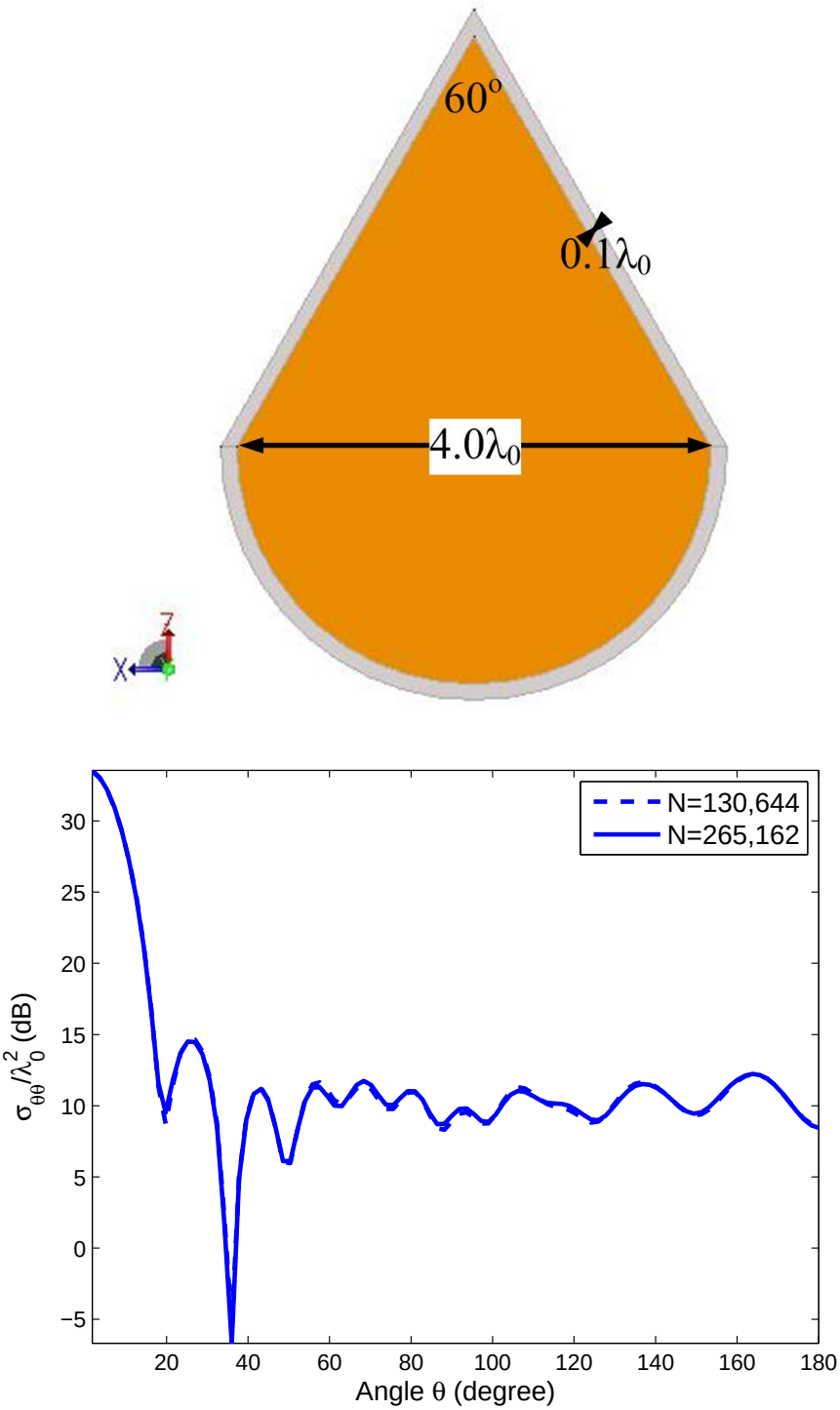

Figure 4.18: (a) A conducting structure coated with faraday chiral material; (b) Bistatic RCS of the conducting structure coated with Faraday chiral material shown in Fig. 4.18(a) in x-z plane.

thick with constitute parameters as follows: $\overline{\boldsymbol{\epsilon}} = \epsilon_0 \begin{pmatrix} 2.0 & 0.3j & 0 \\ -0.3j & 2.0 & 0 \\ 0 & 0 & 3.0 \end{pmatrix}$, $\overline{\boldsymbol{\mu}} = \mu_0 \begin{pmatrix} 1.5 & 0.2j & 0 \\ -0.2j & 1.5 & 0 \\ 0 & 0 & 2.0 \end{pmatrix}$, $\overline{\boldsymbol{\xi}} = \sqrt{\mu_0\epsilon_0} \begin{pmatrix} -0.3j & 0.1 & 0 \\ -0.1 & -0.3j & 0 \\ 0 & 0 & -0.2j \end{pmatrix}$, $\overline{\boldsymbol{\zeta}} = \sqrt{\mu_0\epsilon_0} \begin{pmatrix} 0.3j & -0.1 & 0 \\ 0.1 & 0.3j & 0 \\ 0 & 0 & 0.2j \end{pmatrix}$. The calculated RCS results are computed with 130,644 and 265,162 unknowns and shown in Fig. 4.18(b). From Fig. 4.18(b), it is clear that the result has converged.

Chapter 5

ASED-AIM Analysis of Scattering by Periodic Structures

In this Chapter, the Adaptive Integral Method (AIM) has been extended to characterize electromagnetic scattering by large scale finite periodic arrays with each cell comprising of either dielectric or metallic objects, by utilizing accurate sub-entire-domain (ASED) basis function. The solution process can be carried out in two steps. In the first step, a small problem is solved in order to construct ASED basis functions to be implemented for the second step. This problem consists of nine unit cells for two dimensional periodic arrays and 27 unit cells for three dimensional periodic arrays. When dielectric materials are involved in the cell which results in a large number of unknowns for the small problem, the AIM can be used to accelerate the solution process and reduce the memory requirement. In the second step, the entire problem is solved using the ASED basis function constructed in the first step. The AIM can be enhanced with the ASED basis function implemented to solve the entire problem more efficiently. When calculating the near interaction impedance matrix, computation time can be significantly

reduced by using the near impedance matrix in the first step. The complexity analysis shows that the computational time is $O(N \log N)+O(M \log M)$ and memory requirement is $O(N) + O(M)$, where M denotes the number of cells and N stands for the number of elements in one cell. The results calculated respectively by the ASED-AIM and the existing AIM are then compared and an excellent agreement has been observed, which demonstrates the accuracy of the proposed method. In the meantime, memory and computational time requirements have been considerably reduced using the ASED-AIM as compared to the existing AIM. Finally, an example with over 10 million unknowns is given to demonstrate the efficiency of the proposed method.

5.1 ASED-AIM Formulation

Electromagnetic scattering by periodic arrays of composite dielectric and metallic structures can be characterized using volume-surface integral equation (VSIE) method. The basic equations are formulated below via the boundary conditions satisfied by electric and magnetic field tangential components:

$$\boldsymbol{E}^{\text{inc}}(\boldsymbol{r}) = \boldsymbol{E}(\boldsymbol{r}) - \boldsymbol{E}^{\text{sca}}(\boldsymbol{r}), \quad \boldsymbol{r} \in V \tag{5.1}$$

$$\boldsymbol{E}^{\text{inc}}(\boldsymbol{r})\Big|_{\text{tan}} = -\boldsymbol{E}^{\text{sca}}(\boldsymbol{r})|_{\text{tan}}, \quad \boldsymbol{r} \in S. \tag{5.2}$$

Equivalent electric volume current $\boldsymbol{J}_V(\boldsymbol{r})$ and equivalent electric surface current $\boldsymbol{J}_S(\boldsymbol{r})$ are related to total electric field $\boldsymbol{E}(\boldsymbol{r})$ and scattered electric field $\boldsymbol{E}^{\text{sca}}(\boldsymbol{r})$ via

$$\boldsymbol{J}_V(\boldsymbol{r}) = j\omega\kappa\boldsymbol{D}(r) = j\omega(\epsilon - \epsilon_0)\boldsymbol{E}(r), \quad \boldsymbol{r} \in V \tag{5.3}$$

$$\boldsymbol{E}^{\text{sca}}(\boldsymbol{r}) = -j\omega\mu_0 \int_V G(\boldsymbol{r}, \boldsymbol{r}')\boldsymbol{J}_V(\boldsymbol{r}')dV'$$

$$
\begin{aligned}
&-j\omega\mu_0 \int_S G(\boldsymbol{r},\boldsymbol{r}')\boldsymbol{J}_S(\boldsymbol{r}')dS' \\
&+\frac{\nabla}{j\omega\epsilon_0}\int_V G(\boldsymbol{r},\boldsymbol{r}')\nabla'\cdot\boldsymbol{J}_V(\boldsymbol{r}')dV' \\
&+\frac{\nabla}{j\omega\epsilon_0}\int_S G(\boldsymbol{r},\boldsymbol{r}')\nabla'\cdot\boldsymbol{J}_S(\boldsymbol{r}')dS'
\end{aligned} \tag{5.4}
$$

where $G(\boldsymbol{r},\boldsymbol{r}')$ denotes free space Green's function, μ_0 and ϵ_0 represent free space permeability and permittivity respectively, ϵ stands for permittivity in the dielectric object, and $\kappa = (\epsilon - \epsilon_0)/\epsilon$ identifies the contrast ratio of scatterer material and its background medium.

For simplicity, we consider 2D large scale periodic structures. Three dimensional periodic problems can be analyzed in the same fashion. If there are N unknowns for each cell and M cells, the total number of unknowns will be MN. This number of unknowns can be significantly reduced to M via the ASED method. The basic idea of the ASED method is to first construct the macro basis functions for each cell and then using this basis function to represent a cell for the solution of the whole array. In order to construct the macro basis functions, the ASED method is proposed to first solve a small array problem. If the whole array is considered to construct the ASED basis function, we can get the exact basis function to represent the cell but the computational burden is too large. In order to balance the computational burden and the accuracy, the ASED method is proposed to solve a nine cell problem shown in Fig. 5.1(a) which takes the most important coupling from the nearest neighbor into consideration [92].

For the p-th cell, where $p = 0, \ldots, 8$, surface currents can be expanded, in order to ensure the normal continuity of surface current in the metallic surface, as follows:

$$
\boldsymbol{J}_p^S = \sum_{m=1}^{N_S} I_{p_m}^S \boldsymbol{f}_{p_m}^S. \tag{5.5}
$$

In order to ensure the normal continuity of electric flux density inside the

dielectric objects, $\boldsymbol{D}_p$ can be expanded as:

$$\boldsymbol{D}_p = \frac{1}{j\omega} \sum_{m=1}^{N_V} I_{p_m}^V \boldsymbol{f}_{p_m}^V \tag{5.6}$$

thus, volume currents can be expanded as

$$\boldsymbol{J}_p^V = \sum_{m=1}^{N_V} I_{p_m}^V \kappa \boldsymbol{f}_{p_m}^V \tag{5.7}$$

where $\boldsymbol{f}_{p_m}^S$ and $\boldsymbol{f}_{p_m}^V$ denote respectively the RWG and SWG basis functions associated with the m-th surface and volume basis functions of the p-th cell, N_S is the number of RWG basis functions while N_V is the number of SWG basis functions, and $I_{p_m}^S$ and $I_{p_m}^V$ stand for the respective unknown coefficients to be solved for. Thus, electric current for the p-th cell can be written as

$$\boldsymbol{J}_p = \boldsymbol{J}_p^S + \boldsymbol{J}_p^V. \tag{5.8}$$

The total current for the nine cell problem can be written as

$$\boldsymbol{J} = \sum_{p=0}^{8} \boldsymbol{J}_p \tag{5.9}$$

where $\boldsymbol{J}_p, (p = 0, \ldots, 8)$ are the so-called ASED basis functions to be solved in the nine cell problem. We use the Galerkin procedure of MoM to test the volume-surface integral equations and obtain the following matrix equations:

$$\left(Z_{p_m q_n}\right)\left(I_{q_n}\right) = \left(V_{p_m}\right) \tag{5.10}$$

where p_m denotes the m-th testing function in the p-th cell while q_n stands for the n-th basis function in the q-th cell. The impedance matrix $\overline{\boldsymbol{Z}}$ comprises of 9×9 sub-matrices of size $N \times N$ with the p-th block row and the q-th block column representing the interaction among elements inside the (p, q)-th cell, where M denotes the total unknown number in a cell. For

the p-th block row and q-th block column sub-matrix, it can be written in terms of following block matrices

$$(Z_{p_m q_n}) = \begin{pmatrix} Z^{VV}_{p_m q_n} & Z^{VS}_{p_m q_n} \\ Z^{SV}_{p_m q_n} & Z^{SS}_{p_m q_n} \end{pmatrix} \tag{5.11}$$

whose detailed block matrix expressions can be written as

$$\begin{aligned} Z^{VV}_{p_m q_n} &= \frac{1}{j\omega} < \boldsymbol{f}^V_{p_m}, \frac{1}{\epsilon}\boldsymbol{f}^V_{q_n} > + j\omega\mu_0 < \boldsymbol{f}^V_{p_m}, \boldsymbol{A}^V_{q_n} > \\ &\quad - \frac{1}{j\omega\epsilon_0} < \boldsymbol{f}^V_{p_m}, \nabla\phi^V_{q_n} > \end{aligned} \tag{5.12}$$

$$Z^{VS}_{p_m q_n} = j\omega\mu_0 < \boldsymbol{f}^V_{p_m}, \boldsymbol{A}^S_{q_n} > - \frac{1}{j\omega\epsilon_0} < \boldsymbol{f}^V_{p_m}, \nabla\phi^S_{q_n} > \tag{5.13}$$

$$Z^{SV}_{p_m q_n} = j\omega\mu_0 < \boldsymbol{f}^S_{p_m}, \boldsymbol{A}^V_{q_n} > - \frac{1}{j\omega\epsilon_0} < \boldsymbol{f}^S_{p_m}, \nabla\phi^V_{q_n} > \tag{5.14}$$

$$\begin{aligned} Z^{SS}_{p_m q_n} &= < \boldsymbol{f}^S_{p_m}, \boldsymbol{f}^S_{q_n} > + j\omega\mu_0 < \boldsymbol{f}^S_{p_m}, \boldsymbol{A}^S_{q_n} > \\ &\quad - \frac{1}{j\omega\epsilon_0} < \boldsymbol{f}^S_{p_m}, \nabla\phi^S_{q_n} > \end{aligned} \tag{5.15}$$

where

$$\boldsymbol{A}^V_{q_n} = \int_V G\boldsymbol{f}^V_{q_n} dV' \tag{5.16}$$

$$\boldsymbol{A}^S_{q_n} = \int_S G\boldsymbol{f}^S_{q_n} dS' \tag{5.17}$$

$$\phi^V_{q_n} = \int_V G\nabla' \cdot \boldsymbol{f}^V_{q_n} dV' \tag{5.18}$$

$$\phi^S_{q_n} = \int_S G\nabla' \cdot \boldsymbol{f}^S_{q_n} dS'. \tag{5.19}$$

This matrix can be solved using the AIM when N becomes large. After solving the nine-cell problem, we can obtain the nine types of cell basis functions and the use them to solve the entire problem. Now the current density for the q-th cell, where $q = 1, \ldots, M$ (denoted by the superscript C herein and subsequently) can be written as

$$\boldsymbol{J}^C_q = j_q \boldsymbol{J}_p \tag{5.20}$$

$$\begin{pmatrix} \overline{\boldsymbol{Z}}^C_{11} & \overline{\boldsymbol{Z}}^C_{12} & \cdots & \overline{\boldsymbol{Z}}^C_{1M} \\ \overline{\boldsymbol{Z}}^C_{21} & \overline{\boldsymbol{Z}}^C_{22} & \cdots & \overline{\boldsymbol{Z}}^C_{2M} \\ \vdots & \vdots & \ddots & \vdots \\ \overline{\boldsymbol{Z}}^C_{M1} & \overline{\boldsymbol{Z}}^C_{M2} & \cdots & \overline{\boldsymbol{Z}}^C_{MM} \end{pmatrix} \cdot \begin{pmatrix} j_1 \\ j_2 \\ \vdots \\ j_M \end{pmatrix} = \begin{pmatrix} V^C_1 \\ V^C_2 \\ \vdots \\ V^C_M \end{pmatrix} \tag{5.21}$$

where j_q denotes unknowns to be solved for and the $\boldsymbol{J}_p, (p = 0, \ldots, 8)$ denotes one of the nine ASED basis functions. The corresponding relationship between the whole array and the ASED basis functions are shown in Fig. 5.1. Thus, the reduced matrix equations can be written as Eqn. (6.13). The cell impedance matrix elements can be written as

$$Z^C_{pq} = \sum_{m=1}^{M} \sum_{n=1}^{M} I_{p_m} Z_{p_m q_n} I_{q_n} \tag{5.22}$$

where $Z_{p_m q_n}$ is the original matrix element. It is noted here that I_{p_m} and I_{q_n} are the elements of the ASED basis functions obtained earlier and we have to use the mapping in Fig. 5.1 to find the ASED basis functions for each cell impedance matrix element. The unknowns to be solved is $j_1, j_2, \ldots j_M$. These coefficients multiplied by the ASED basis functions define the actual current distributions on each cell. In other words, the ASED basis functions can be thought as the profile for the current distribution and j_p provides the magnitude of the distribution. $V^C_p = \boldsymbol{J}^T_p \cdot \boldsymbol{V}_p$ where $\boldsymbol{V}_p$ is the excitation vector for the p-th cell.

When M is large, we can use the AIM to accelerate the solution process. We should combine the ASED approach with the AIM to solve large-scale periodic structure problems. The basic idea of AIM is to calculate the far-zone interaction via projecting the basis functions to, and interpolating potentials from, grid space associated with each basis function while the near zone interactions can be directly calculated. Since free space Green's function is translational invariant and the calculation is made based on grid space, the FFT can be used to greatly reduce the memory requirement

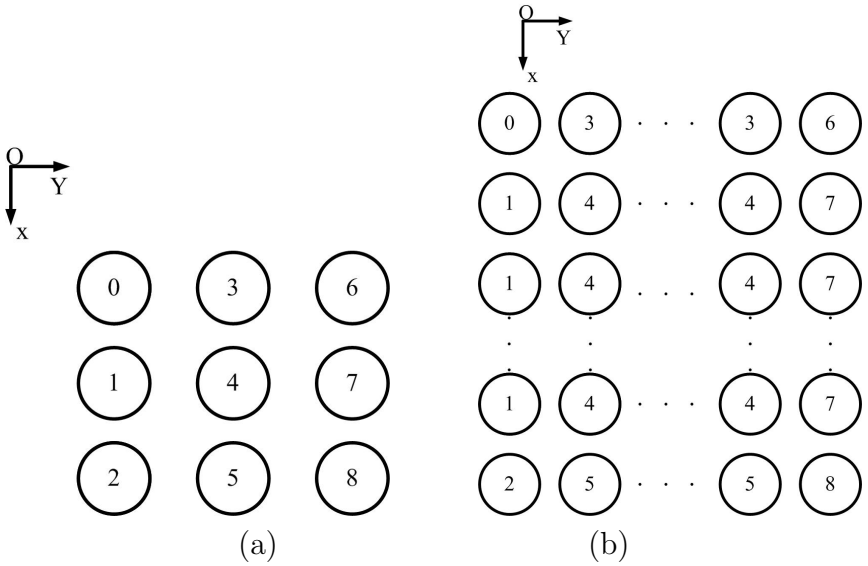

Figure 5.1: Mapping of the ASED basis functions. (a) The nine-cell problem; (b) The entire problem.

and computational time. Using the conventional AIM, the matrix vector multiplication can be written as

$$\overline{\boldsymbol{Z}}\boldsymbol{I} = \overline{\boldsymbol{V}}\,\overline{\boldsymbol{H}}\,\overline{\boldsymbol{P}}\,\boldsymbol{I} + \overline{\boldsymbol{Z}}^{\text{near}}\boldsymbol{I} \tag{5.23}$$

where $\overline{\boldsymbol{V}}$ is the interpolation matrix, $\overline{\boldsymbol{H}}$ is the Green's function matrix, and $\overline{\boldsymbol{P}}$ is the projection matrix. The mapping and calculations are made using the following four steps:

1. to project the sources distributed on the basis functions onto the regular grids by matching their vector and scalar potentials at some given test points to guarantee the approximate equality of their far fields;

2. to evaluate the potentials at other grid locations produced by these grid-projected sources by a 3-D convolution;

3. to interpolate the grid point potentials onto the testing functions, where the projection and interpolation operators are represented by

sparse matrices, and the convolution can be carried out rapidly using discrete FFTs; and

4. to compute the near-field interactions directly and remove the errors introduced by the far-field operators.

The four steps of conventional AIM can be shown in Fig. 5.2(a). For the

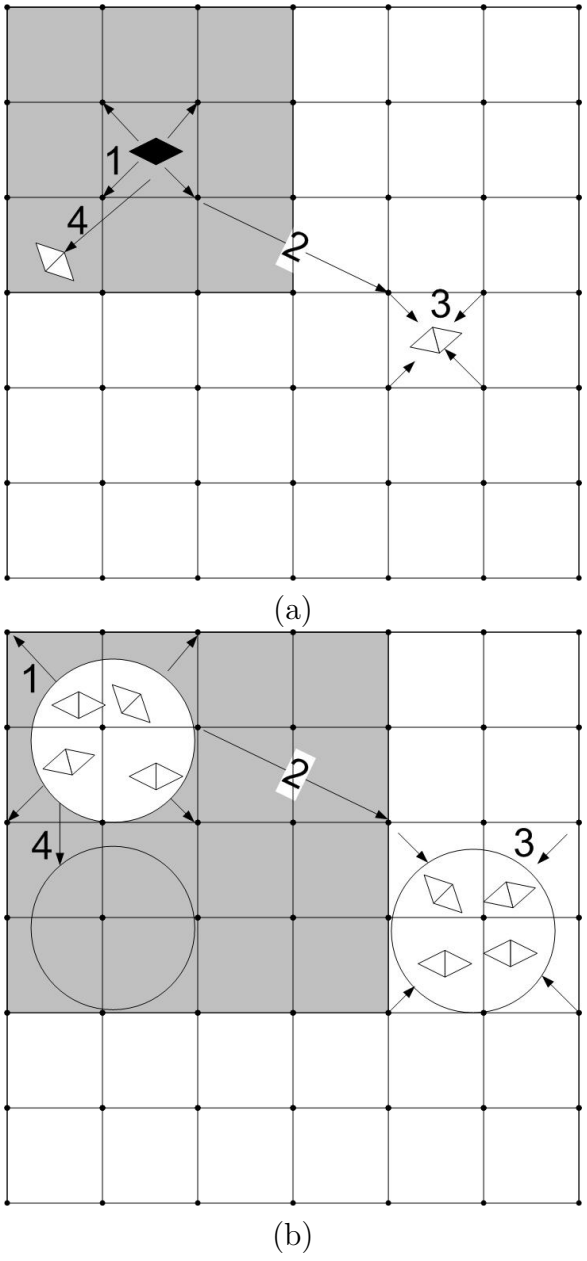

Figure 5.2: (a) The pictorial representation of the conventional AIM; (b) The pictorial representation of the ASED-AIM.

far zone interaction, the impedance matrix elements can be approximated

as:

$$Z_{p_m q_n} \approx \tilde{Z}_{p_m q_n} = \sum_s \sum_t V_{m_s} H_{m_s n_t} P_{n_t} \tag{5.24}$$

where V_{m_s} and P_{n_t} denote the s-th and t-th interpolation and projection matrix coefficients for the m-th basis function and in p-th cell respectively. $\sum$ denotes summation of all the grids associated with the basis functions. Thus, for cell interaction in the far zone, we have

$$\begin{aligned} Z^C_{pq} &= \sum_m \sum_n I_{p_m} Z_{p_m q_n} I_{q_n} \\ &\approx \sum_m \sum_s \sum_n \sum_t I_{p_m} V_{m_s} H_{m_s n_t} I_{q_n} P_{n_t} \\ &= V^C_p H_{pq} P^C_q \end{aligned} \tag{5.25}$$

where the element is the sum of the contributions of m-th and n-th basis functions in the p-th and q-th cells respectively. We denote $\overline{\boldsymbol{V}}^C$ and $\overline{\boldsymbol{P}}^C$ as the interpolation and projection matrices for cell basis functions. They can be written explicitly as:

$$V^C_p = \sum_m \sum_s I_{p_m} V_{m_s} \tag{5.26}$$

$$P^C_q = \sum_n \sum_t I_{q_n} P_{n_t}. \tag{5.27}$$

Now, Using the ASED-AIM, the matrix vector multiplication can be written as

$$\overline{\boldsymbol{Z}}^C \cdot \overline{\boldsymbol{I}}^C = \overline{\boldsymbol{V}}^C \cdot \overline{\boldsymbol{H}} \cdot \overline{\boldsymbol{P}}^V \cdot \overline{\boldsymbol{I}}^C + \overline{\boldsymbol{Z}}^{C,\text{near}} \cdot \overline{\boldsymbol{I}}^C \tag{5.28}$$

which takes the four steps to manipulate as follows:

1. to sum-up all the projections from every basis functions within each cell;

2. to evaluate the potentials at other grid locations produced by these grid-projected sources using a 3-D convolution;

3. to interpolate the grid point potentials onto each cell rather than individual testing functions; and

4. to compute the near-field interactions directly from at most nine nearby neighbors.

The four steps for implementing the ASED-AIM is shown graphically in Fig. 5.2(b).

5.2 Complexity Analysis for ASED-AIM

In the first step of ASED-AIM, the conventional AIM is carried out to solve a problem with $9N$ unknowns. Thus, the memory requirement and computational time are $O(N)$ and $O(N \log N)$, respectively. It should be noted that in [94], the authors focused on metallic structures; thus, N is usually small for a cell. For example, when $N = 65$, then the memory requirement and computational time are not large. In this case, the MoM can be employed to solve the nine-cell problem. But it is not the case when composite metallic and dielectric objects are within a cell since N is large, for example, $N = 10^3$. Thus, this portion of memory and computational time should be taken into consideration as can be shown in the numerical results later. In the second step of ASED-AIM, since there are only nine types of cell basis functions, the memory requirement for interpolation and projection matrix is a constant C and the computational time is $O(M)$ where M denotes the number of cells in the whole domain. For the FFT operation, since the grid number Ng is proportional to the total number of cells M, thus the memory requirement is $O(M)$ and the computational time is $O(M \log M)$.

In [94], disaggregation (equivalent to interpolation in the AIM), aggregation (equivalent to projection in the AIM) and translation (equivalent to the FFT in the AIM) have to be carried for each k direction (which is of order N) respectively per iteration. However, interpolation, and projection are only need once and the FFT twice per iteration in the AIM, one for forward FFT and the other for the inverse FFT. Thus, the computational time can be reduced greatly. For the near interactions, the computational time will be quite large if we calculate directly using

$$Z_{pq}^{C,\text{near}} = Z_{pq}^{C} - \tilde{Z}_{pq}^{C} = \sum_{m=1}^{M} \sum_{n=1}^{M} I_{p_m} \left(Z_{p_m q_n} - \tilde{Z}_{p_m q_n} \right) I_{q_n} \tag{5.29}$$

since this operation takes $O(N^2)$ multiplication and addition. In fact, we can utilize the near zone interaction matrix Z^{near} in the first step. We know that Z^{near} is a sparse $9N \times 9N$ matrix, which is made up of 9×9 sub-matrices with each matrix $N \times N$ elements, each element is $\left(Z_{p_m q_n} - \tilde{Z}_{p_m q_n} \right)$. Consider the fifth row of the sub-matrices which are calculated when the cell p is surrounded by nine most near neighboring cells q, as shown in Fig. 5.1(a) where $p = 4$ and $q = 0, ..., 8$. The sub-matrices are all sparse, since

$$Z_{p_m q_n} - \tilde{Z}_{p_m q_n} = 0, \quad d_{p_m q_n} > d_{\text{near}} \tag{5.30}$$

where d_{near} is the near zone threshold. Thus, $O(N^2)$ multiplications and additions can be greatly reduced using sparse matrix vector multiplication. For the near zone interactions, there are at most nine near neighbors for each cell; thus the memory requirement and the computational time are $O(M)$. Therefore, the total memory requirement is

$$\mathcal{M} = O(N) + C + O(M) + O(M) = O(N) + O(M) \tag{5.31}$$

and the total computational time is

$$\mathcal{C} = O(M \log M) + O(N) + O(N \log N) + O(N) = O(M \log M) + O(N \log N). \tag{5.32}$$

5.3 Numerical Results using ASED-AIM

In this section, several examples will be given to demonstrate the validity and efficiency of our code to solve electromagnetic scattering by large scale periodic structures consisting of composite metallic and dielectric objects. The GMRES solver is adopted as the iterative solver and it terminates when the normalized residue falls below 10^{-3}.

5.3.1 2D Array Results

First, we consider a 2D periodic structure shown in Fig. 5.3. The unit cell is shown in Fig. 5.3. The dielectric object is an cube with length $0.2\lambda_0$ and $\epsilon_r = 4$. Above the cube is a metallic square patch with length $0.2\lambda_0$. The entire objects are discretized with 467 tetrahedrons and 36 triangles resulting in $N = 1087$ unknowns. In the first situation, we consider a 4×4 array in x-y plane, where the periodicity in x-y plane is $0.4\lambda_0$. Three cases are considered: the first case shown in Fig. 5.4 is normal incidence at $\theta_i = 0^o$ and $\phi_i = 0^o$; the second case shown in Fig. 5.5 is oblique incidence at $\theta_i = 45^o$ and $\phi_i = 0^o$; and the third case shown in Fig. 5.6 is grazing incidence at $\theta_i = 90^o$ and $\phi_i = 0^o$. The electric field is θ-polarized in all the cases. The total number of unknowns is $MN = 17,248$. The results generated by the ASED-AIM are compared with conventional AIM results and a good agreement has been observed. When the ASED-AIM is used to

solve the problem, only 169 MB memory is needed and the computational time is around 60 seconds for all three cases while using AIM, the memory requirement is 300 MB and the solver CPU time is 102 seconds. Further reduction of memory requirement and CPU time using the ASED-AIM will be demonstrated in later examples.

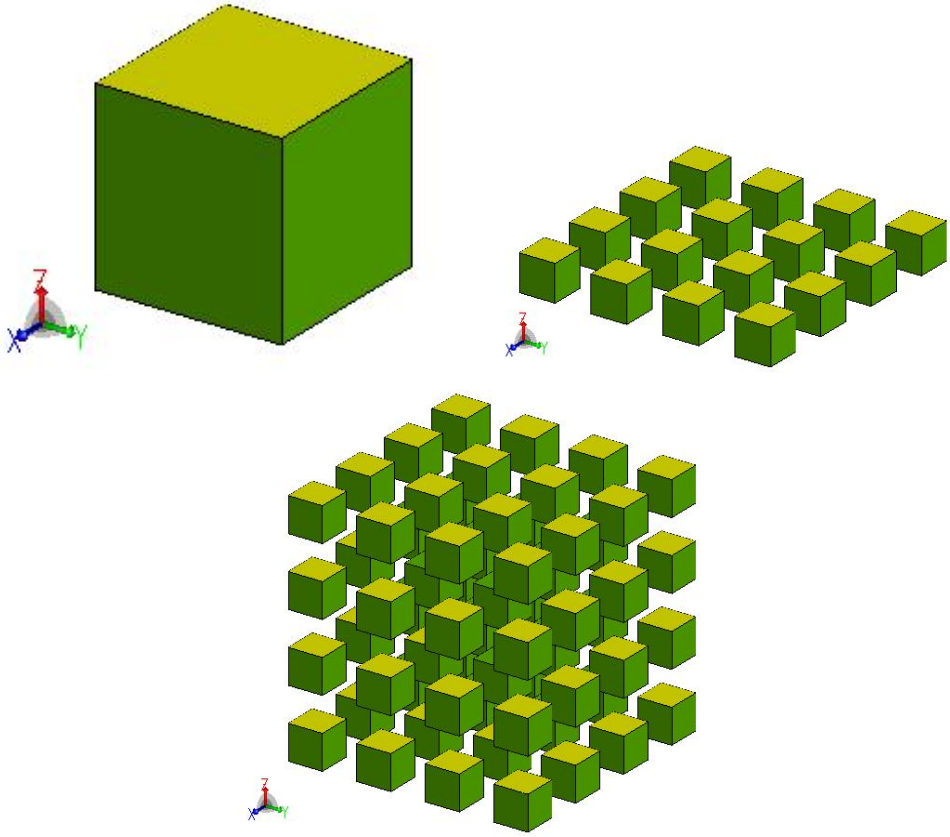

Figure 5.3: Examples of arrays used in the calculations of numerical results. (a) The structure of a unit cell, $d = 0.2\lambda_0$. The yellow face above the cube denotes a metallic patch while cube is a dielectric object with $\epsilon_r = 4$. (b) 4×4 array. (c) $4 \times 4 \times 4$ array.

Now, we consider three array cases: 6×6 array shown in Fig. 5.7, 8×8 array shown in Fig. 5.8, and 10×10 array shown in Fig. 5.9 at normal incident of plane wave which is θ-polarized. Comparison is made between the ASED-AIM results and the AIM results and a good agreement has been observed. The number of unknowns for the 6×6 array is 38,808 and it requires memory of 169 MB and computational time of 54 seconds when the ASED-AIM is used while it needs memory of 675 MB and computational

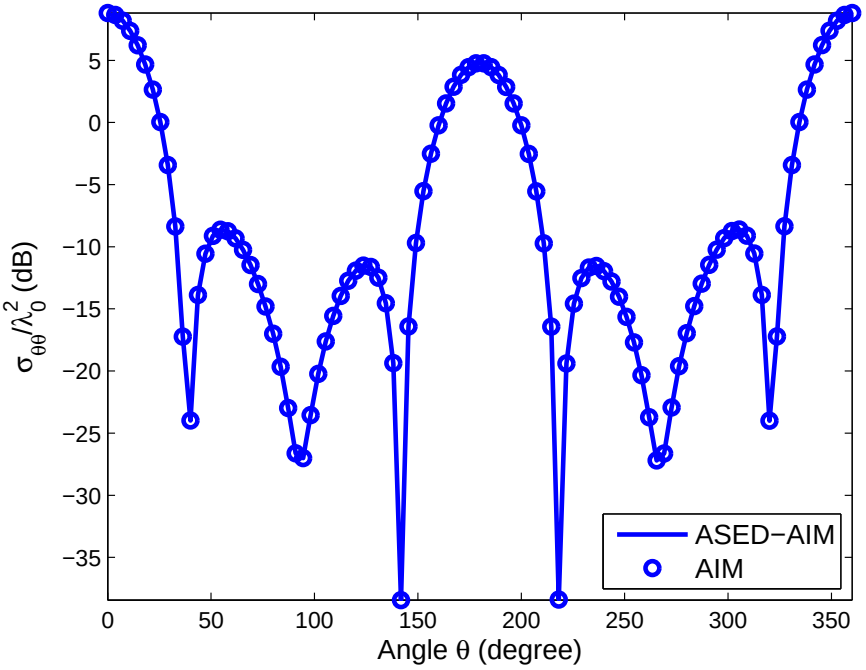

Figure 5.4: Bistatic RCS of the 4×4 array with each cell shown in Fig. 5.3 with electric field θ-polarized at the normal incidence ($\theta = 0^o$). The gap is $0.2\lambda_0$ in both x- and y-directions. The results are computed using the AIM (circle line) and the ASED-AIM (solid line).

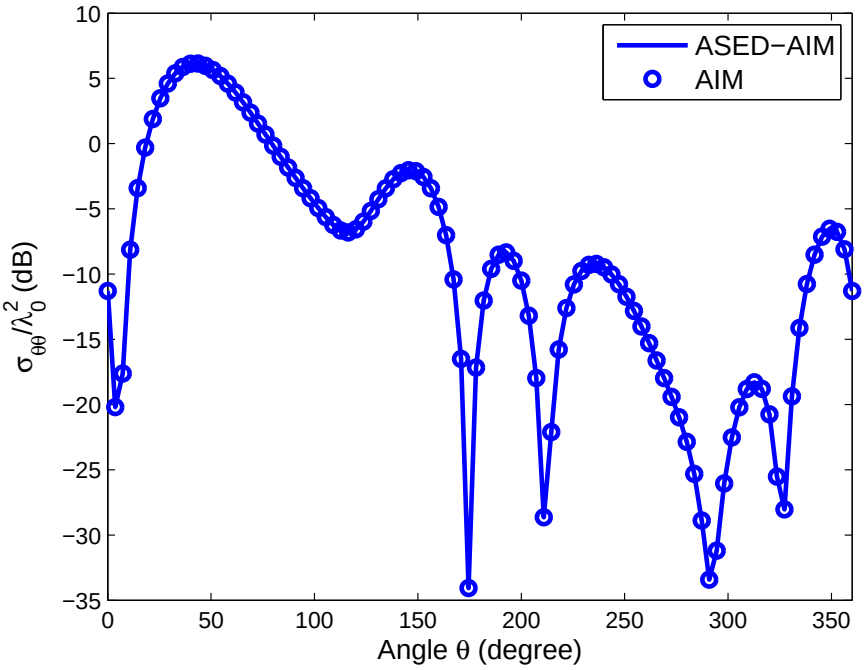

Figure 5.5: Bistatic RCS of the 4×4 array with each cell shown in Fig. 5.3 with electric field θ-polarized at the oblique incidence ($\theta = 45^o$). The gap is $0.2\lambda_0$ in both x- and y-directions. The results are computed using the AIM (circle line) and the ASED-AIM (solid line).

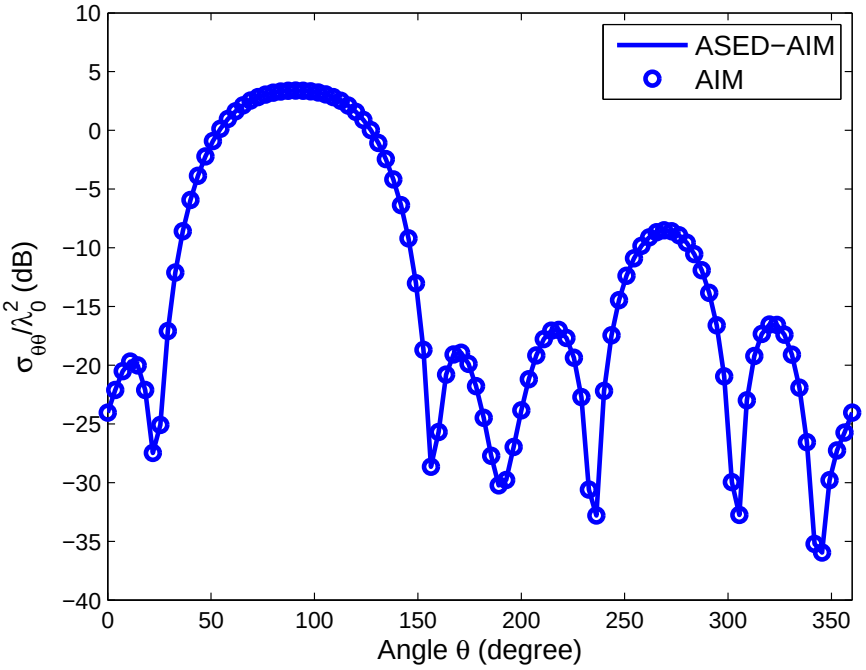

Figure 5.6: Bistatic RCS of the 4×4 array with each cell shown in Fig. 5.3 ($\theta = 90^o$) with electric field θ-polarized at the grazing incidence. The gap is $0.2\lambda_0$ in both x- and y-directions. The results are computed using the AIM (circle line) and the ASED-AIM (solid line).

time of 302 seconds when the conventional AIM is utilized. The number of unknowns for the 8×8 array is 68,992 and it requires memory of 169 MB and computational time of 55 seconds when the ASED-AIM is applied, while it needs memory of 1200 MB and computational time of 753 seconds when the AIM is utilized. The number of unknowns for the 10×10 array is 107,800 and it requires memory of 170 MB and computational time of 55 seconds when the ASED-AIM is used, while it needs memory of 1874 MB and computational time of 1485 seconds when the AIM is applied. It is now clear that the memory requirement and CPU time are almost the same when the ASED-AIM is applied to solve problems with these different array sizes, but the memory requirement and CPU time increase with the array sizes when the conventional AIM is utilized.

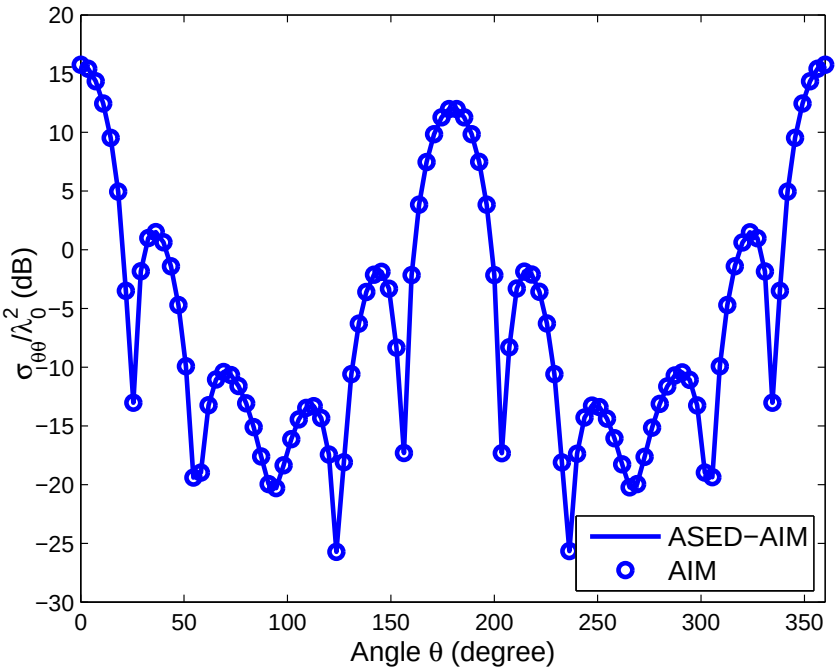

Figure 5.7: Bistatic RCS values of the 6×6 array with each cell shown in Fig. 5.3 with electric field θ-polarized at the normal incidence ($\theta = 0^o$). The gap is $0.2\lambda_0$ in both x- and y-directions. The results are computed using the AIM (circle line) and the ASED-AIM (solid line).

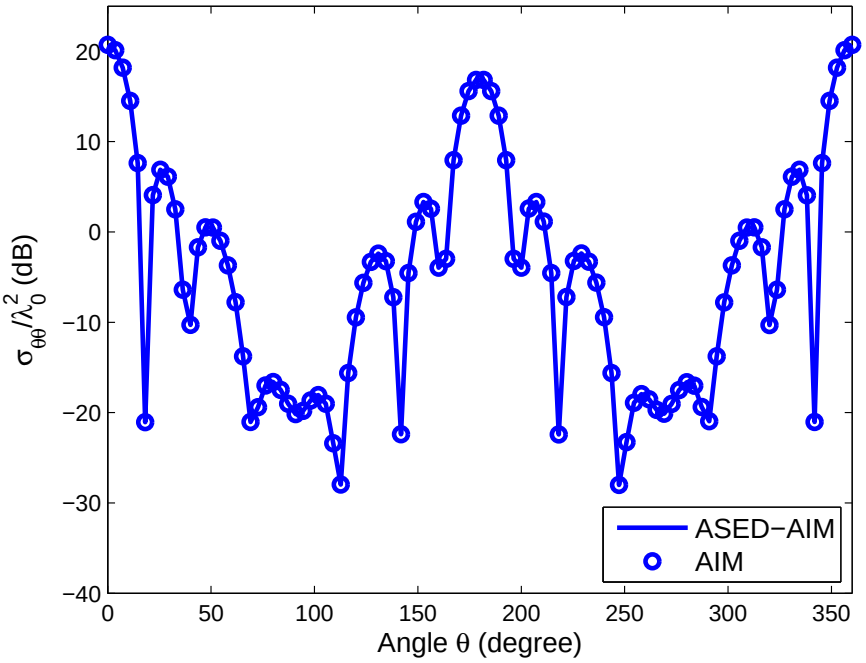

Figure 5.8: Bistatic RCS values of the 8×8 array with each cell shown in Fig. 5.3 with electric field θ-polarized at the normal incidence ($\theta = 0^o$). The gap is $0.2\lambda_0$ in both x- and y-directions. The results are computed using the AIM (circle line) and the ASED-AIM (solid line).

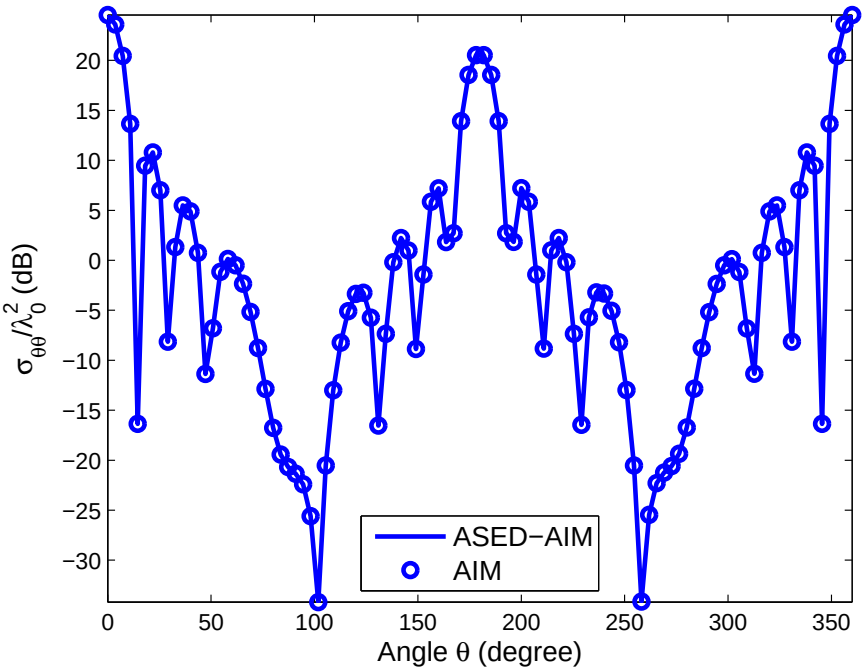

Figure 5.9: Bistatic RCS values of the 10×10 array with each cell shown in Fig. 5.3 with electric field θ-polarized at the normal incidence ($\theta = 0^o$). The gap is $0.2\lambda_0$ in both x- and y-directions. The results are computed using the AIM (circle line) and the ASED-AIM (solid line).

5.3.2 Efficiency for 2D arrays

Subsequently, we investigate the computational complexity and memory requirement of the ASED-AIM and compare them with those of the conventional AIM. Fig. 5.10(a) shows the relationship between the computational time and the number of unknowns using the ASED-AIM and the AIM. Fig. 5.10(b) shows the relationship between the memory and the number of unknowns using the ASED-AIM and the AIM. From Fig. 5.10, it is clear that when the AIM is used, the computational time and the memory requirement are proportional to the number of unknowns. When the number of unknowns reaches 10^5, the memory requirement is over 10^3 MB and CPU time is over 10^3 seconds. When the ASED-AIM is used, the computational time and the memory requirement are much less than those when the conventional AIM is used. Even when the number of un-

knowns reaches 10 million, the memory requirement for ASED-AIM is still less than 10^3 MB and CPU time is less than 10^3 seconds. Especially, they are nearly the same when the number of unknowns is less than 10^6. When the number of unknowns goes up beyond 10^6, the memory requirement and the CPU time become proportional to the number of unknowns. This observation agrees well with the previous complexity analysis in literature. Since the memory requirement is $O(M) + O(N)$, the computational time is $O(M \log M) + O(N \log N)$. When M is small as compared to N, N determines the memory requirement and computational time. It means that most of CPU time and memory have been spent on the first stage of the ASED-AIM. From our results, 168-MB memory and 50-second computational time have been used in the first stage. When number of unknowns is smaller than 10^6, only several MB of memory and a few seconds of computational time have been used in the second stage. When the number of unknowns is larger than 10^6, effect of M becomes dominant. The memory requirement and CPU time both increase linearly with N.

5.3.3 Results for 3D Arrays

The above method can also be extended to analyze 3D finite periodic structures. In this case, a smaller sub-domain of 27 cells is first considered. Then, the entire domain of 27 types of cell basis functions is analyzed by extending the above algorithm. In Fig. 5.11(a), the RCS values calculated using the ASED-AIM and the AIM are compared for the $4 \times 4 \times 4$ array shown in Fig. 5.3, where the dimensions between each cell in x-, y-, and z-directions are all 0.2λ. The array is illuminated at normal incidence by a plane wave with electric field θ-polarized. From Fig. 5.11(a), it is clear that RCS results using ASED-AIM and AIM are in a good agreement. For the $4 \times 4 \times 4$ array problem, the ASED-AIM code requires 68,992 un-

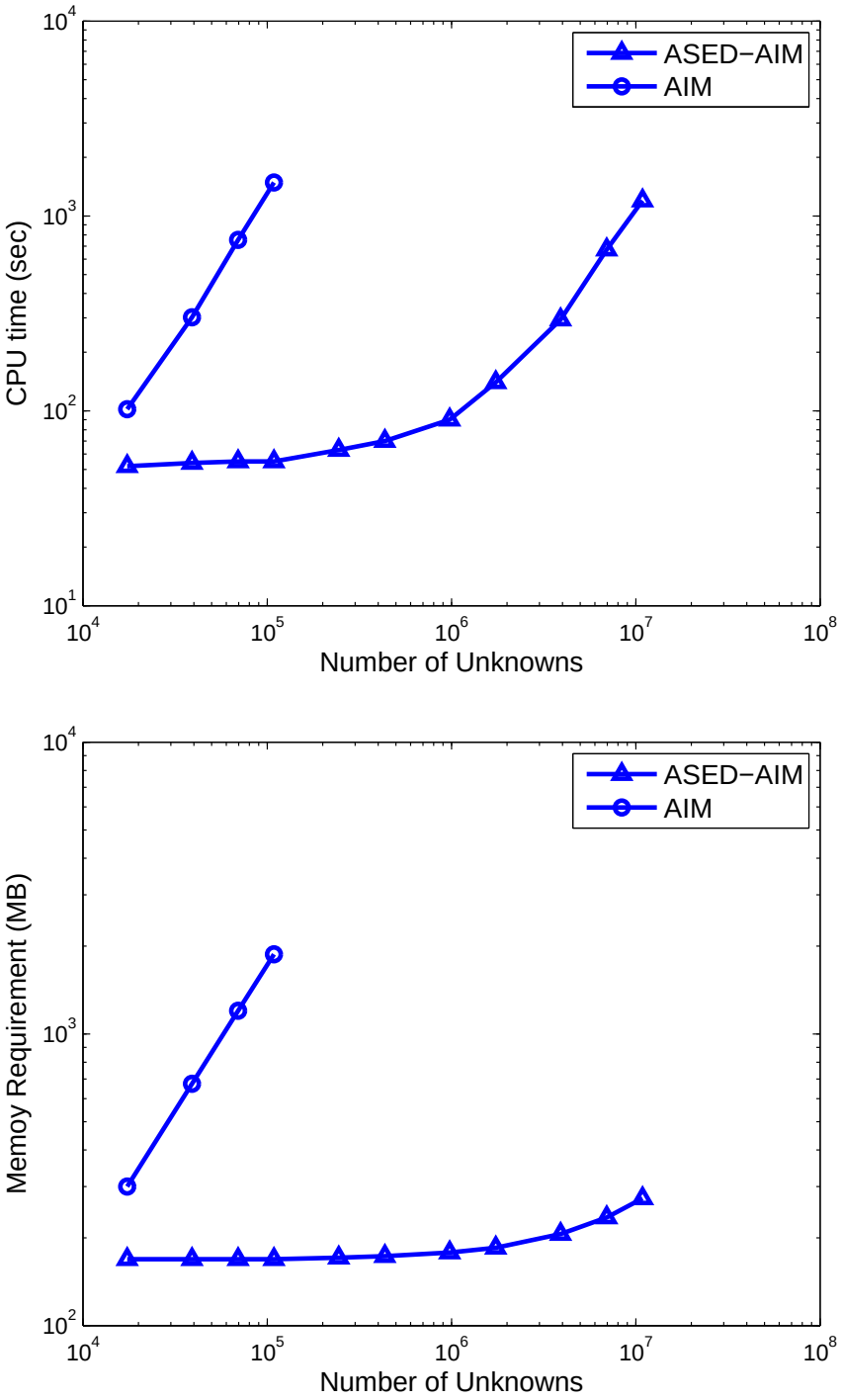

Figure 5.10: The relationship between (a) computational time (b) memory requirement and the number of unknowns within the ASED-AIM (triangle line) and the AIM (circle line).

knowns, 507-MB memory and 178-second computational time, while the AIM code needs 1200-MB memory and 753-second computational time. A $10 \times 10 \times 10$ array problem was also considered, where the number of unknowns is over 1 million. It takes the ASED-AIM code 516 MB in memory and 229 seconds in CPU time to calculate the RCS results shown in Fig. 5.11(b). Compared with those required computational expenses used in the $4 \times 4 \times 4$ array problem, the memory requirement and CPU time used for the $10 \times 10 \times 10$ array problem increase only slightly from 507 MB to 516 MB and from 178 seconds to 229 seconds, respectively; while the number of unknowns increases from 68,992 to over a million. The 3D situation is very similar to the 2D situation, which demonstrates that the ASED-AIM is also very efficient in solving electrically-large 3D periodic structures.

5.3.4 Solving 100×100 Array using ASED-AIM

Finally, we consider an electrically very large finite periodic structure with 100×100 array similar to Fig. 5.3(b). The structure is illuminated by plane wave with $\theta = 0^o$ and $\phi = 0^o$, electric field is θ-polarized. The total number of unknowns in this example is 10.87 million. The calculated radar cross section is shown in Fig. 5.12. For such an electrically large structure with over 10 million unknowns, the ASED-AIM only requires 273 MB memory and 1200 seconds, which demonstrates the efficiency of the new method in solving problems of electromagnetic scattering by large-scale periodic structures.

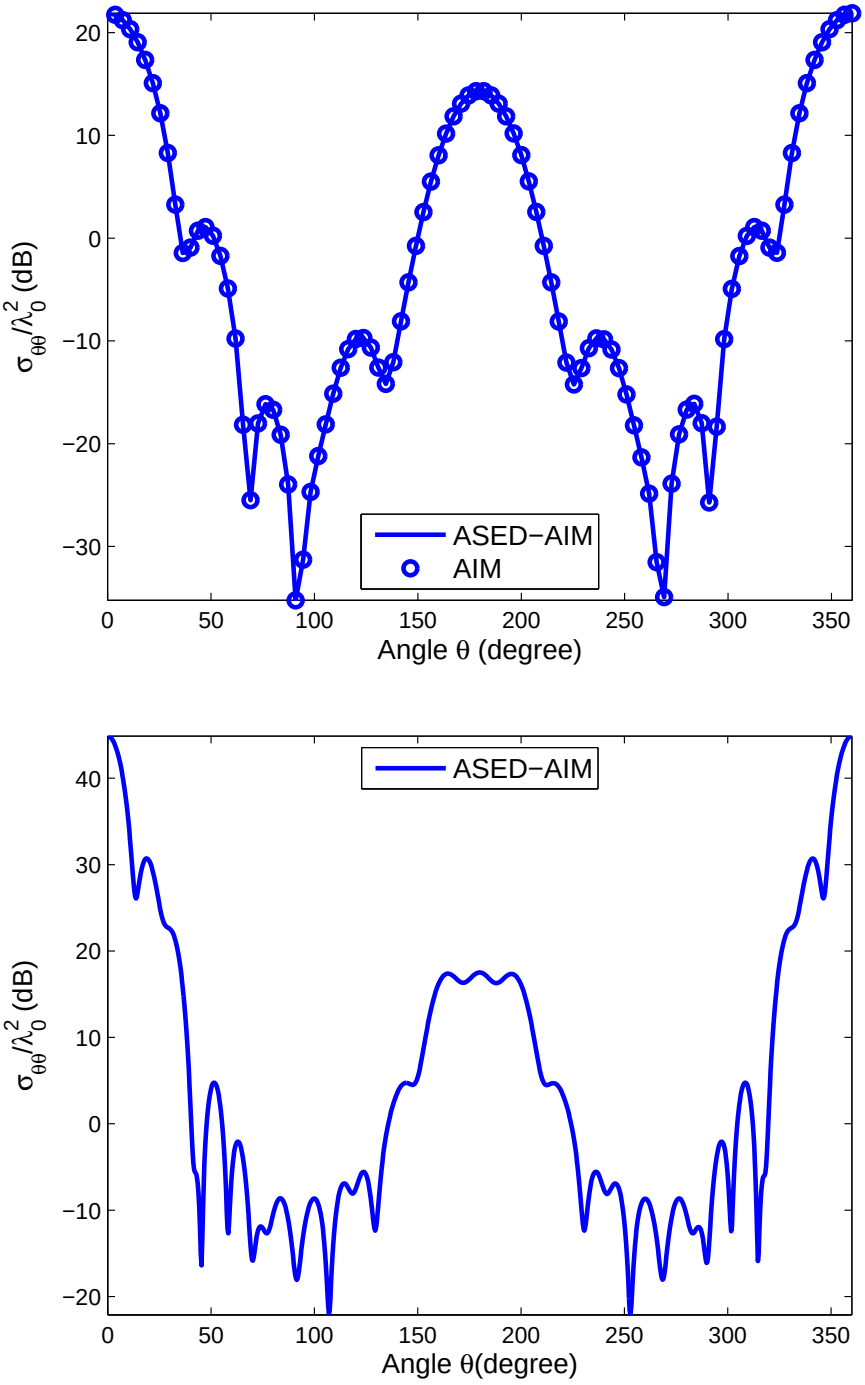

Figure 5.11: Bistatic RCS values of the (a) $4\times4\times4$ array and (b) $10\times10\times10$ array with each cell shown in Fig. 5.3 with electric field θ-polarized at the normal incidence ($\theta = 0^o$). The gap is 0.2λ in the x-, y- and z-directions. The results are computed using the AIM (circle line) and the ASED-AIM (solid line).

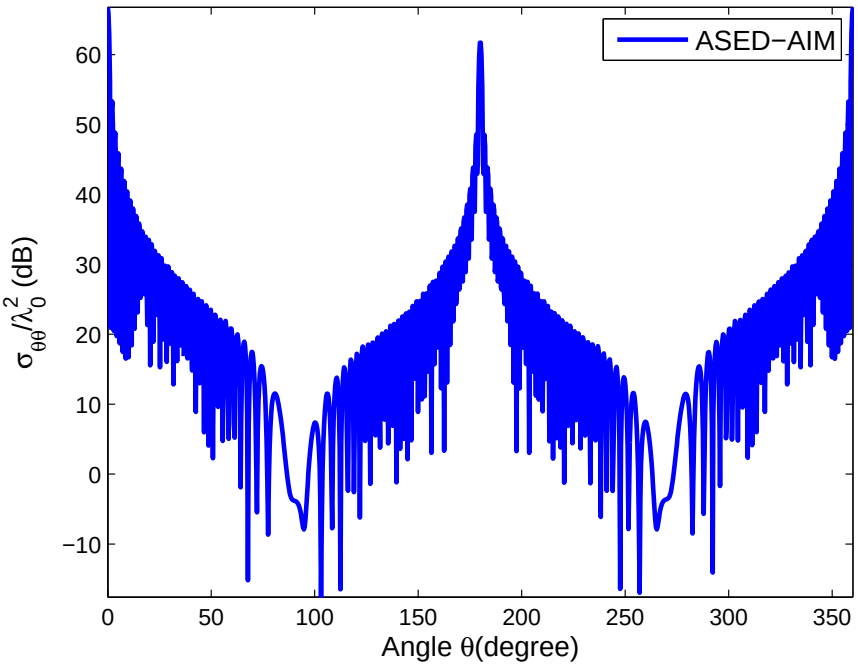

Figure 5.12: Bistatic RCS of the 100×100 array with each cell shown in Fig. 5.3 with electric field θ-polarized at the normal incidence ($\theta = 0^o$). The gap is $0.2\lambda_0$ in all the x-, y-, and z-directions. The result is computed using the ASED-AIM.

Chapter 6

Scattering by Finite Periodic Structures Using CBFM/AIM

In this chapter, we introduce a novel technique that combines the AIM algorithm with the CBFM to solve the problem of electromagnetic scattering by large but finite periodic arrays. An important advantage of using the CBFM for this problem is that we only need to analyze a single unit cell to construct the CBFs for the entire array. The CBFs are generated by illuminating the unit cell with a plane wave incident from different angles, for both the θ- and ϕ- polarizations. The initial set of CBFs, generated in the manner described above, are then downselected by applying a SVD procedure and retaining only the left singular vectors whose corresponding singular values fall above a threshold. Next, in the conventional CBFM, we derive a reduced matrix by applying the Galerkin procedure and solve it directly if its size is manageable. However, when solving an array problem, which precludes the direct-solution option, we can utilize the AIM algorithm, detailed below, not only to accelerate the solution but to reduce memory requirements as well. Numerical examples are included in this chapter to demonstrate the accuracy and the numerical efficiency of the

proposed technique.

6.1 CBFM/AIM Algorithm

Although the CBFM/AIM algorithm is quite general, and useful for treating either metallic or dielectric objects, here we only consider a periodic array of dielectric objects whose treatment is more involved than if the elements were just PEC. For dielectric objects, we can use the volume integral equation formulation, and we begin by imposing the condition:

$$\boldsymbol{E}^{\text{inc}}(\boldsymbol{r}) = \boldsymbol{E}(\boldsymbol{r}) - \boldsymbol{E}^{\text{sca}}(\boldsymbol{r}), \quad \boldsymbol{r} \in V \tag{6.1}$$

where $\boldsymbol{E}^{\text{inc}}(\boldsymbol{r})$, $\boldsymbol{E}^{\text{sca}}(\boldsymbol{r})$, and $\boldsymbol{E}(\boldsymbol{r})$ are the incident, scattered and total fields, respectively.The polarization current $\boldsymbol{J}(\boldsymbol{r})$ induced in the dielectric scatterer is related to the total electric field $\boldsymbol{E}(\boldsymbol{r})$ as follows:

$$\boldsymbol{J}(\boldsymbol{r}) = j\omega\kappa\boldsymbol{D}(\boldsymbol{r}) = j\omega(\epsilon - \epsilon_0)\boldsymbol{E}(\boldsymbol{r}), \quad \boldsymbol{r} \in V \tag{6.2}$$

and

$$\boldsymbol{E}^{\text{sca}}(\boldsymbol{r}) = -j\omega\mu_0 \int_V G(\boldsymbol{r}, \boldsymbol{r}')\boldsymbol{J}(\boldsymbol{r}')dV' + \frac{\nabla}{j\omega\epsilon_0} \int_V G(\boldsymbol{r}, \boldsymbol{r}')\nabla' \cdot \boldsymbol{J}(\boldsymbol{r}')dV' \tag{6.3}$$

where $G(\boldsymbol{r}, \boldsymbol{r}')$ denotes the free-space Green's function; μ_0 and ϵ_0 represent the free-space permeability and permittivity, respectively; ϵ is the permittivity in the dielectric object; and $\kappa = (\epsilon - \epsilon_0)/\epsilon$ identifies the contrast ratio of the material of the scatterer and its background medium.

To ensure the continuity of the normal component of the electric flux density inside the dielectric objects, electric flux density $\boldsymbol{D}$ in the p-th cell,

denoted as the displacement vector $\boldsymbol{D}_p$, expanded as

$$\boldsymbol{D}_p = \frac{1}{j\omega} \sum_{m=1}^{N} I_{p_m} \boldsymbol{f}_{p_m} \tag{6.4}$$

and the volume current in the p-th cell can be written as

$$\boldsymbol{J}_p = \sum_{m=1}^{N} I_{p_m} \kappa \boldsymbol{f}_{p_m} \tag{6.5}$$

where $\boldsymbol{f}_{p_m}$ denotes the SWG basis functions associated with the m-th volume basis functions of the p-th cell, N is the number of SWG basis functions, and I_{p_m} are the unknown coefficients. Next, we employ the Galerkin procedure to test the volume integral equation to obtain the matrix equation:

$$\left(\overline{\boldsymbol{Z}}_{pq}\right)\left(\boldsymbol{I}_q\right) = \left(\boldsymbol{V}_p\right). \tag{6.6}$$

The elements of the impedance matrix $\overline{\boldsymbol{Z}}_{pq}$ can be expressed as

$$\begin{aligned} Z_{p_m q_n} = & \frac{1}{j\omega} < \boldsymbol{f}_{p_m}, \frac{1}{\epsilon} \boldsymbol{f}_{q_n} > + j\omega\mu_0 < \boldsymbol{f}_{p_m}, \boldsymbol{A}_{q_n} > \\ & - \frac{1}{j\omega\epsilon_0} < \boldsymbol{f}_{p_m}, \nabla\phi_{q_n} > \end{aligned} \tag{6.7}$$

where

$$\boldsymbol{A}_{q_n} = \int_{V_{q_n}} G(\kappa \boldsymbol{f}_{q_n}) dV' \tag{6.8}$$

$$\phi_{q_n} = \int_{V_{q_n}} G \nabla' \cdot (\kappa \boldsymbol{f}_{q_n}) dV'. \tag{6.9}$$

For an array with M unit cells and N basis functions are associated with each of these cells, the dimension of the linear equation MN can be large, which may prevent a direct solution of the equation since the memory requirement and the CPU time estimates are $O[(MN)^2]$ and $O[(MN)^3]$, respectively. To circumvent this problem, we employ macro-basis functions, such as the CBFs, to reduce the number of unknowns. The CBFM

algorithm divides the original geometry into a number of subdomains and then constructs the CBFs for each of these subdomains. Since the problem at hand is a truncated periodic array, we can define each cell as a subdomain, enabling us to construct just a single set of the CBFs — a key feature of the CBFM — and subsequently use it for all the cells, solving the scattering problem for arbitrary incident angles.

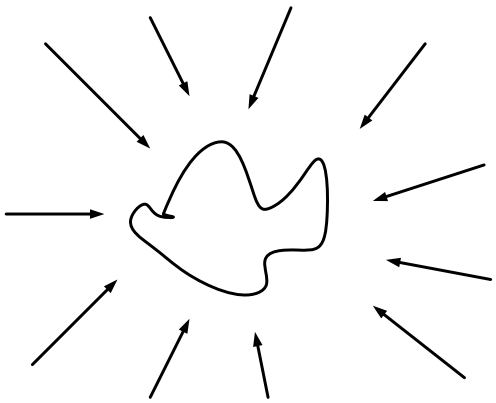

Figure 6.1: CBFs are obtained through currents induced in one unit cell under N_{PWS} plane waves.

To construct such universal CBFs, we illuminate the unit cell with plane waves, incident from N_{PWS} angles (see Fig. 6.1), and consider both vertical and horizontal polarizations. The number N_{PWS} should be sufficiently large to ensure that the current distribution induced on the scatterer for an arbitrary incident angle and polarization can always be expressed as a linear combination of the N_{PWS} CBFs. Typically, the set of CBFs are over-determined, and we perform SVD in order to remove the redundancy and improve the conditioning number of the reduced matrix, which we would generate later by using the CBFs. Fig. 6.2 shows the typical normalized singular value distribution versus the index of singular values for a spherical scatterer, whose dimensions are given in the numerical result section. Based on previous experience, we choose the threshold value for the normalized singular value to be 10^{-3}. Let us denote K as the index

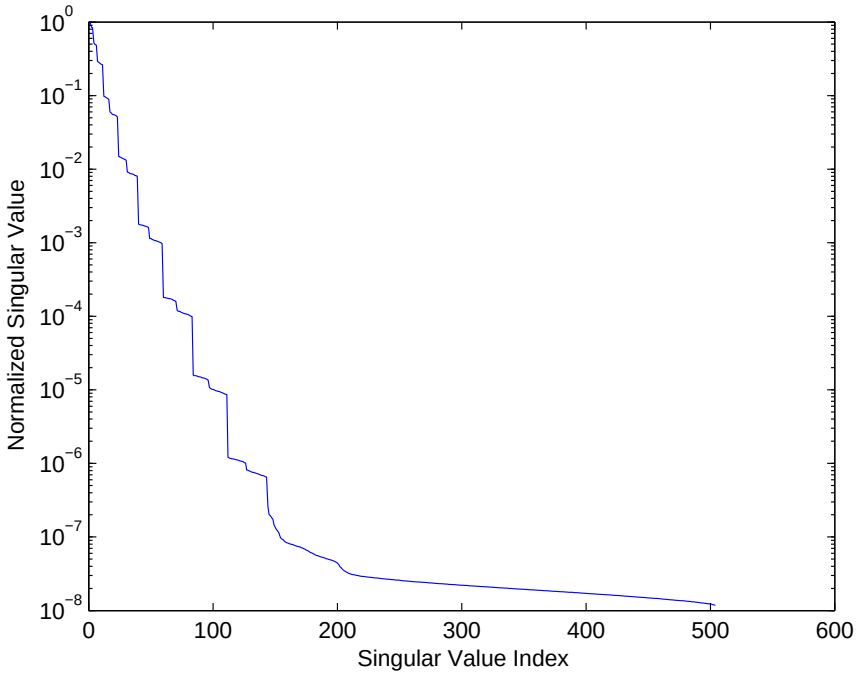

Figure 6.2: Typical normalized singular value as a function of singular value index.

above which the normalized singular value falls below 10^{-3}. We construct the CBFs by solving the matrix equation:

$$\overline{\boldsymbol{Z}} \cdot \overline{\boldsymbol{I}}_{\mathrm{PWS}} = \overline{\boldsymbol{V}}_{\mathrm{PWS}} \tag{6.10}$$

where $\overline{\boldsymbol{Z}}$ denotes impedance matrix for a unit cell, and $\overline{\boldsymbol{V}}_{\mathrm{PWS}}$ denotes the N_{PWS} plane wave excitations. Next, we use the SVD to express the set of solutions $\overline{\boldsymbol{I}}_{\mathrm{PWS}}$ as

$$\overline{\boldsymbol{I}}_{\mathrm{PWS}} = \overline{\boldsymbol{U}}\ \overline{\boldsymbol{S}}\ \overline{\boldsymbol{V}}^{H} \tag{6.11}$$

and we retain the K columns from the left singular value matrix $\overline{\boldsymbol{U}}$ whose singular values are above the threshold. As mentioned earlier, this process not only removes the redundancy from the original solution, but serves to improve the condition number of the reduced matrix as well.

For the p-th cell, the current can be written as $\boldsymbol{J_p} = \overline{\boldsymbol{I}} \cdot \boldsymbol{\alpha}_p$ where $\boldsymbol{\alpha}_p = (\alpha_p^1, \ldots, \alpha_p^K)^T$ are unknowns to be determined by solving the reduced

$$\begin{pmatrix} \overline{\boldsymbol{Z}}^C_{11} & \overline{\boldsymbol{Z}}^C_{12} & \cdots & \overline{\boldsymbol{Z}}^C_{1M} \\ \overline{\boldsymbol{Z}}^C_{21} & \overline{\boldsymbol{Z}}^C_{22} & \cdots & \overline{\boldsymbol{Z}}^C_{2M} \\ \vdots & \vdots & \ddots & \vdots \\ \overline{\boldsymbol{Z}}^C_{M1} & \overline{\boldsymbol{Z}}^C_{M2} & \cdots & \overline{\boldsymbol{Z}}^C_{MM} \end{pmatrix} \cdot \begin{pmatrix} \boldsymbol{\alpha}_1 \\ \boldsymbol{\alpha}_2 \\ \vdots \\ \boldsymbol{\alpha}_M \end{pmatrix} = \begin{pmatrix} \overline{\boldsymbol{I}}^T \boldsymbol{V}_1 \\ \overline{\boldsymbol{I}}^T \boldsymbol{V}_2 \\ \vdots \\ \overline{\boldsymbol{I}}^T \boldsymbol{V}_M \end{pmatrix} \tag{6.13}$$

matrix equations. The cell impedance matrix elements (denoted by the superscript C) can be written as

$$\overline{\boldsymbol{Z}}^C_{pq} = \overline{\boldsymbol{I}}^T \, \overline{\boldsymbol{Z}}_{pq} \overline{\boldsymbol{I}}. \tag{6.12}$$

Thus, the reduced matrix equations can be written as Eqn. (6.13). When KM is large, the matrix equation may not lend itself to a direct solution since the memory requirement and computational complexity are $O((KM)^2)$ and $O((KM)^3)$, respectively. However, we can use a fast iterative solver, such as the AIM, to reduce the memory requirement as well as the CPU time.

The underlying concept in the AIM algorithm is to compute the near-zone interaction directly, and approximate the far zone interactions by using the FFT. Since the number of near-zone interactions is small, and the FFT operation is very efficient, both the memory, and the computational time can be significantly reduced. The AIM algorithm can take advantage of the translational invariance of the Green's function, whether it be free-space or multilayer type. Using the conventional AIM, the matrix vector multiplication can be given by

$$\overline{\boldsymbol{Z}}\boldsymbol{X} = \overline{\boldsymbol{W}} \, \overline{\boldsymbol{H}} \, \overline{\boldsymbol{P}} \, \boldsymbol{X} + \overline{\boldsymbol{Z}}^{\text{near}} \boldsymbol{X} \tag{6.14}$$

where $\overline{\boldsymbol{W}}$ is the interpolation matrix, $\overline{\boldsymbol{H}}$ is the Green's function matrix, $\overline{\boldsymbol{P}}$ is the projection matrix, and $\overline{\boldsymbol{Z}}^{\text{near}}$ is the near-zone correction matrix. For the far zone interaction, the block impedance matrix between p-th and

q-th cell can be approximated as

$$\overline{\boldsymbol{Z}}_{pq} \approx \overline{\boldsymbol{Z}}_{pq}^{\text{far}} = \overline{\boldsymbol{W}}_p \overline{\boldsymbol{H}}_{pq} \overline{\boldsymbol{P}}_q. \tag{6.15}$$

Thus, for the cell interaction in the far zone, we have

$$\begin{aligned} \overline{\boldsymbol{Z}}_{pq}^{C} &= \overline{\boldsymbol{I}}^T \, \overline{\boldsymbol{Z}}_{pq} \overline{\boldsymbol{I}} \\ &\approx \overline{\boldsymbol{I}}^T \, \overline{\boldsymbol{W}}_p \overline{\boldsymbol{H}}_{pq} \overline{\boldsymbol{P}}_q \overline{\boldsymbol{I}} \\ &= \overline{\boldsymbol{W}}_p^C \overline{\boldsymbol{H}}_{pq} \overline{\boldsymbol{P}}_q^C \end{aligned} \tag{6.16}$$

where $\overline{\boldsymbol{W}}_p^C$ and $\overline{\boldsymbol{P}}_q^C$ are the interpolation and projection matrices for the CBFs of p-th and q-th cells, respectively. They can be written explicitly as

$$\overline{\boldsymbol{W}}_p^C = \overline{\boldsymbol{I}}^T \overline{\boldsymbol{W}}_p \tag{6.17}$$

$$\overline{\boldsymbol{P}}_q^C = \overline{\boldsymbol{P}}_q \overline{\boldsymbol{I}}. \tag{6.18}$$

Next, we use the CBFM/AIM to write the matrix vector multiplication, written as

$$\overline{\boldsymbol{Z}}^C \cdot \boldsymbol{X}^C = \overline{\boldsymbol{W}}^C \cdot \overline{\boldsymbol{H}} \cdot \overline{\boldsymbol{P}}^C \cdot \boldsymbol{X}^C + \overline{\boldsymbol{Z}}^{C,\text{near}} \cdot \boldsymbol{X}^C \tag{6.19}$$

whose implementation entails the use of the following four steps:

1. Summing up all the projections from all of the basis functions within each cell;

2. Evaluating the potentials at other grid locations produced by these grid-projected sources by using a 3-D convolution;

3. Interpolating the grid-point potentials onto each cell rather than individual testing functions;

4. Computing the near-field interactions directly for the cells in the immediate vicinity.

6.2 Complexity Analysis for CBFM/AIM Algorithm

In this section, we present a brief analysis of the computational complexity as well as memory requirement of the CBFM/AIM algorithm.

We begin by estimating the computational complexity of the algorithm. In the step to obtain the CBFs, we need to solve Eqn. (6.10). If we were to use a direct solver, the computational time would be $O(N^3)$, where N denotes the number of unknowns in a unit cell. However, the computational time reduces to $O(N \log N)$ if we use the AIM algorithm instead. Next we estimate the computational complexity of the SVD process for obtaining the CBFs. It is known to be $C_1 N N_{\mathrm{PWS}}^2 = O(N)$, where C_1 is a constant and N_{PWS} is the number of plane wave excitations. For the near-zone interactions, the interaction of each CBF in a given cell with each CBF in the neighboring cell needs to be counted. Therefore, the computational cost in each iteration step is approximately $(C_2 K) \cdot (KM) = O(M)$, where C_2 is the number of near-neighbors of a given cell, K is the index above which the normalized singular value falls below the threshold, and M is the number of cells in the entire array. Since there are only M cells, the projection process for all of the cells requires $O(M)$ operations. The computational cost of the FFT process is $O(N_g \log N_g) = O(M \log M)$, where N_g is the number of grids enclosing the computational domain, which is proportional to number of cells M. Similar to the projection process, the interpolation process also needs $O(M)$ operation. Adding these together, the total computational

complexity can be expressed as

$$\begin{aligned}\mathcal{C} &= O(N\log N) + O(N) + O(M) + O(M\log M)\\ &= O(N\log N) + O(M\log M).\end{aligned} \tag{6.20}$$

Next, by following a similar procedure, we can estimate the memory requirement for the new algorithm. The memory required to construct the CBFs is $O(N^2)$ if the entire matrix is stored and $O(N)$ if the AIM is used. The memory requirement for the SVD process is $O(N)$. To compute the near-region interactions between the elements, we need a memory of $O(K^2)$, which is usually negligible. The memory requirements for the projection and interpolation matrices are $O(M)$. The memory requirement of the FFT matrix is $O(N_g)$. Hence, the total storage requirement is estimated to be

$$\begin{aligned}\mathcal{M} &= O(N) + O(N) + O(K^2) + O(M) + O(N_g)\\ &= O(N) + O(M).\end{aligned} \tag{6.21}$$

We note from the above equation that both the computational complexity and the memory requirement are comprised of two parts. The first of these is related to M, the number of cells in the periodic array, while the second is related to N, the number of basis functions in a cell, which can be very large when either the permittivity of the dielectric scatterer or its volume is large or when a cell is comprised of a large number of scatterers. Numerical results will be presented in the next section to validate the above analysis.

6.3 Numerical Results Involving CBFM/AIM

In this section, we present a number of illustrative examples to demonstrate the accuracy and efficiency of the CBFM/AIM algorithm. We employ a GMRES solver for the iteration and terminate the iterative solution process when residual falls below 10^{-3}.

6.3.1 2D-Array Results

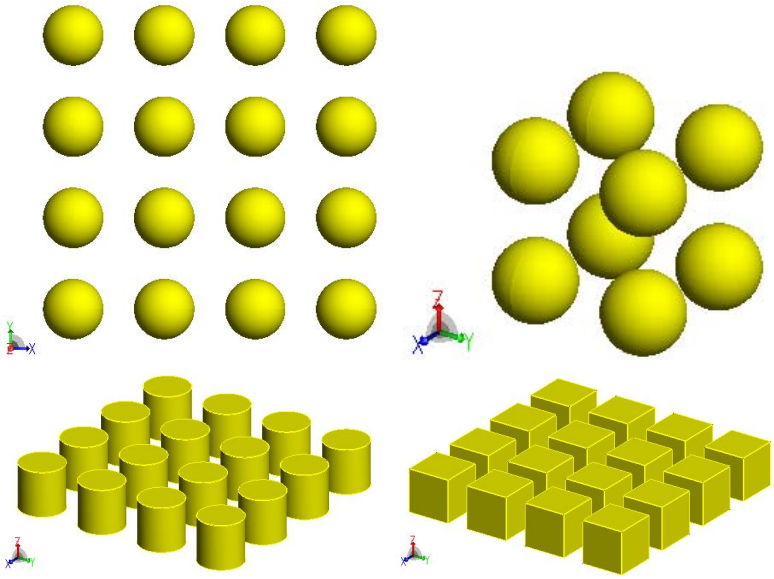

Figure 6.3: Structures used in the examples. (a) A 4×4 sphere array; (b) a $2 \times 2 \times 2$ sphere array; and (c) a 4×4 cylinder array; (d) a 4×4 cube array.

The first example is a 2×2 array located in the x-y plane, and each cell of the array is a sphere with radius $0.2\lambda_0$ and $\epsilon_r = 2$. The periodicity is $0.6\lambda_0$ in both the x- and y-dimensions. We consider the case of a θ-polarized plane wave with an incident angle $\theta^{\text{inc}} = 0^o, \phi^{\text{inc}} = 0^o$. We compare CBFM/AIM result with one from the conventional AIM. Fig. 6.4(a) compares the bistatic RCS, while Figs. 6.4(b) and (c) present a comparison of the magnitudes of the electric fields, calculated at a plane located at a distance of $z = 0.1\lambda$ below the array. An excellent agreement between the

two confirms the accuracy of the CBFM/AIM algorithm for the 2D-array problem in consideration.

In order to demonstrate that the CBFM/AIM is accurate with varying array size, the shape of the unit cell, the constitutive parameters, the incidence of plane wave and the spacing between each cell, we investigated many cases as shown below. For the examples below, we vary one parameter while keep other parameters fixed. By default, the examples are a 4×4 sphere array with other parameters shown in the first example.

In the first case, we considered the effect of the array size to the accuracy of our CBFM/AIM solver. Here, we considered arrays of sizes 3×3 and 4×4. We calculated both far field RCS and the magnitude of electric field in the $z = 0.1\lambda_0$ plane below the array. We compared CBFM/AIM result with one from the conventional AIM. The results are shown in Fig. 6.5 and Fig. 6.6. An excellent agreement between the CBFM/AIM and conventional AIM confirms that the accuracy of the CBFM/AIM algorithm is not affected by the size of the 2D-array problems under consideration.

In the second case, we investigated the effect of the shape of the unit cell on the accuracy of our CBFM/AIM solver. We considered two examples: the first one is a cylinder array shown in Fig. 6.3(c) with the radius of the cylinder $0.2\lambda_0$ and the height $0.4\lambda_0$, the second one is a cube array Fig. 6.3(d) with the dimension $0.4\lambda_0$. We calculated both far field RCS and the magnitude of electric field. For the cylinder array, we calculated the electric field in the $z = 0.2\lambda_0$ plane above the array. For the cube array, we calculated the electric field in the $z = 0.5\lambda_0$ plane below the array. We compared CBFM/AIM result with one from the conventional AIM. The results of the cylinder array are shown in Fig. 6.7. The results of the cube array are shown in Fig. 6.8. An excellent agreement between the CBFM/AIM and conventional AIM confirms that the accuracy of the

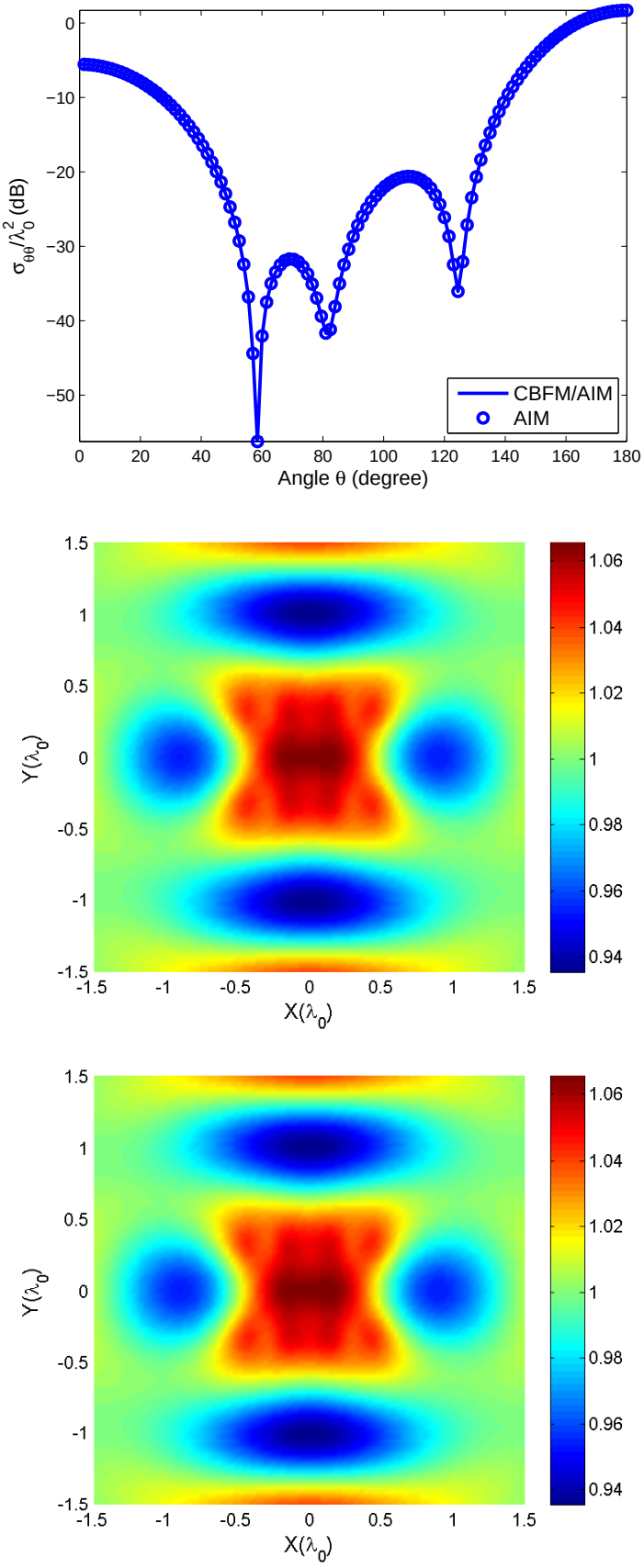

Figure 6.4: Far field RCS and magnitude of electric field calculated for 2×2 sphere array. (a) Bistatic RCS in the x-z plane; (b) electric field calculated by CBFM/AIM; (c) electric field calculated by AIM.

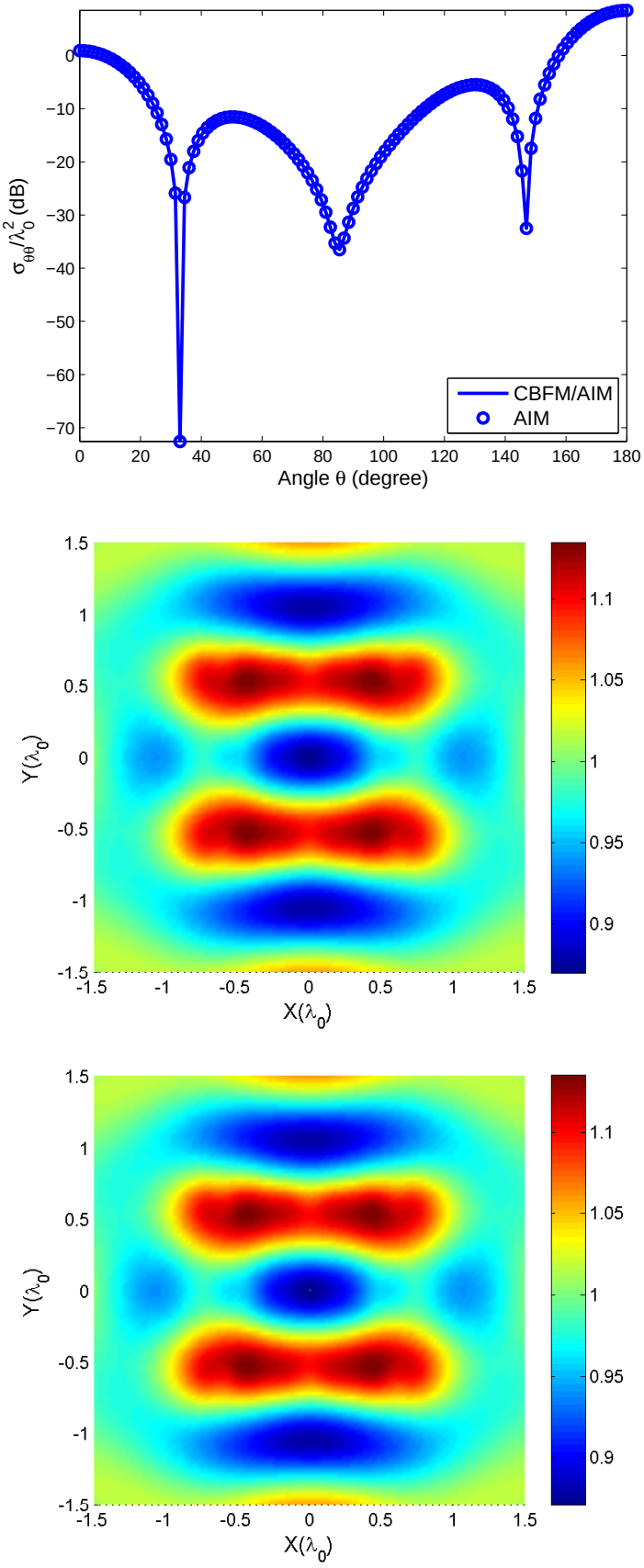

Figure 6.5: Far field RCS and magnitude of electric field calculated for a 3×3 sphere array. (a) Bistatic RCS in the x-z plane; (b) electric field calculated by CBFM/AIM; (c) electric field calculated by AIM.

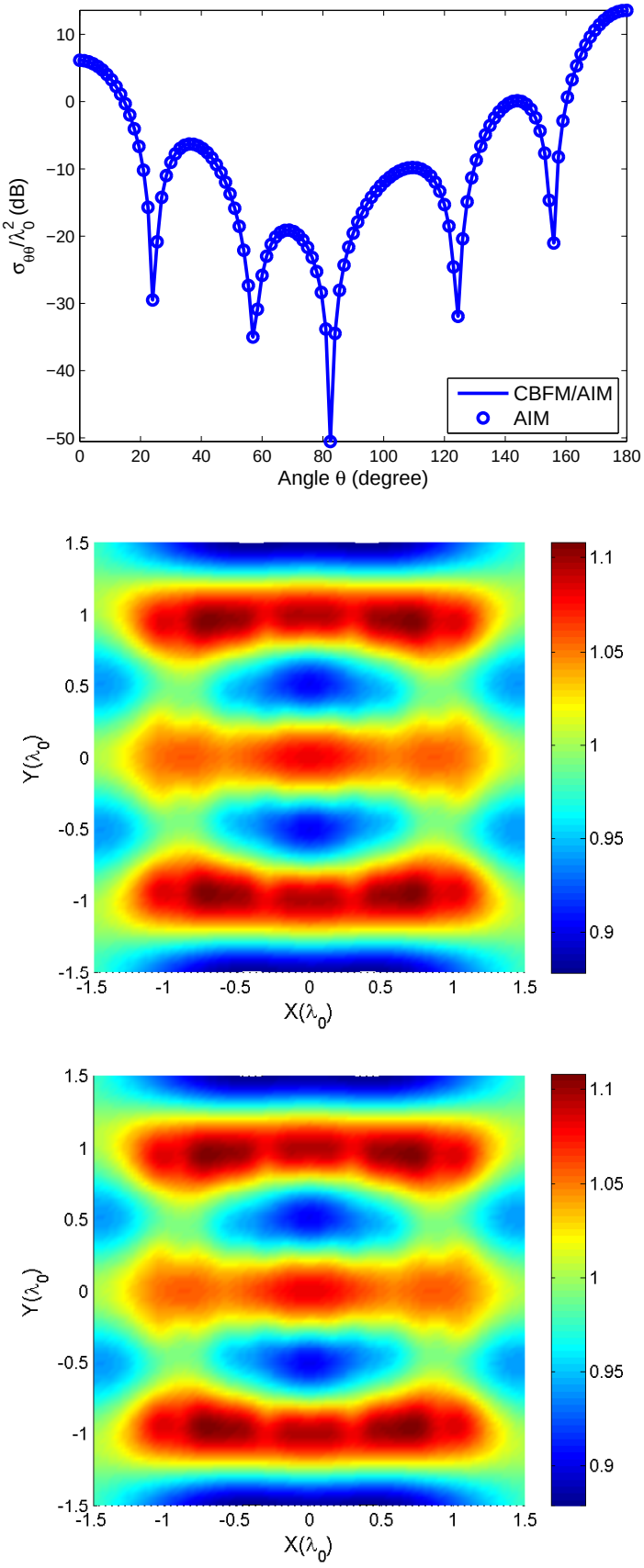

Figure 6.6: Far field RCS and magnitude of electric field calculated for a 4×4 sphere array. (a) Bistatic RCS in the x-z plane; (b) electric field calculated by CBFM/AIM; (c) electric field calculated by AIM.

CBFM/AIM algorithm is robust against the variation of cell shape of the 2D-array problems under consideration.

In the third case, we investigated the effect of spacing between the unit cell on the accuracy of our CBFM/AIM solver. We considered two spacing: $0.1\lambda_0$ and contacting elements. We calculated both far field RCS and the magnitude of electric field in the $z = 0.1\lambda_0$ plane below the array. We compared CBFM/AIM result with one from the conventional AIM. The results of the array with $0.1\lambda_0$ spacing are shown in Fig. 6.9. The results of the array with contacting elements are shown in Fig. 6.10. Excellent agreement between the CBFM/AIM and conventional AIM confirms that the accuracy of the CBFM/AIM algorithm is robust against the variation of spacing of the 2D-array problems in consideration.

In the fourth case, we investigated the effect of the direction of plane wave incidence on the accuracy of our CBFM/AIM solver. We considered two directions: $\theta^i = 135^o$ and $\theta^i = 90^o$ while $\phi^i = 0^o$, the plane waves are θ-polarized. We calculated both far field RCS and the magnitude of electric field in the $z = 0.1\lambda_0$ plane below the array. We compared CBFM/AIM result with one from the conventional AIM. The results of the array with $\theta^i = 135^o$ are shown in Fig. 6.11. The results of the array with $\theta^i = 90^o$ are shown in Fig. 6.12. An excellent agreement between the CBFM/AIM and conventional AIM confirms that the accuracy of the CBFM/AIM algorithm is robust against the variation of the direction of plane wave incidence.

In the last case, we investigated the effect of the constitutive parameters of the unit cell on the accuracy of our CBFM/AIM solver. We considered two parameters: $\epsilon_r = 4$ and $\epsilon_r = 6$. We calculated both far field RCS and the magnitude of electric field in the $z = 0.1\lambda_0$ plane below the array. We compared CBFM/AIM result with one from the conventional AIM. The results of the array with $\epsilon_r = 4$ are shown in Fig. 6.13. The results

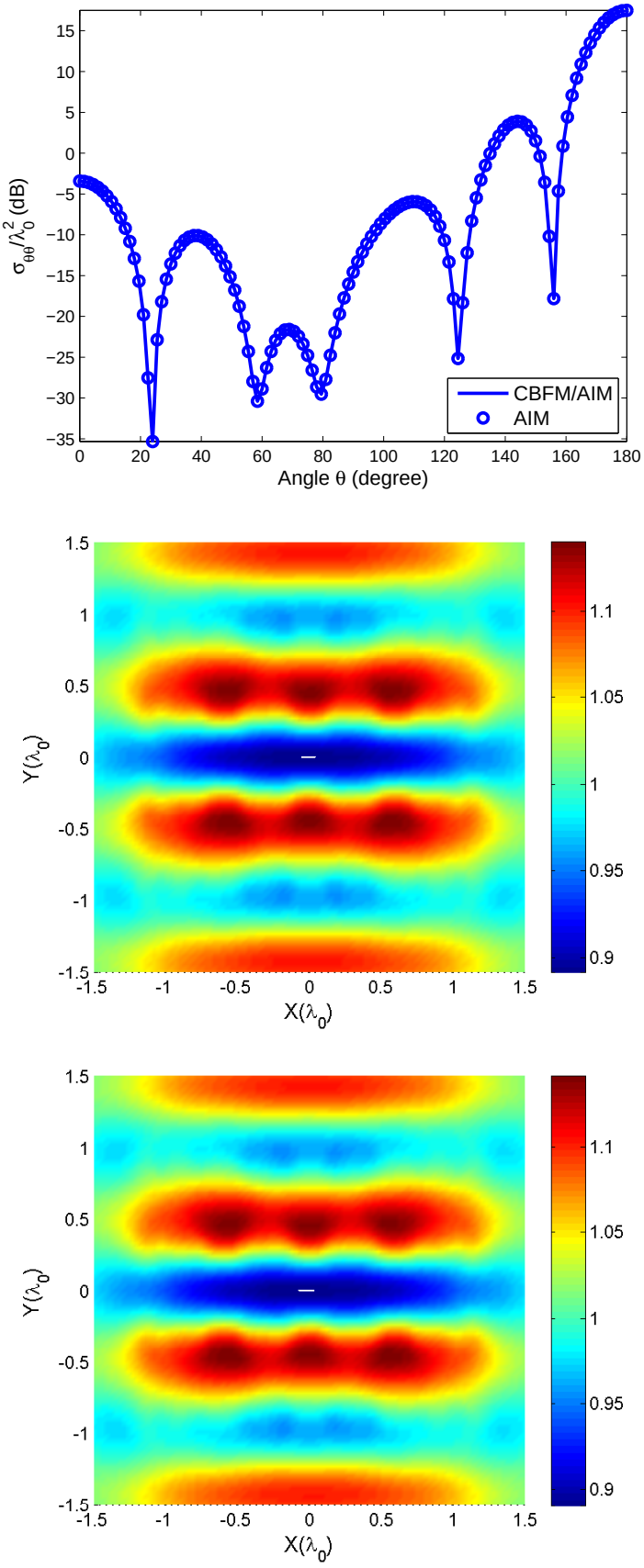

Figure 6.7: Far field RCS and magnitude of electric field calculated for a 4×4 cylinder array. (a) Bistatic RCS in the x-z plane; (b) electric field calculated by CBFM/AIM; (c) electric field calculated by AIM.

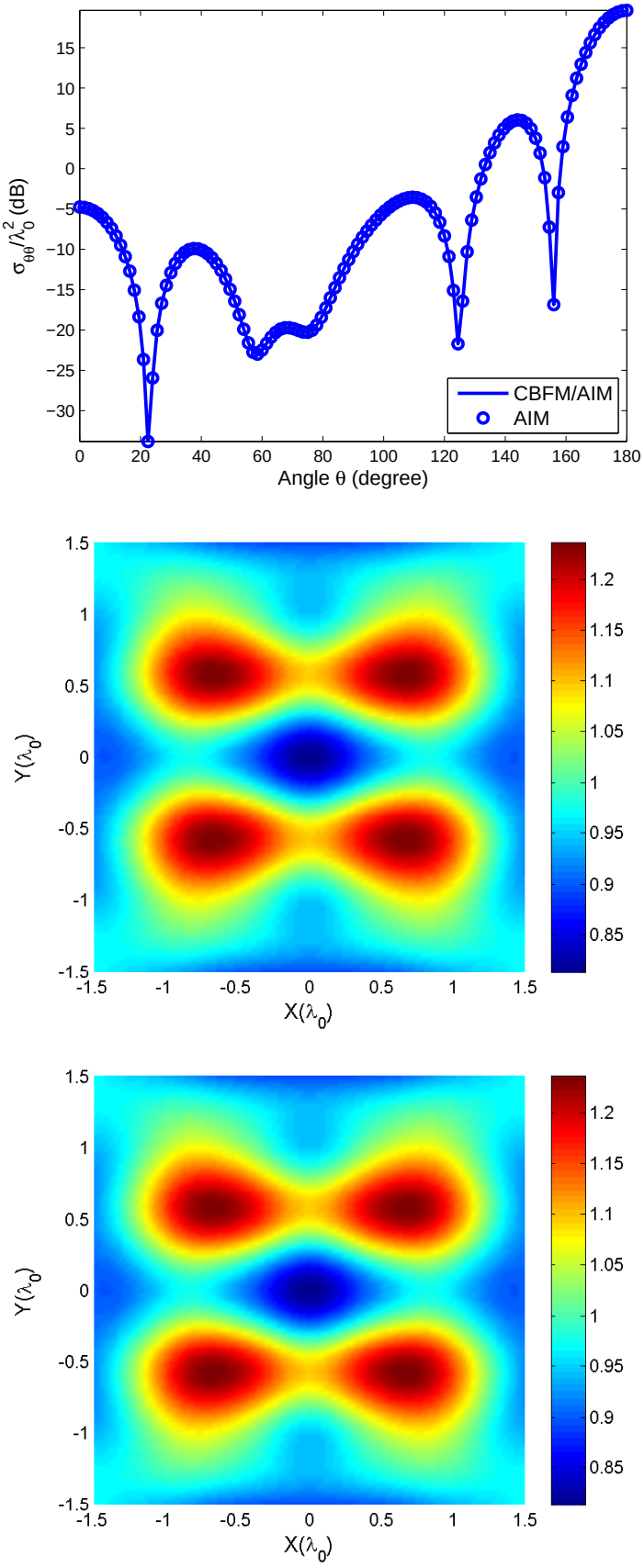

Figure 6.8: Far field RCS and magnitude of electric field calculated for a 4×4 cube array. (a) Bistatic RCS in the x-z plane; (b) electric field calculated by CBFM/AIM; (c) electric field calculated by AIM.

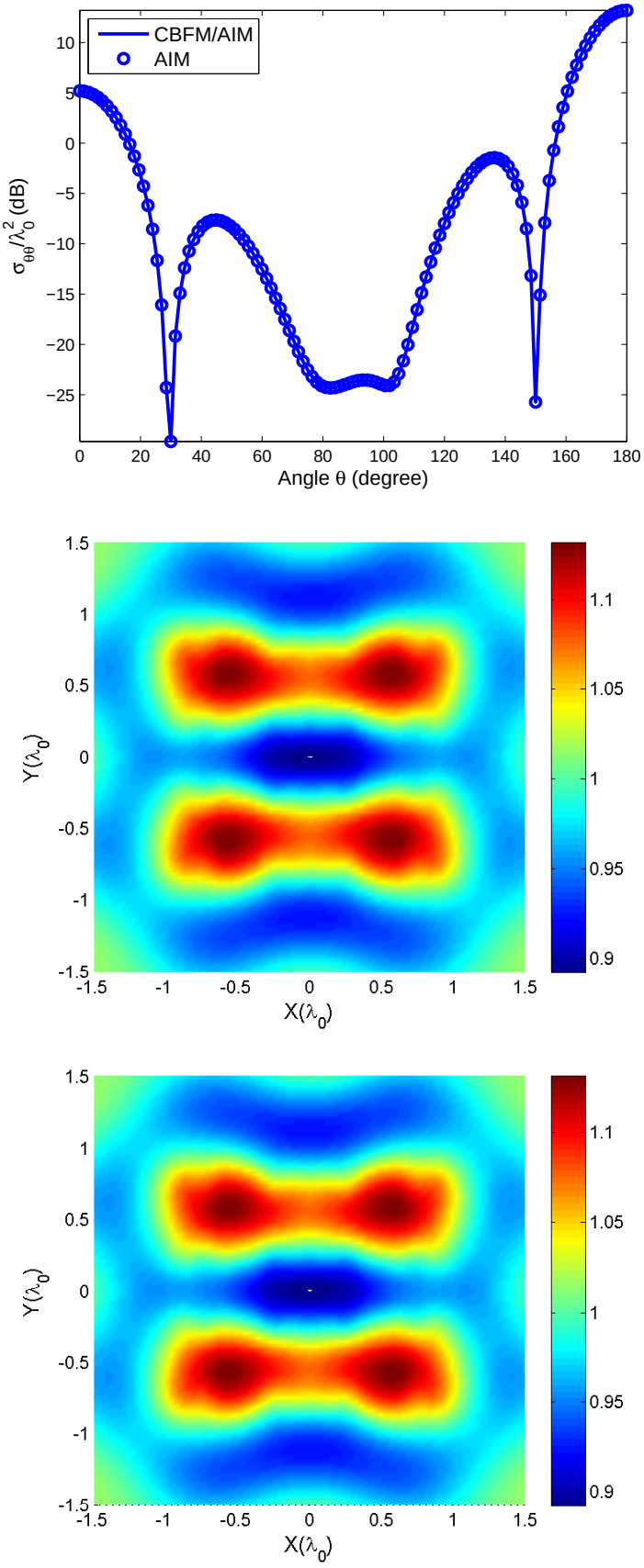

Figure 6.9: Far field RCS and magnitude of electric field calculated for a 4×4 sphere array with $0.1\lambda_0$ spacing between each cell. (a) Bistatic RCS in the x-z plane; (b) electric field calculated by CBFM/AIM; (c) electric field calculated by AIM.

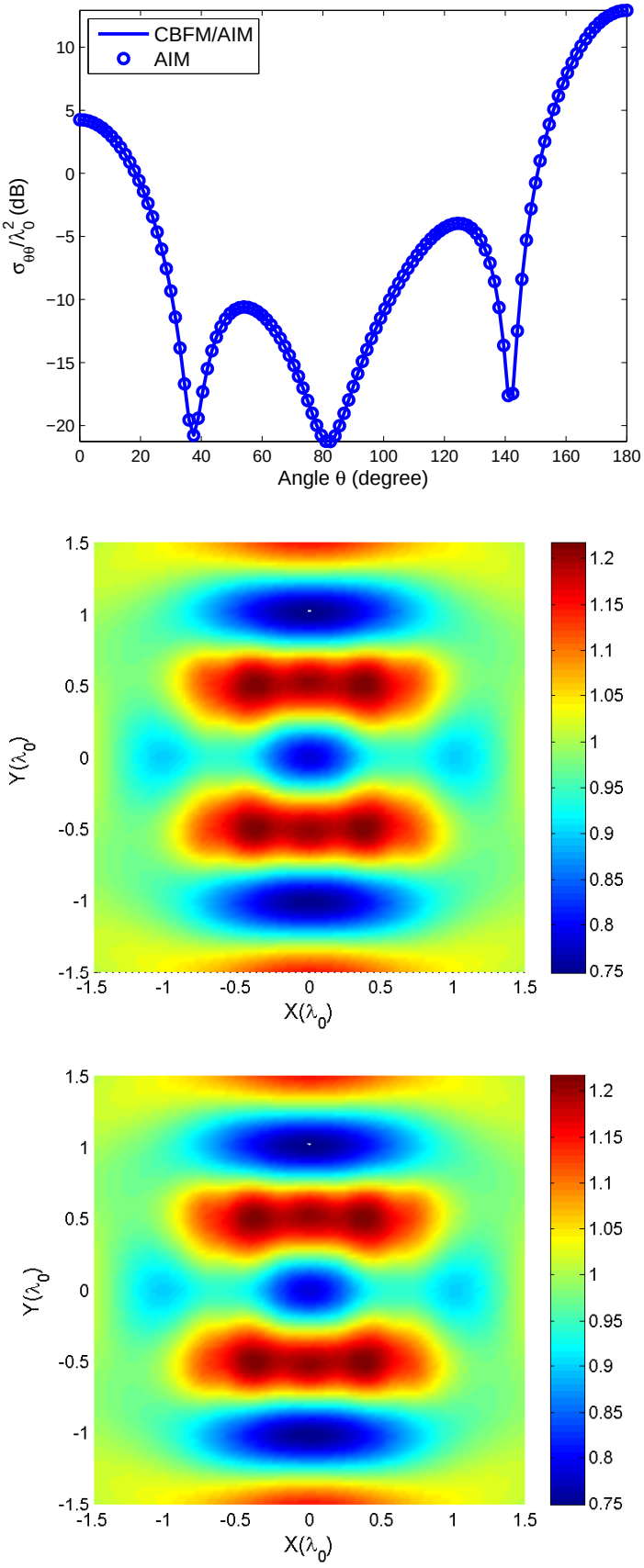

Figure 6.10: Far field RCS and magnitude of electric field calculated for a 4×4 sphere array with contacting elements. (a) Bistatic RCS in the x-z plane; (b) electric field calculated by CBFM/AIM; (c) electric field calculated by AIM.

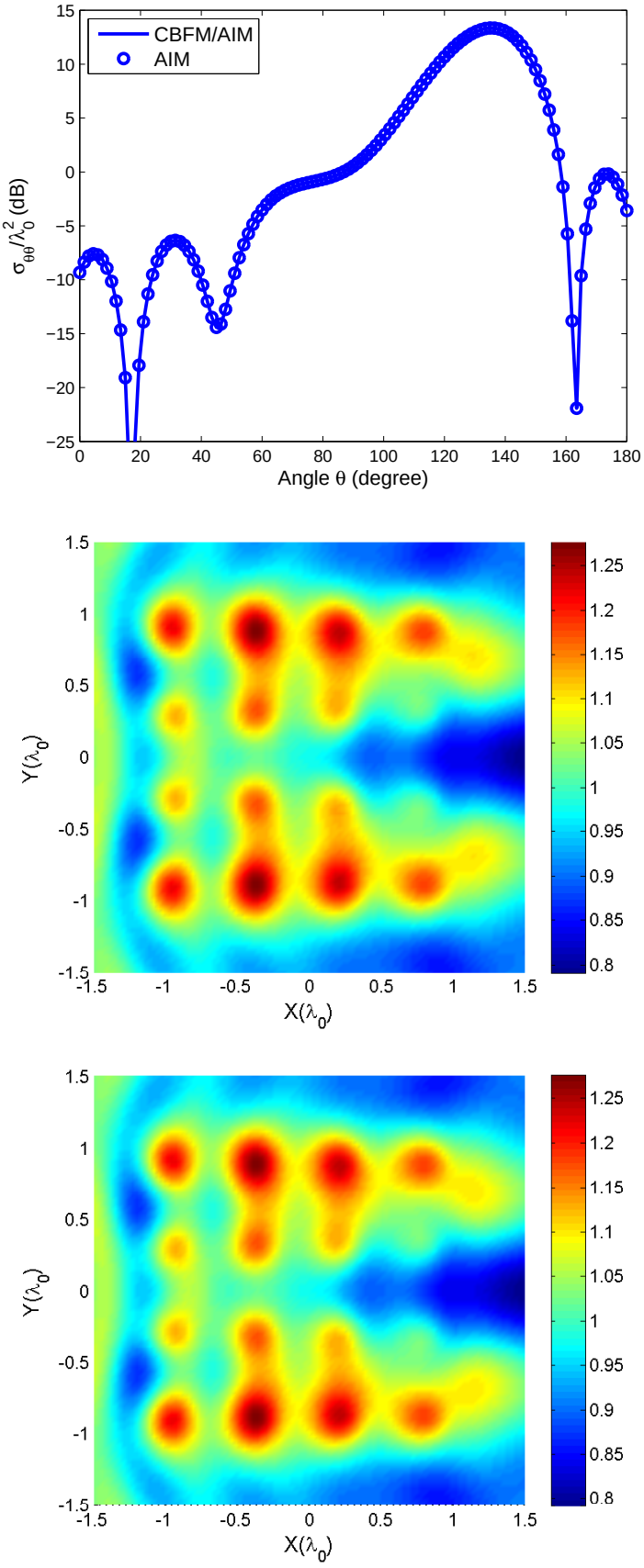

Figure 6.11: Far field RCS and magnitude of electric field calculated for a 4×4 sphere array incident by plane wave with $\theta^i = 135^o$. (a) Bistatic RCS in the x-z plane; (b) electric field calculated by CBFM/AIM; (c) electric field calculated by AIM.

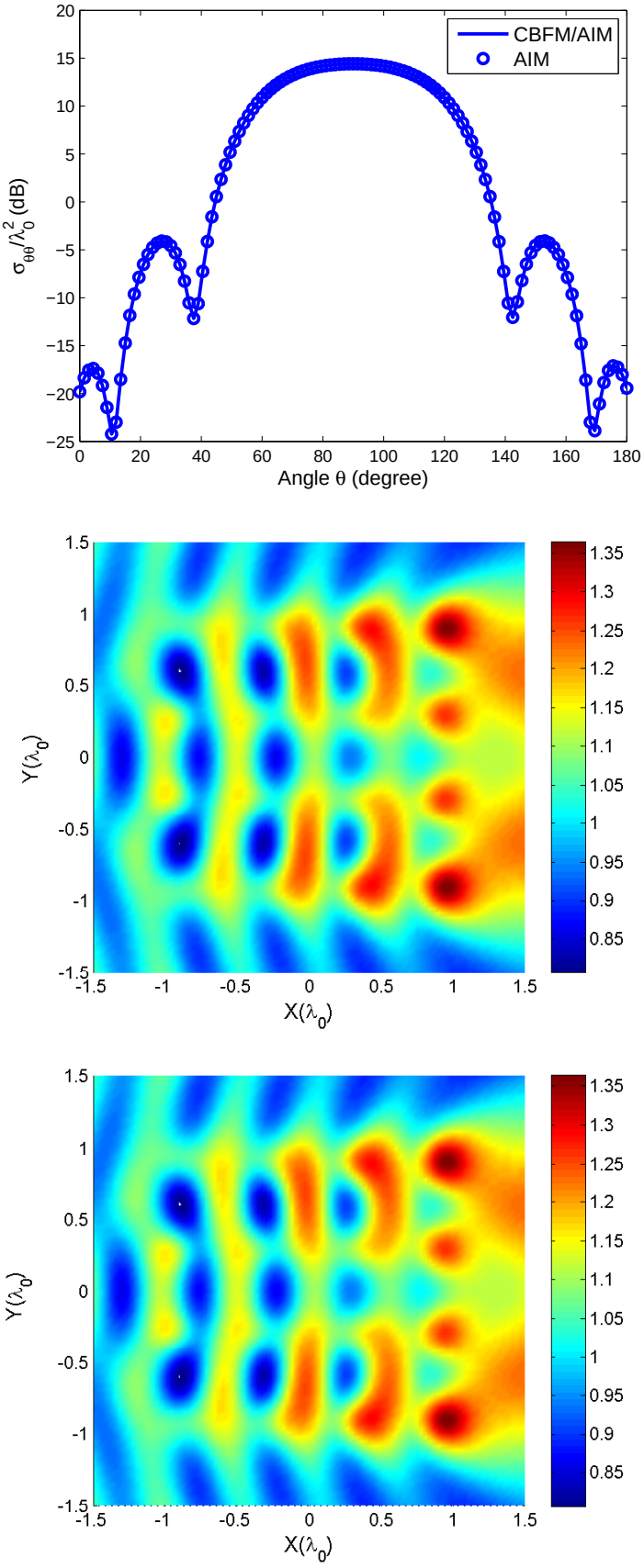

Figure 6.12: Far field RCS and magnitude of electric field calculated for a 4×4 sphere array incident by plane wave with $\theta^i = 90^o$. (a) Bistatic RCS in the x-z plane; (b) electric field calculated by CBFM/AIM; (c) electric field calculated by AIM.

of the array with $\epsilon_r = 6$ are shown in Fig. 6.14. Excellent agreement between the CBFM/AIM and conventional AIM confirms that the accuracy of the CBFM/AIM algorithm is robust against the variation of constitutive parameters of the 2D-array problems in consideration.

6.3.2 Efficiency for 2D-Array Problems

Our next step is to investigate the efficiency of the CBFM/AIM algorithm. Fig. 6.15(a) and Fig. 6.15(b) display the CPU time and memory, respectively, as we progressively increased the number of unknowns. It is evident from the figures that the CBFM/AIM algorithm outperforms conventional AIM, both in memory and computational time. We also note that the memory requirement and computational time remains the same even when the number of unknowns increases up to 10^6. This can be attributed to the overhead involved in the setup process, which includes the evaluation of the generation of the CBFs, the projection, the interpolation operation and the evaluation of the near-zone impedance matrix dominates the entire solution process and, hence, renders the overhead of the setup process to be relatively independent of the size of array. With the increase in the number of unknowns, the matrix-vector multiplication process begins to dominate the solution process, and the overhead of this process becomes proportional to the number of unknowns. The computational statistics of CBFM/AIM for 2D arrays are listed in Table 6.1. It is evident, from this table, that the number of CBFs is much smaller than the number of original unknowns, and the memory requirement is smaller than 1 GB even when the number of unknowns reaches 20 million. The total time required to solve a problem involving over 20 million unknowns problem is around 1 hour.

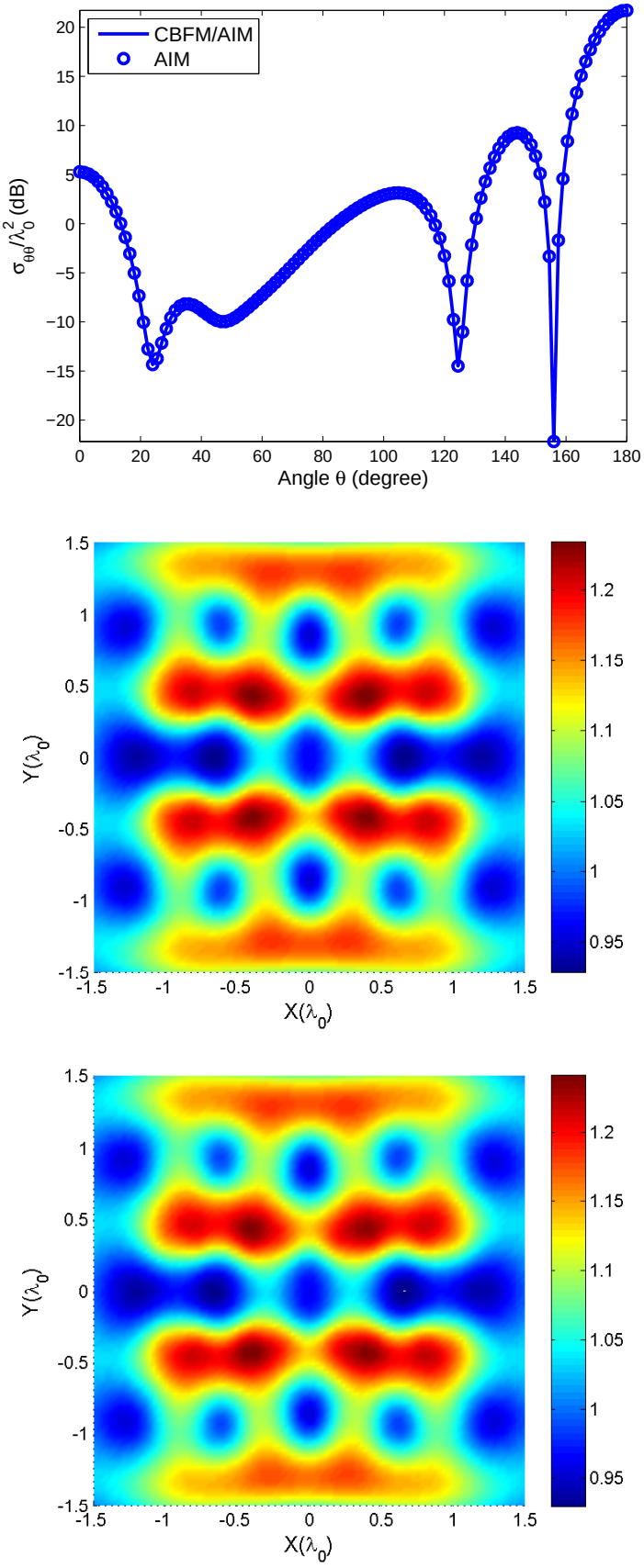

Figure 6.13: Far field RCS and magnitude of electric field calculated for a 4×4 sphere array with $\epsilon_r = 4$. (a) Bistatic RCS in the x-z plane; (b) electric field calculated by CBFM/AIM; (c) electric field calculated by AIM.

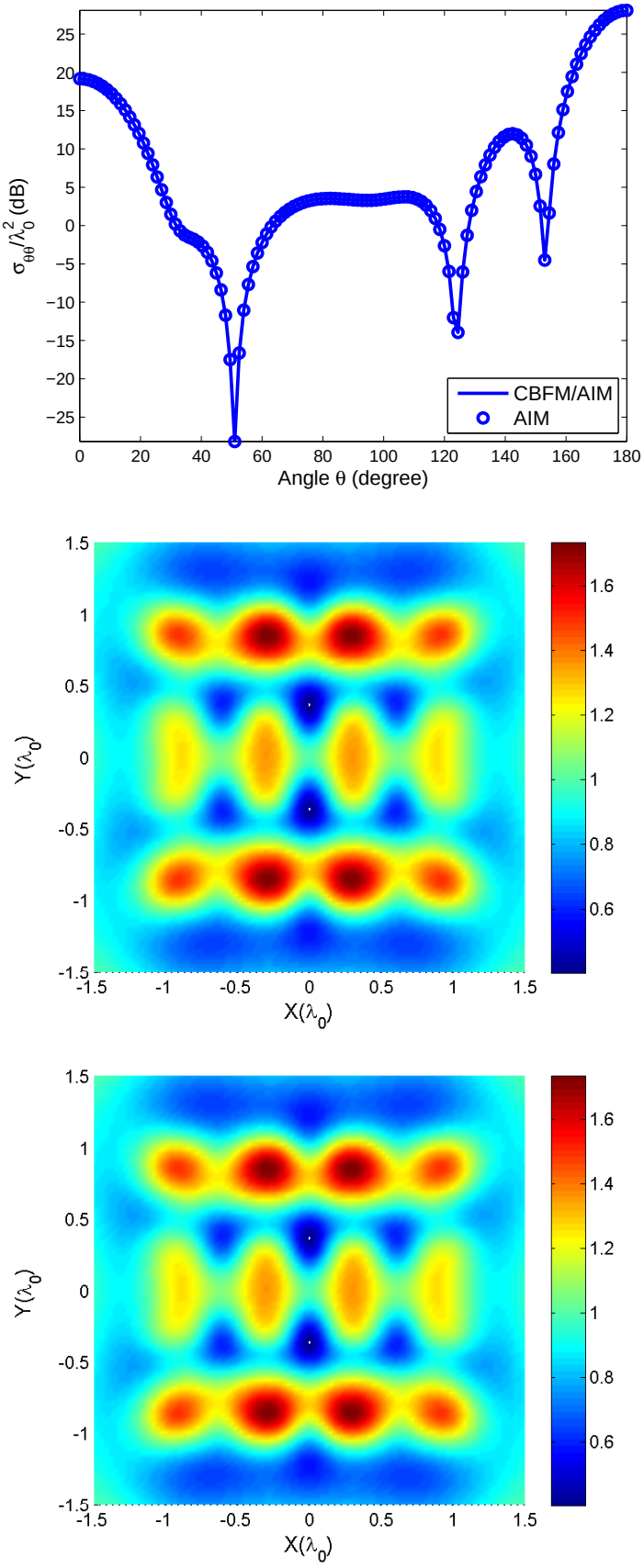

Figure 6.14: Far field RCS and magnitude of electric field calculated for a 4×4 sphere array with $\epsilon_r = 6$. (a) Bistatic RCS in the x-z plane; (b) electric field calculated by CBFM/AIM; (c) electric field calculated by AIM.

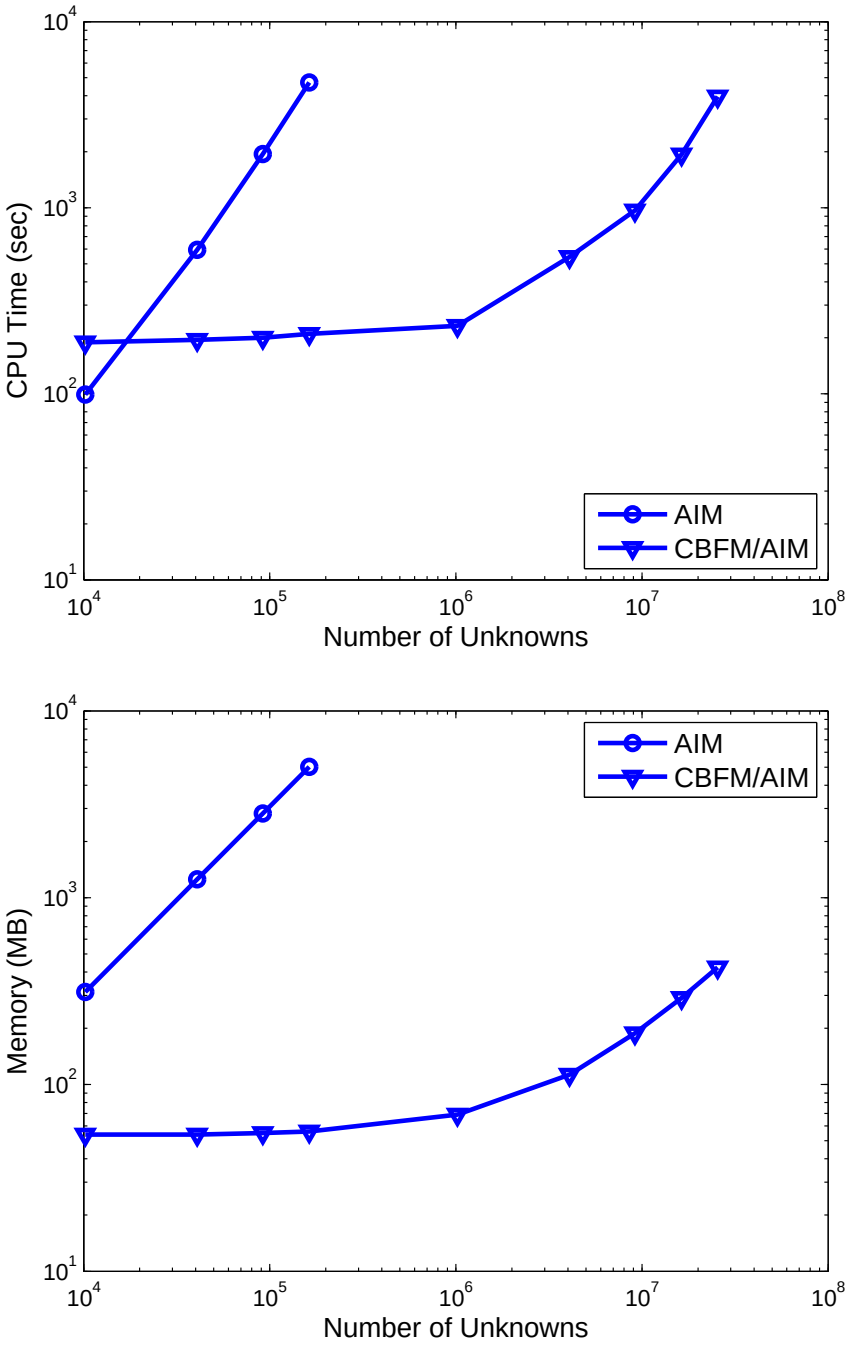

Figure 6.15: Relationship between number of unknowns, (a) computational time and (b) memory requirement for 2D arrays.

Table 6.1: Computational statistics of CBFM/AIM for various 2D arrays simulations

size of array	**total number of unknowns**	**total number of CBFs**	**memory (MB)**	**total time (hh:mm:ss)**
20×20	1.0M	0.02M	69	00:03:52
40×40	4.1M	0.09M	113	00:09:04
60×60	9.2M	0.21M	188	00:16:07
80×80	16.3M	0.38M	291	00:32:13
100×100	25.5M	0.59M	424	01:06:08

6.3.3 3D-Array Cases

Having demonstrated the accuracy and efficiency of the CBFM/AIM algorithm in solving the 2D-array type of scattering problems, we go on to investigate its capability to handle 3D-array problems. Toward this end, we consider an example which analyzes a $2 \times 2 \times 2$ array shown in Fig. 6.3(b). We calculate the RCS as well as the near field behavior for this geometry, and then compare them with the conventional AIM results displayed in Fig. 6.16; an excellent agreement is observed again. Next, we investigate the efficiency of the CBFM/AIM for this example. The computational complexity versus the number of unknowns for the 3-D case are similar to those for the 2-D case, namely that CBFM/AIM is numerically more efficient as well as less burdensome on the memory than the AIM approach alone. Fig. 6.17(a) and Fig. 6.17(b) display the comparison between CBFM/AIM and AIM in CPU time and memory, respectively, as we progressively increased the number of unknowns.

6.3.4 Large 2D and 3D Array Problems

Finally, to demonstrate the capability of the proposed method to solve large problems, we analyze two large-array problems. The first one of these is a

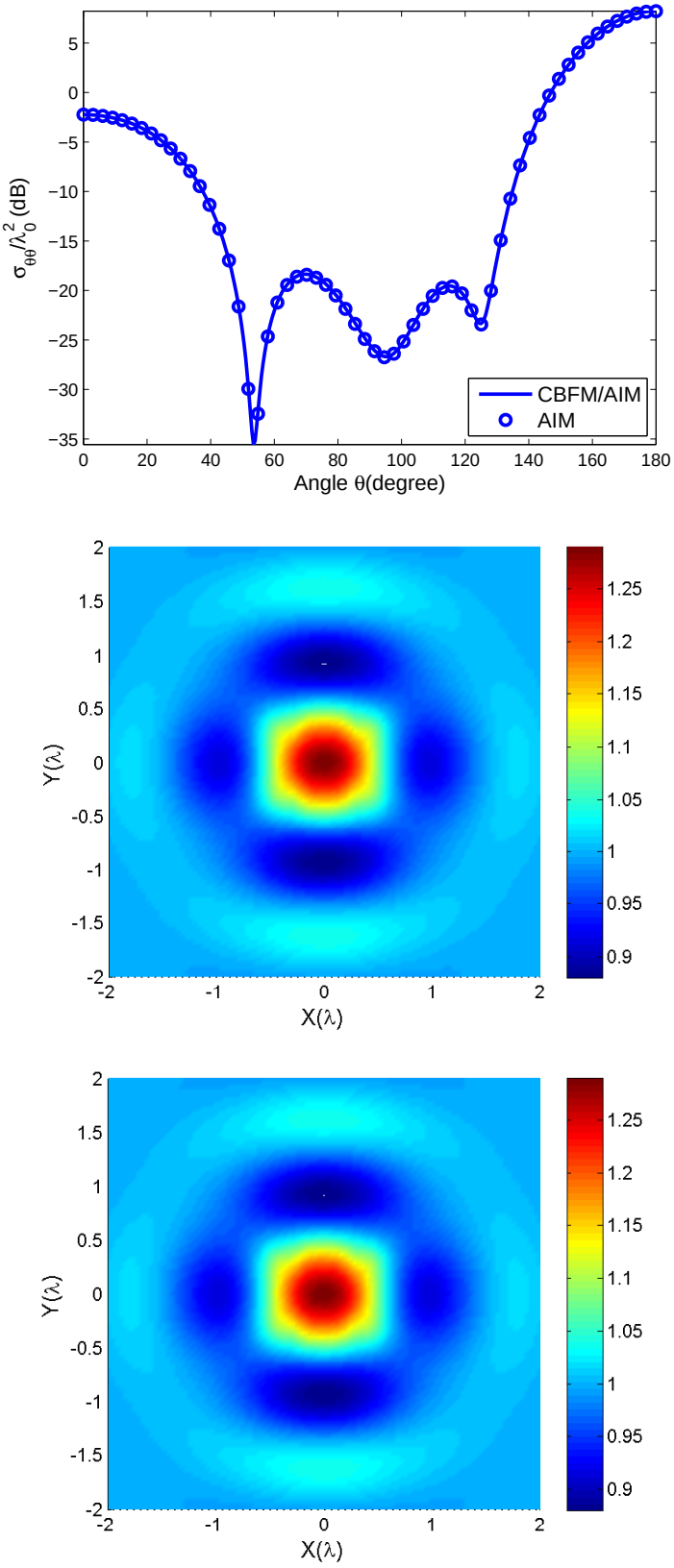

Figure 6.16: Far field RCS and magnitude of electric field calculated for a $2 \times 2 \times 2$ sphere array shown in Fig. 6.3(b). (a) Bistatic RCS in the x-z plane; (b) electric field calculated by CBFM/AIM; (c) electric field calculated by AIM.

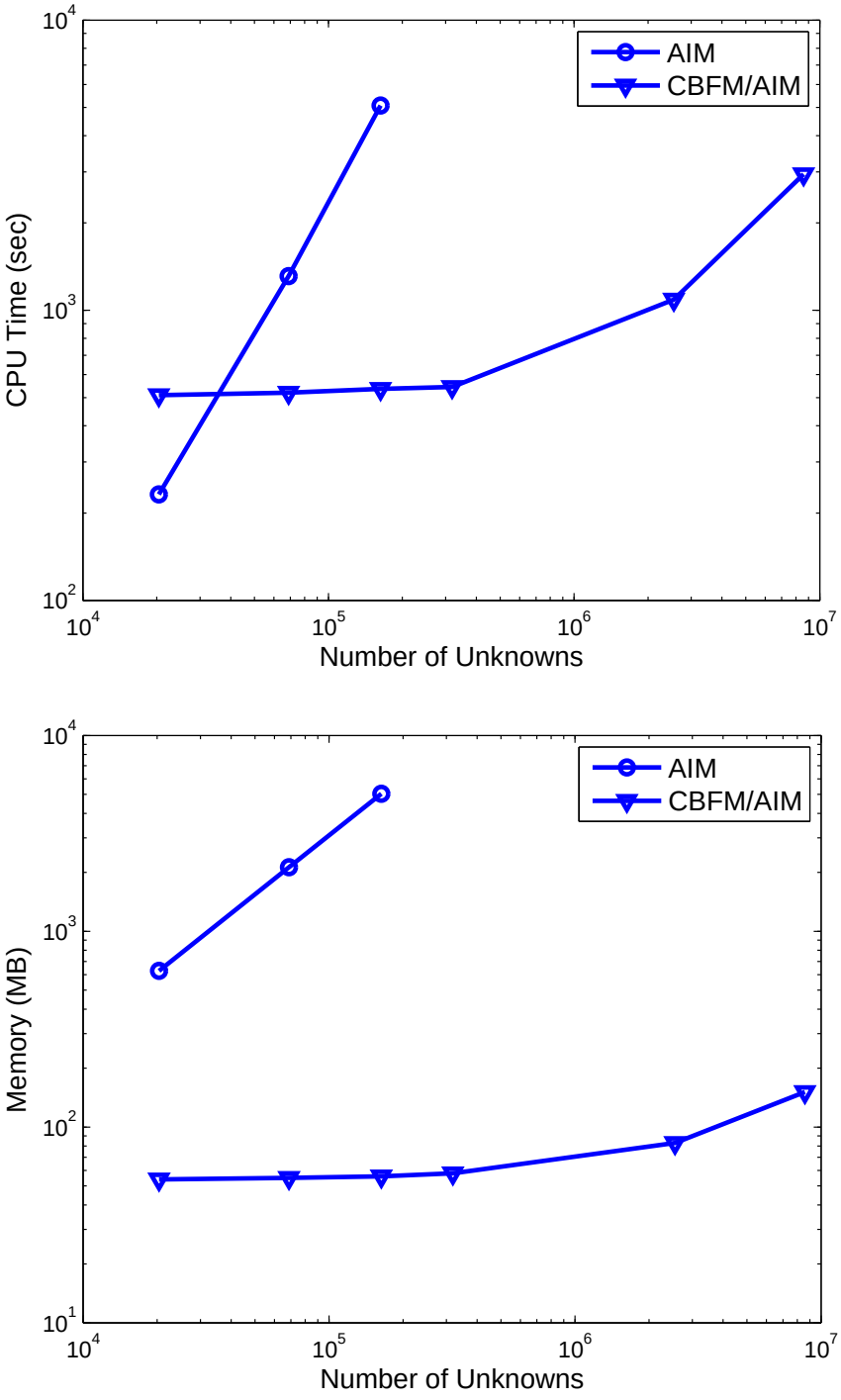

Figure 6.17: Relationship between number of unknowns, (a) computational time and (b) memory requirement for 3D array.

Table 6.2: Computational statistics of CBFM/AIM for various 3D array simulations

size of array	**total number of unknowns**	**total number of CBFs**	**memory (MB)**	**total time (hh:mm:ss)**
$5 \times 5 \times 5$	0.3M	0.01M	58	00:09:04
$10 \times 10 \times 10$	2.5M	0.06M	83	00:18:08
$15 \times 15 \times 15$	8.6M	0.20M	151	00:49:05

2D-array of a 100×100 spherical elements with 25.48 million unknowns. The far field RCS is shown in Fig. 6.18. It requires only 424 MB memory and one hour to solve the problem.

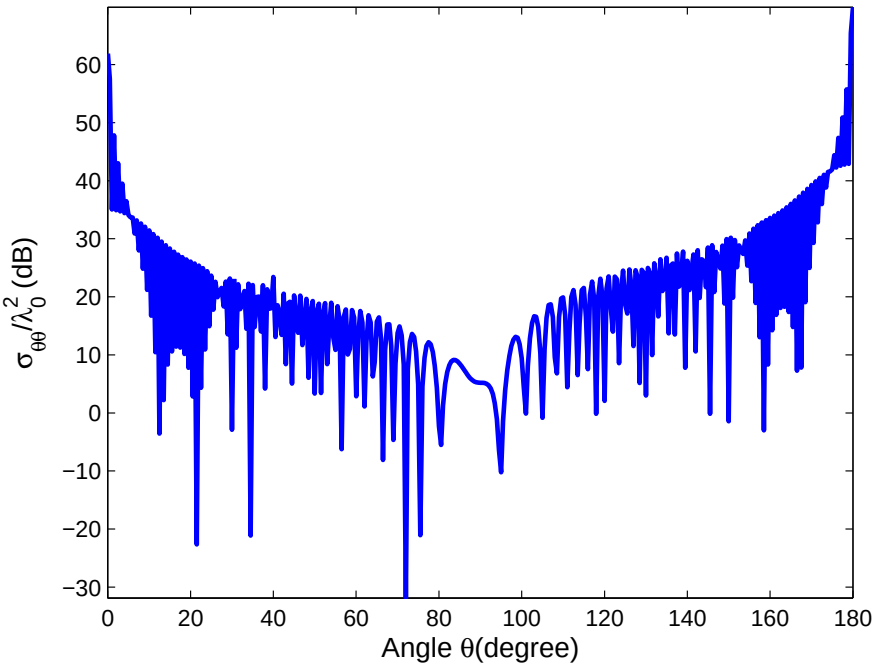

Figure 6.18: Bistatic RCS in x-z plane for a 100×100 spherical array under normal incidence of plane wave with $\boldsymbol{k}$ in the -z direction and $\boldsymbol{E}$ in the $+x$ direction.

The second one is a $15 \times 15 \times 15$ array with 8.6 million unknowns, its far field RCS is shown in Fig. 6.19. It requires only 151 MB memory and one hour to solve the problem.

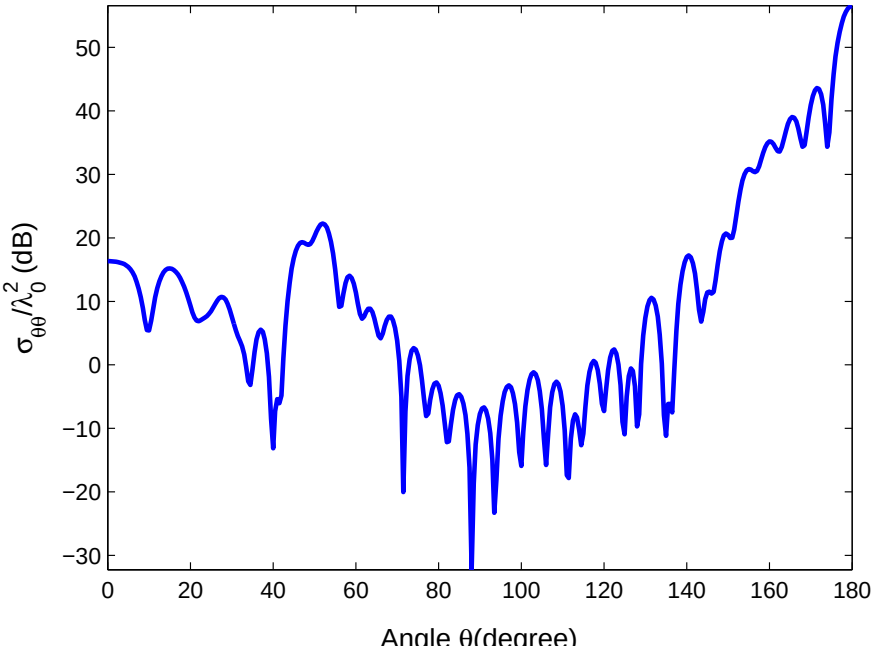

Figure 6.19: Bistatic RCS in x-z plane for a $15 \times 15 \times 15$ spherical array under normal incidence of plane wave with $\boldsymbol{k}$ in the -z direction and $\boldsymbol{E}$ in the $+x$ direction.

Chapter 7

Conclusion for the Thesis

In this thesis, the AIM solvers are developed for the electromagnetic scattering by large-scale objects with composite materials and large-scale finite periodic arrays. The scattering problems are characterized using the surface integral equation method, the volume integral equation method, and the hybrid volume-surface integral equation method. The MoM is applied to discretize the integral equations and solve the resultant matrix equation using an iterative solver. However, the MoM is inadequate when used to solve large-scale electromagnetic problems. The AIM is used to accelerate the matrix-vector multiplication in iterative solvers and to reduce the memory requirement for matrix storage.

In Chapter 3, we have developed the AIM solver for the electromagnetic scattering problems of large-scale objects with chiral materials, which is formulated by using SIE. In the first section, we derive formulations of fields-source relationship in an unbounded chiral medium which forms the theoretical basis for later sections. It is clear that the unbounded chiral medium can be equivalent to two dielectric media, and in the unbounded chiral medium, the fields can be written as the sum of right-handed and left-handed fields. Therefore, surface integral equation for chiral media can

be derived. In the second section, we derive integral equations for a chiral object, mixed chiral objects and composite chiral and conducting objects respectively. In the third section, the MoM is used to discretize the integral equations into matrix forms and then the AIM is modified to accelerate the solution process and reduce the memory requirement. The Numerical examples have been presented to show the accuracy and efficiency of our code in solving the electromagnetic problems of chiral media.

In Chapter 4, we have formulated the scattering problems of composite bi-anisotropic and conducting objects using the hybrid VSIE method. First, we show the constitutive relations for the most general bi-anisotropic media. Second, we derive the VIE for fields inside the bi-anisotropic media and the VSIE when conducting objects are considered. Third, we use the MoM to discretize the integral equations and apply the AIM to accelerate the solution process and reduce the memory requirement. We have presented several numerical examples to demonstrate the accuracy and applicability of the AIM in solving the scattering problems of composite bi-anisotropic and conducting objects.

In Chapter 5, an extended AIM algorithm has been developed based on the ASED basis functions to solve problems of electromagnetic scattering by large-scale finite periodic arrays comprising of metallic and dielectric objects. The VSIE is used to characterize the scattering property of periodic arrays. Two steps are needed in the ASED-AIM to solve the large array problems. The first step is to solve a small-scale problem with nine cells. We obtain the ASED basis function after the first step is completed. In the second step, we use the ASED basis function for each cell and then solve the entire problem. The AIM has been modified to incorporate the ASED basis function which reduces the memory requirement and computational time significantly in solving the array problems. Numerical results

demonstrate the accuracy of the ASED-AIM in comparison with conventional AIM in solving finite array problems. Several large-scale examples are also considered to illustrate its efficiency.

Although ASED-AIM is accurate in capturing the far field RCS info, it is less accurate in the calculation of near field parameters. In order to obtain the near field info, we developed CBFM/AIM method, which is accurate in obtaining both the far field and near field info. In Chapter 6, we presented a new approach that combines the CBFM with the AIM to solve the problem of truncated periodic arrays, which may be either two- or three-dimensional in nature. The generation of the CBFs is carried out efficiently by taking advantage of the identical nature of the elements of the array. Another important feature of the CBFM is that the size of the reduced matrix is typically much smaller than the number of low-level basis functions. It has shown that the memory requirement and the solve-time can be reduced by incorporating the AIM algorithm in the CBFM. Several numerical examples have been presented to demonstrate its accuracy in calculating both near field and far field info as well as its efficiency. The capability of the proposed technique to solve large problems have been adequately demonstrated via several illustrative examples.

Bibliography

[1] A. Taflove and S. C. Hagness, *Computational Electrodynamics: The Finite-Difference Time-Domain Method*, 3rd ed. Artech House Publishers, 2005.

[2] J. M. Jin, *The Finite Element Method in Electromagnetics*, 2nd ed. New York: John Wiley & Sons, 2002.

[3] R. F. Harrington, *Field Computation by Moment Method*, 1st ed. New York: The Macmillan Company, 1968.

[4] L. Greengard and V. Rokhlin, "A fast algorithm for particle simulations," *J. Comput. Phys.*, vol. 73, no. 2, pp. 325–348, Dec. 1987.

[5] V. Rokhlin, "Rapid solution of integral equations of scattering theory in two dimensions," *J. Comput. Phys.*, vol. 86, no. 2, pp. 414–439, Feb. 1990.

[6] C. C. Lu and W. C. Chew, "A fast algorithm for solving hybrid integral equation," *IEE Proceedings-H*, vol. 140, no. 6, pp. 455–460, Dec. 1993.

[7] ——, "A multilevel algorithm for solving boundary integral equations of wave scattering," *Microwave Opt. Technol. Lett.*, vol. 7, no. 10, pp. 466–470, July 1994.

[8] J. M. Song and W. C. Chew, "Multilevel fast-multipole algorithm for solving combined field integral equations of electromagnetics scattering," *Microwave Opt. Technol. Lett.*, vol. 10, no. 1, pp. 14–19, Sept. 1995.

[9] J. M. Song, C. C. Lu, and W. C. Chew, "Multilevel fast multipole algorithm for electromagnetic scattering by large complex objects," *IEEE Trans. Antennas Propagat.*, vol. 45, no. 10, pp. 1488–1493, Oct. 1997.

[10] T. K. Sarkar, E. Arvas, and S. M. Rao, "Application of FFT and the conjugate gradient method for the solution of electromagnetic radiation from electrically large and small conducting bodies," *IEEE Trans. Antennas Propagat.*, vol. 34, no. 5, pp. 635–640, May 1986.

[11] T. J. Peters and J. L. Volakis, "Application of a conjugate gradient FFT method to scattering from thin planar material plates," *IEEE Trans. Antennas Propagat.*, vol. 36, no. 4, pp. 518–526, Apr. 2000.

[12] M. F. Catedra, J. G. Cuevas, and L. Nuno, "A scheme to analyze conducting plates of resonant size using the conjugate gradient method and the fast Fourier transform," *IEEE Trans. Antennas Propagat.*, vol. 36, no. 12, pp. 1744–1752, Dec. 1988.

[13] M. F. Catedra and E. Gago, "Spectral domain analysis of conducting patches of arbitrary geometry in multilayer media using CG-FFT method," *IEEE Trans. Antennas Propagat.*, vol. 38, no. 10, pp. 1530–1536, Oct. 1990.

[14] J. M. Jin and J. L. Volakis, "A biconjugate gradient FFT solution for scattering by planar plates," *Electromagnetics*, vol. 12, no. 1, pp. 105–119, Jan.-Mar. 1992.

[15] H. Gan and W. C. Chew, "A discrete BCG-FFT algorithm for solving 3D inhomogeneous scatterer problems," *J. Electromag. Waves Appl.*, vol. 9, no. 10, pp. 1339–1357, July 1995.

[16] E. Bleszynski, M. Bleszynski, and T. Jaroszewicz, "AIM: adaptive integral method for solving large-scale electromagnetic scattering and radiation problems," *Radio Sci.*, vol. 31, no. 5, pp. 1225–1252, Sept.-Oct. 1996.

[17] W. B. Ewe, L. W. Li, and M. S. Leong, "Fast solution of mixed dielectric/ conducting scattering problem using volume-surface adaptive integral method," *IEEE Trans. Antennas Propagat.*, vol. 52, no. 11, pp. 3071–3077, Nov. 2004.

[18] ——, "Solving mixed dielectric/conducting scattering problem using adaptive integral method," *Progress In Electromagnetics Research*, vol. 46, pp. 143–163, 2004.

[19] W. B. Ewe, L. W. Li, Q. Wu, and M. S. Leong, "AIM solution to electromagnetic scattering using parametric geometry," *IEEE Antennas and Wireless Propagat. Lett.*, vol. 4, pp. 107–111, 2005.

[20] ——, "Preconditioners for adaptive integral method implementation," *IEEE Trans. Antennas Propagat.*, vol. 53, no. 7, pp. 2346–2350, July 2005.

[21] W.-B. Ewe, E.-P. Li, and L.-W. Li, "Aim analysis of electromagnetic transmission through dielectric radomes," *Proceedings of Asia-Pacific Microwave Conference 2006*, 2006.

[22] W. B. Ewe, E. P. Li, H. S. Chu, and L. W. Li, "AIM analysis of electromagnetic scattering by arbitrarily shaped magnetodielectric object," *IEEE Trans. Antennas Propagat.*, vol. 55, no. 7, pp. 2073–2079, July 2007.

[23] W. B. Ewe, L. W. Li, C. S. Chang, and J. P. Xu, "AIM analysis of scattering and radiation by arbitrary surface-wire configurations," *IEEE Trans. Antennas Propagat.*, vol. 55, no. 1, pp. 162–166, Jan. 2007.

[24] L. Hu, L.-W. Li, and T.-S. Yeo, "Fast solution to electromagnetic scattering by large-scaled inhomogeneous bi-anisotropic materials using AIM method," *Progress In Electromagnetics Research*, vol. 99, pp. 21–36, 2009.

[25] ——, "ASED-AIM analysis of scattering by large-scale finite periodic arrays," *Progress In Electromagnetics Research B*, vol. 18, pp. 381–399, 2009.

[26] L. Hu, L.-W. Li, and R. Mittra, "Electromagnetic scattering by finite periodic arrays using CBFM/AIM," *IEEE Trans. Antennas Propagat.*, vol. 58, no. 9, pp. 3086–3090, Sept. 2010.

[27] J. R. Phillips and J. K. White, "A precorrected-FFT method for electrostatic analysis of complicated 3-D structures," *IEEE Transactions on Computer Aided Design of Integrated Circuits and Systems*, vol. 16, no. 10, pp. 1059–1072, Oct. 1997.

[28] N. Yuan, T. S. Yeo, X. C. Nie, L. W. Li, and Y. B. Gan, "Analysis of scattering from composite conducting and dielectric targets using the precorrected-FFT algorithm," *J. Electromag. Waves Appl.*, vol. 17, no. 3, pp. 499–515, 2003.

[29] X. C. Nie, N. Yuan, L. W. Li, Y. B. Gan, and T. S. Yeo, "A fast volume-surface integral equation solver for scattering from composite conducting-dielectric objects," *IEEE Trans. Antennas Propagat.*, vol. 53, no. 2, pp. 818–824, Feb. 2005.

[30] X. C. Nie, L. W. Li, N. Yuan, T. S. Yeo, and Y. B. Gan, "Precorrected-FFT solution of the volume integral equation for 3-D inhomogeneous dielectric objects," *IEEE Trans. Antennas Propagat.*, vol. 53, no. 1, pp. 313–320, Jan. 2005.

[31] X.-C. Nie, N. Yuan, L.-W. Li, Y.-B. Gan, and T.-S. Yeo, "A fast combined field volume integral equation solution to EM scattering by 3-D dielectric objects of arbitrary permittivity and permeability," *IEEE Trans. Antennas Propagat.*, vol. 54, no. 3, pp. 961–969, Mar. 2006.

[32] C. F. Wang, F. Ling, J. Song, and J. M. Jin, "Adaptive integral solution of combined field integral equation," *Microwave Opt. Technol. Lett.*, vol. 19, no. 5, pp. 321–328, Dec. 1998.

[33] J. D. Joannopoulos, R. D. Meade, and J. N. Winn, *Photonic Crystal: Modeling the Flow of Light.* Princeton: Princeton University Press, 1995.

[34] J. B. Pendry, "Negative refraction makes a perfect lens," *Phys. Rev. Lett.*, vol. 85, no. 18, pp. 3966–3969, Oct. 2000.

[35] A. J. Viitanen and I. V. Lindell, "Chiral slab polarization transformer for aperture antennas," *IEEE Trans. Antennas Propagat.*, vol. 46, no. 9, pp. 1395–1397, Sept. 1998.

[36] S. A. Tretyakov and A. A. Sochava, "Proposed composite material for nonreflecting shields and antenna radomes," *Electron. Lett.*, vol. 29, no. 12, pp. 1048–1049, June 1993.

[37] T. Nurgaliev, S. Miteva, A. P. Jenkins, and D. D. Hughes, "Investigation of MW characteristics of HTS microstrip and coplanar resonators with ferrite thin-film components," *IEEE Trans. Microwave Theory Tech.*, vol. 51, no. 1, pp. 33–40, Jan. 2003.

[38] C. M. Krowne, "Full-wave spectral Greens function integral-equation calcula- tion of coplanar ferroelectric thin-film transmission structures," *Microwave Opt. Technol. Lett.*, vol. 26, no. 3, pp. 187–192, June 2000.

[39] ——, "Theoretical considerations for finding anisotropic permittivity in layered ferroelectric/ferromagnetic structures from full-wave electromagnetic simulations," *Microwave Opt. Technol. Lett.*, vol. 28, no. 1, pp. 63–69, Jan. 2001.

[40] C. M. Krowne, M. Daniel, S. W. Kirchoefer, and J. Pond, "Anisotropic permittivity and attenuation extraction from propagation constant measurements using an anisotropic full-wave Greens function solver for coplanar ferroelectric thin-film devices," *IEEE Trans. Microwave Theory Tech.*, vol. 50, no. 1, pp. 537–548, Feb. 2002.

[41] G. W. Hanson, "A numerical formulation of dyadic Greens functions for planar bianisotropic media with application to printed transmission lines," *IEEE Trans. Microwave Theory Tech.*, vol. 44, no. 1, pp. 144–151, Jan. 1996.

[42] C. F. Bohren, "Light scattering by an optically active sphere," *Chem. Phys. Lett.*, vol. 29, no. 3, pp. 458–462, 1974.

[43] ——, "Scattering of electromagnetic waves by an optically ac tive spherical shell," *J. Chem. Phys.*, vol. 62, no. 4, pp. 1566–1571, 1975.

[44] Y. L. Geng, X. B. Wu, L. W. Li, and B. R. Guan, "Mie scattering by a uniaxial anisotropic sphere," *Phys. Rev. E*, vol. 70, no. 5, pp. 056 609/1–8, Nov. 2004.

[45] Y. L. Geng, X. B. Wu, and L. W. Li, "Analysis of electromagnetic scattering by a plasma anisotropic sphere," *Radio Sci.*, vol. 38, no. 6, pp. 1104/1–12, Nov.-Dec. 2003.

[46] ——, "Characterization of electromagnetic scattering by a plasma anisotropic spherical shell," *IEEE Antennas and Wireless Propagat. Lett.*, vol. 3, no. 6, pp. 100–103, June 2004.

[47] Y. L. Geng, X. B. Wu, L. W. Li, and B. R. Guan, "Electromagnetic scattering by an inhomogeneous plasma anisotropic sphere of multilayers," *IEEE Trans. Antennas Propagat.*, vol. 53, no. 12, pp. 3982–3989, Dec. 2005.

[48] Y. L. Geng, "Scattaring of a plane wava by an anisotropic ferrite-coated conducting sphere," *IET Microw. Antennas Propag.*, vol. 2, no. 2, pp. 158–162, Mar. 2008.

[49] A. Semichaevsky, A. Akyurtlu, D. Kern, D. H. Werner, and M. G. Bray, "Novel BI-FDTD approach for the analysis of chiral cylinders and spheres," *IEEE Trans. Antennas Propagat.*, vol. 54, no. 3, pp. 925–932, Mar. 2006.

[50] V. Demir, A. Z. Elsherbeni, and E. Arvas, "FDTD formulation for dispersive chiral media using the Z transform method," *IEEE Trans. Antennas Propagat.*, vol. 53, no. 10, pp. 3374–3384, Oct. 2005.

[51] A. Grande, I. Barba, A. C. L. Cabeceira, J. Represa, P. P. M. So, and W. J. R. Hoefer, "FDTD modeling of transient microwave signals in dispersive and lossy bi-isotropic media," *IEEE Trans. Microwave Theory Tech.*, vol. 52, no. 3, pp. 773–784, Mar. 2004.

[52] Z. Chen, W. Hong, and W. Zhang, "Electromagnetic scattering from a chiral cylinder-general case," *IEEE Trans. Antennas Propagat.*, vol. 44, no. 7, pp. 912–917, July 1996.

[53] F. Bilotti, A. Toscano, and L. Vegni, "FEM-BEM formulation for the analysis of cavity-backed patch antennas on chiral substrates," *IEEE Trans. Antennas Propagat.*, vol. 51, no. 2, pp. 306–311, Feb. 2003.

[54] L. Valor and J. Zapata, "An efficient finite element formulation to analyze waveguides with lossy inhomogeneous bi-anisotropic materials," *IEEE Trans. Microwave Theory Tech.*, vol. 44, no. 2, pp. 291–296, Feb. 1996.

[55] ——, "A simplified formulation to analyze inhomogeneous waveguide with lossy chiral media using the finite-element method," *IEEE Trans. Microwave Theory Tech.*, vol. 46, no. 2, pp. 185–187, Feb. 1998.

[56] I. V. Lindell, A. H. Sihvola, S. A. Tretyakov, and A. J. Viitanen, *Electromagnetic Waves in Chiral and Bi-Isotropic Media.* Boston, MA: Artech House, 1994.

[57] M. S. Kluskens and E. H. Newman, "Scattering by a chiral cylinder of arbitrary cross section," *IEEE Trans. Antennas Propagat.*, vol. 38, no. 9, pp. 1448–1455, Sept. 1990.

[58] ——, "Scattering by a multilayer chiral cylinder," *IEEE Trans. Antennas Propagat.*, vol. 39, no. 1, pp. 91–96, Jan. 1991.

[59] D. Worasawate, J. R. Mautz, and E. Arvas, "Electromagnetic scattering from an arbitrarily shaped three-dimensional homogeneous chiral body," *IEEE Trans. Antennas Propagat.*, vol. 51, no. 5, pp. 1077–1084, May 2003.

[60] D. H. Schaubert, D. R. Wilton, and A. W. Gilsson, "A tetrahedral modeling method for electromagnetic scattering by arbitrarily shaped inhomogeneous dielectric bodies," *IEEE Trans. Antennas Propagat.*, vol. 32, no. 1, pp. 77–85, Jan. 1984.

[61] C. C. Lu and W. C. Chew, "A coupled surface-volume integral equation approach for the calculation of electromagnetic scattering from composite metallic and material targets," *IEEE Trans. Antennas Propagat.*, vol. 48, no. 12, pp. 1866–1868, Dec. 2000.

[62] C. C. Su, "Electromagnetic scattering by a dielectric body with arbitrary inhomogeneity and anisotropy," *IEEE Trans. Antennas Propagat.*, vol. 37, no. 3, pp. 384–389, Mar. 1989.

[63] G. Kobidze and B. Shanker, "Integral equation based analysis of scattering from 3-D inhomogeneous anisotropic bodies," *IEEE Trans. Antennas Propagat.*, vol. 52, no. 10, pp. 2650–2658, Oct. 2004.

[64] M. Hasanovic, C. Mei, J. R. Mautz, and E. Arvas, "Scattering from 3-D inhomogeneous chiral bodies of arbitrary shape by the method of moments," *IEEE Trans. Antennas Propagat.*, vol. 55, no. 6, pp. 1817–1825, June 2007.

[65] R. Kindt, K. Sertel, E. Topsakal, and J. Volakis, "Array decomposition method for the accurate analysis of finite arrays," *IEEE Trans. Antennas Propagat.*, vol. 51, no. 6, pp. 1364–1372, 2003.

[66] R. W. Kindt and J. L. Volakis, "Array decomposition-fast multipole method for finite array analysis," *Radio Sci.*, vol. 39, no. 2, 2004.

[67] S. C. Lee, M. N. Vouvakis, and J. F. Lee, "A non-overlapping domain decomposition method with non-matching grids for modeling large finite antenna arrays," *J. Comput. Phys.*, vol. 203, no. 1, pp. 1–21, Feb. 2005.

[68] M. N. Vouvakis and J. F. L. Z. Cendes, "A FEM domain decomposition method for photonic and electromagnetic band gap structures," *IEEE Trans. Antennas Propagat.*, vol. 54, no. 2, pp. 721–733, Feb. 2006.

[69] M. N. Vouvakis, K. Z. Zhao, S. M. Seo, and J. F. Lee, "A domain decomposition approach for non-conformal couplings between finite and boundary elements for unbounded electromagnetic problems in R-3," *J. Comput. Phys.*, vol. 225, no. 1, pp. 975–994, July 2007.

[70] K. Z. Zhao, V. Rawat, and J. F. Lee, "A domain decomposition method for electromagnetic radiation and scattering analysis of multi-target problems," *IEEE Trans. Antennas Propagat.*, vol. 56, no. 8, pp. 2211–2221, Aug. 2008.

[71] Z. Peng, V. Rawat, and J. F. Lee, "One way domain decomposition method with second order transmission conditions for solving electromagnetic wave problems," *J. Comput. Phys.*, vol. 229, no. 4, pp. 1181–1197, Feb. 2010.

[72] Y. J. Li and J. M. Jin, "A vector dual-primal finite element tearing and interconnecting method for solving 3-D large-scale electromagnetic problems," *IEEE Trans. Antennas Propagat.*, vol. 54, no. 10, pp. 3000–3009, Oct. 2006.

[73] ——, "A new dual-primal domain decomposition approach for finite element simulation of 3-D large-scale electromagnetic problems," *IEEE Trans. Antennas Propagat.*, vol. 55, no. 10, pp. 2803–2810, Oct. 2007.

[74] ——, "Implementation of the second-order ABC in the FETI-DPEM method for 3D EM problems," *IEEE Trans. Antennas Propagat.*, vol. 56, no. 8, pp. 2765–2769, Aug. 2008.

[75] ——, "Simulation of photonic crystal nanocavity using the FETI-DPEM method," *Microwave Opt. Technol. Lett.*, vol. 50, no. 8, pp. 2083–2086, Aug. 2008.

[76] ——, "Parallel implementation of the FETI-DPEM algorithm for general 3D EM simulations," *J. Comput. Phys.*, vol. 228, no. 9, pp. 3255–3267, May 2009.

[77] A. Neto, S. Maci, G. Vecchi, and M. Sabbadini, "A truncated Floquet wave diffraction method for the full wave analysis of large phased arrays-Part II: Generalization to 3-D cases," *IEEE Trans. Antennas Propagat.*, vol. 48, no. 3, pp. 601–611, Mar. 2000.

[78] ——, "A truncated Floquet wave diffraction method for the full wave analysis of large phased arrays - Part I: Basic principles and 2-D cases," *IEEE Trans. Antennas Propagat.*, vol. 48, no. 4, pp. 594–600, Apr. 2000.

[79] A. Cucini, M. Albani, and S. Maci, "Truncated Floquet wave full-wave analysis of large phased arrays of open-ended waveguides with a nonuniform amplitude excitation," *IEEE Trans. Antennas Propagat.*, vol. 51, no. 6, pp. 1386–1394, June 2003.

[80] ——, "Truncated Floquet wave full-wave (T(FW)(2)) analysis of large periodic arrays of rectangular waveguides," *IEEE Trans. Antennas Propagat.*, vol. 51, no. 6, pp. 1373–1385, June 2003.

[81] C. Craeye, A. G. Tijhuis, and D. H. Schaubert, "An efficient MoM formulation for finite-by-infinite arrays of two-dimensional antennas arranged in a three-dimensional structure," *IEEE Trans. Antennas Propagat.*, vol. 52, no. 1, pp. 271–282, Jan. 2004.

[82] C. Craeye and X. Dardenne, "Element pattern analysis of wide-band arrays with the help of a finite-by-infinite array approach," *IEEE Trans. Antennas Propagat.*, vol. 54, no. 2, pp. 519–526, Feb. 2006.

[83] V. V. S. Prakash and R. Mittra, "Characteristic basis function method: A new technique for efficient solution of method of moments

matrix equations," *Microwave Opt. Technol. Lett.*, vol. 36, no. 2, pp. 95–100, Jan. 2003.

[84] C. D. C, M. Catedra, and R. Mittra, "Application of the characteristic basis function method utilizing a class of basis and testing functions defined on NURBS patches," *IEEE Trans. Antennas Propagat.*, vol. 56, no. 3, pp. 784–791, Mar. 2008.

[85] E. Lucente, A. Monorchio, and R. Mittra, "An iteration-free MoM approach based on excitation independent characteristic basis functions for solving large multiscale electromagnetic scattering problems," *IEEE Trans. Antennas Propagat.*, vol. 56, no. 4, pp. 999–1007, Apr. 2008.

[86] G. Tiberi, A. Monorchio, G. Manara, and R. Mittra, "A spectral domain integral equation method utilizing analytically derived characteristic basis functions for the scattering from large faceted objects," *IEEE Trans. Antennas Propagat.*, vol. 54, no. 9, pp. 2508–2514, Sept. 2006.

[87] C. Delgado, M. F. Catedra, and R. Mittra, "Efficient multilevel approach for the generation of characteristic basis functions for large scatters," *IEEE Trans. Antennas Propagat.*, vol. 56, no. 7, pp. 2134–2137, July 2008.

[88] G. Ogucu, R. M. R, and K. Du, "An interpolation algorithm to reduce the reduced matrix fill-time in CBFM," *IEEE Antennas and Wireless Propagat. Lett.*, vol. 8, pp. 457–460, 2009.

[89] L. Matekovits, V. A. Laza, and G. Vecchi, "Analysis of large complex structures with the synthetic-functions approach," *IEEE Trans. Antennas Propagat.*, vol. 55, no. 9, pp. 2509–2521, Sept. 2007.

[90] L. Matekovits, G. Vecchi, M. Bercigli, and M. Bandinelli, "Synthetic-functions analysis of large aperture-coupled antennas," *IEEE Trans. Antennas Propagat.*, vol. 57, no. 7, pp. 1936–1943, July 2009.

[91] ——, "Efficient numerical analysis of large planar high impedance surface by the synthetic function expansion technique," *Microwave Opt. Technol. Lett.*, vol. 51, no. 11, pp. 2763–2769, Nov. 2009.

[92] W. B. Lu, T. J. Cui, Z. G. Qian, X. X. Yin, and W. Hong, "Accurate analysis of large-scale periodic structures using an efficient sub-entire-domain basis function method," *IEEE Trans. Antennas Propagat.*, vol. 52, no. 11, pp. 3078–3085, Nov. 2004.

[93] W. B. Lu, T. J. Cui, X. X. Yin, Z. G. Qian, and W. Hong, "Fast algorithms for large-scale periodic structures using subentire domain basis functions," *IEEE Trans. Antennas Propagat.*, vol. 53, no. 3, pp. 1154–1162, Mar. 2005.

[94] W. B. Lu, T. J. Cui, and H. Zhao, "Acceleration of fast multipole method for large-scale periodic structures with finite sizes using sub-entire-domain basis functions," *IEEE Trans. Antennas Propagat.*, vol. 55, no. 2, pp. 414–421, Feb. 2007.

[95] D. J. Bekers, S. J. L. van Eijndhoven, A. A. F. van de Ven, P. P. Borsboom, and A. G. Tijhuis, "Eigencurrent analysis of resonant behavior in finite antenna arrays," *IEEE Trans. Microwave Theory Tech.*, vol. 54, no. 6, pp. 2821–2829, June 2006.

[96] D. J. Bekers, S. J. L. van Eijndhoven, and A. G. Tijhuis, "An eigencurrent approach for the analysis of finite antenna arrays," *IEEE Trans. Antennas Propagat.*, vol. 57, no. 12, pp. 3772–3782, Dec. 2009.

[97] ——, "An eigencurrent description of finite arrays of electromagnetically characterized elements," *Radio Sci.*, vol. 44, no. RS2S90, Mar. 2009.

[98] E. Suter and J. R. Mosig, "A subdomain multilevel approach for the efficient mom analysis of large planar antennas," *Microwave Opt. Technol. Lett.*, vol. 26, no. 4, pp. 270–277, June 2000.

[99] I. Stevanovic and J. R. Mosig, "Efficient evaluation of macrobasis-function reaction terms in the subdomain multilevel approach," *Microwave Opt. Technol. Lett.*, vol. 42, no. 2, pp. 138–143, July 2004.

[100] ——, "Using symmetries and equivalent moments in improving the efficiency of the subdomain multilevel approach," *IEEE Antennas and Wireless Propagat. Lett.*, vol. 4, pp. 158–161, 2005.

[101] K. C. Donepudi, J. M. Jin, and W. C. Chew, "A higher order multilevel fast multipole algorithm for scattering from mixed conducting/dielectrics bodies," *IEEE Antennas Propagat. Mag.*, vol. 51, no. 10, pp. 2814–2821, Oct. 2003.

[102] J. Liu and J. M. Jin, "A novel hybridization of higher order finite element and boundary integral methods for electromagnetic scattering and radiation problems," *IEEE Trans. Antennas Propagat.*, vol. 49, no. 12, pp. 1794–1806, Dec. 2001.

[103] A. F. Yagli, "Electromagnetic scattering from three-dimensional gyrotropic objects using the transmission line modeling (TLM) method," Ph.D. dissertation, Syracuse University, 2006.